Physical Modelling of Pier Scour in a Constricting Channel

Thesis submitted to the
Faculty of Graduate and Postdoctoral Studies
In partial fulfillment of the requirements
for the Masters of Applied Science degree in Civil Engineering

The Ottawa-Carleton Institute for Civil Engineering
Department of Civil Engineering
Faculty of Engineering
University of Ottawa

Abstract

Experiments were completed in order to examine the effects of combined constriction and pier scour. Scour is cited as being a leading cause of bridge failure. It was found that in cases where both constriction and pier scour are present, the sum is greater than the linear addition of each individual case. This is contrary to the current industry assumption which states that the total depth of scour is the linear sum of the constriction and pier scour depth.

Velocimetry and scour data were collected enabling comparisons to be made in order to determine how the flowfield influences the equilibrium scour conditions. In addition, experiments were performed examining the effect that the pier shape has on the scour depth and distribution.

Since the results are contrary to the assumption used in industry, they are especially important and may help reduce future bridge failures.

Acknowledgements

I would like to thank my supervisor, Professor Colin Rennie for his help during this thesis. I'd like to thank my friends and family for their help and support during this process.

This thesis would not have been possible without an Educational Leave form Environment Canada or without Mohammed Barry and James Reid for collecting data while I was working. Above all, I'd like to thank God for his love and grace. [John 3:16].

List of Symbols

d_s = Diameter of the sediment

γ_s = Specific weight of the sediment

γ = Specific wieght of the fluid

c_1 = Coefficient for the volume of the sediment

c_2 = Coefficient for the surface area exposed to the drag force

U_{*C} = Critical shear velocity

v = Viscosity of fluid

τ_0 = Shear stress

τ_c^* = Dimensionless Shear Stress

R_* = Boundary Reynolds Number

K_s= Factor for the shape of the pier,

K_Θ= Factor for the angle of approach,

K_3 = Factor for the mode of sediment transport,

K_4 = Factor for armouring by bed material,

b = Width of the pier,

d_s = Scour depth,

Fr = Froude number,

y = Water depth before the constriction

c = Speed of sound,

τ = Time between pulses in a pulse pair,

f = Acoustic operating frequency (f).

$d\theta$ = Doppler phase shift for a pulse pair,

$\frac{d\theta}{d\tau}$ = Average phase shift for several pulse pairs.

u', v', and w' = Fluctuating components of velocity in the X, Y and Z directions.

ω = Vorticity

$\overline{U}$, $\overline{V}$ = Mean velocities in the x, y directions respectively

c = Speed of light,

τ = Time lag between pulses in a pulse pair

f =Acoustic frequency

V = velocity

L = Length

Dm = Model dimension

Dp = Prototype dimension

τ_o= Shear stress

γ= Specific gravity of water

γ_s=Specific gravity of sediment

d_s= Diameter of sediment

m = Model parameters

p = Prototype parameters

C32 = Constriction and two piers

C30 = Constriction Alone

C02 = Two Square Piers Alone

List Of Tables

Table of Figures

Table of Contents

1 Introduction

The objective of this study is to examine scouring, which is one of the major processes that cause bridge failures. This is completed though a series of experiments within two flumes at the University of Ottawa. Flow data and sediment data were collected and then analysed so comparisons can be made to current bridge design practices.

To reduce span lengths, bridges are often placed in a channel constriction. Current design practice is to assume that total scour at a pier is the linear sum of scour that would be generated due to flow acceleration in the constriction, and local scour that would be generated due to flow deflection around the pier (Arneson et al, 2012). The experimental results of this study demonstrate that this assumption is non-conservative for the range of blockage ratios tested which were from 0.1 to 0.6. In fact, total scour can exceed the linear sum of constriction scour and local pier scour. In other words, this project shows that having both types of scouring simultaneously produces a cumulative effect resulting in a scour depth that is greater than the sum of the individual components for all of the tested cases. This important result can change bridge design procedures leading to fewer failures.

1.1Problem Statement

The focus of this research project is to examine and compare the scouring processes that occur around a bridge pier in a spatially uniform versus spatially accelerating flow field.

Bridge pier scouring is the process wherein sediment at the foundation of bridge piers is eroded by the river (Melville & Coleman, 2000). Scour at bridge supports can decrease the structural integrity of the bridge and cause failure (Melville & Coleman, 2000). In America, it has been estimated that 60% of bridges fail due to processes

involving river hydraulics, including pier scour (Melville & Coleman, 2000). In New Zealand, it has been approximated that one bridge fails per year due to scouring (Melville & Coleman, 2000).

No previous research has examined pier scour in a narrowing channel. Bridges are typically built at natural river constrictions in order to minimize large spans. Thus, many bridges are built in locations where the flow is undergoing spatial acceleration upstream of the bridge. Scour can be induced by the channel constriction itself, which will compound the local scour at the bridge pier. In this study, the influence of channel narrowing on pier scour will be examined. A proper understanding of scouring at bridge piers in a narrowing channel can reduce bridge failures.

1.2 Statement of Novelty / Significance

Scale models were developed within two mobile-bed flumes at the Civil Engineering Hydraulics Laboratory at the University of Ottawa. Larger scale tests were conducted in the 12 m long straight part of the 1.0 m wide bend flume. A larger number of smaller scale tests were conducted in a 0.61 m wide by 2.0 m long pier scour flume. Scour in spatially uniform flow fields was evaluated in straight flume runs, and internal walls were constructed within each flume to develop a channel constriction such that scour in spatially accelerating flow fields could be tested. The 3D turbulent flow field was measured using Acoustic Doppler Velocimeters. To the best of the candidate's knowledge, these were the first physical model tests of pier scour with and without channel constriction.

Currently, it is assumed that the total amount of scour at a bridge is the linear sum of the local scour caused by the piers and the scour caused by the constriction. This assumption is thought to be conservative but in the experiments performed in this study, it was actually found that this assumption is not conservative for the range of

blockage ratios tested which ranged from 0.1 to 0.6. This is an important result, which could possibly lead to changes in bridge design procedures.

This research results in a better understanding of the complex scour process, from which improved methods to minimize pier scour failure can be developed.

2. Sediment Transport Fundamentals

Prior to understanding the complicated flow patterns around a bridge pier, it is important to discuss the fundamentals of general sediment transport.

A grain in a channel has several forces acting upon it. These include the gravity forces consisting of weight and buoyancy, hydrodynamic lift forces which are normal to the river bed and drag forces that are parallel. These forces act on a grain of sediment as shown in Figure 1 (García, 2008). In the diagram below, ø represents the slope of the bed while ɵ represents the angle of repose of the sediment.

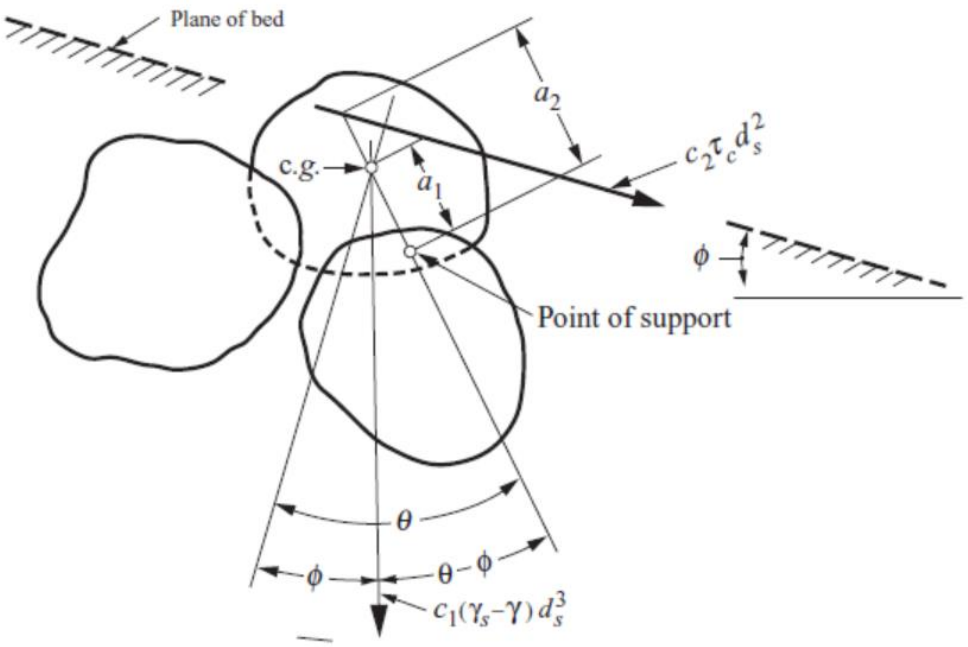

Figure 1: Forces on a grain of sediment on a river bed with a slope ø (Garcia 2008).

The definition of variables and equations is as follows.

$$d_s = \text{diameter of the sediment}$$
$$\gamma_s = \text{specific weight of the sediment}$$
$$\gamma = \text{specific wieght of the fluid}$$
$$c_1 = \text{coefficient for the volume of the sediment}$$
$$c_2 = \text{coefficient for the surface area exposed to the drag force}$$

$$Gravity\ Force = c_1(\gamma_s - \gamma)d_s^3 \qquad (1)$$

$$Particle\ Volume = c_1 d_s^3 \qquad (2)$$

$$critical\ drag\ force = c_2\tau_c d_s^2 \qquad (3)$$

Where $\tau_c d_s^2$ is the exposed surface area of the particle

The sediment starts to rotate when the forces causing it to move are greater than the forces that are stabilizing it. This is mathematically represented by equating the

moment caused by the drag forces to the moment caused by the gravity forces about the point of support as shown in Figure 1. These can be seen in equations 4 and 5 below.

$$c_1(\gamma_s - \gamma)d_s^3 a_1 \sin(\theta - \emptyset) = c_2 \tau_c d_s^2 a_2 cos\theta \quad (4)$$

$$\tau_c = \frac{c_1 a_1}{c_2 a_2}(\gamma_s - \gamma)d_s cos\emptyset(tan\theta - tan\emptyset) \quad (5)$$

Thus, the shear stress required for particle entrainment depends upon both particle size and the local geometry of particle packing.

To overcome this complexity, empirical methods are employed to predict particle entrainment. A typical method to determine when sediment movement will occur is to use the Shields diagram seen in Figure 2. By determining the parameters that make up the axes of this graph, engineers are able to predict whether or not sediment movement can be expected to occur for particular particle sizes and flow conditions. There is no movement expected when the shear stress and Reynolds numbers produce a point that is below the line on the Shields diagram. More practical detail on how to use this chart can be found in (García, 2008)

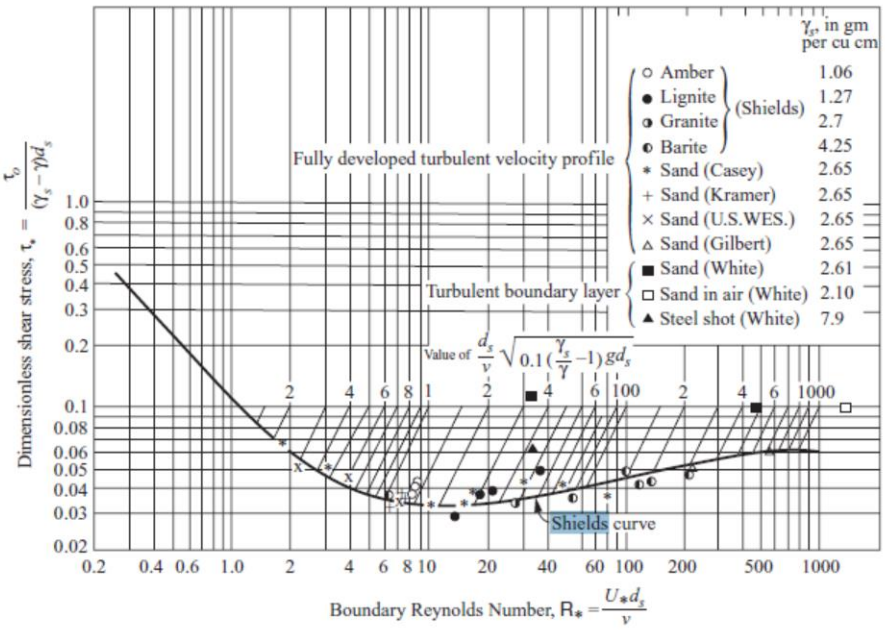

Figure 2: Shields Diagram describing sediment movement (García, 2008)

In order to use the Shields diagram, one must determine the dimensionless shear stress and the boundary Reynolds number which are calculated by the parameters below.

$$Dimensionless\ Shear\ Stress = \tau_c^* = \frac{\tau_0}{(\gamma_s - \gamma)d_s} \quad (6)$$

$$Boundary\ Reynolds\ Number\ R_* = \left(\frac{U_{*c}D}{\nu}\right) \quad (7)$$

$$U_{*C} = critical\ shear\ velocity$$
$$\nu = viscosity\ of\ fluid$$
$$\tau_0 = shear\ stress$$

2.1 Background on Scouring

Scouring is an extremely important process that greatly affects the health of modern infrastructure. In America, it has been estimated that 60% of bridges fail due to processes involving river hydraulics, including pier scour (Melville & Coleman, 2000). In

New Zealand it has been approximated that one bridge fails per year due to scouring (Melville & Coleman, 2000).

Scouring can be defined as the lowering of the river bed elevation due to the transport of bed sediment. The three classifications of scour are general, local and constriction scour. General scour occurs naturally, that is without obstructions created by hydraulic structures such as piers and abutments (Coleman, 1997). Local scour occurs in the immediate vicinity of a structure due to the complicated turbulent three-dimensional flow field that is formed (Dey & Raikar, 2007). The final type of scour is constriction scour which occurs when there is a constriction in the cross section causing the flow to accelerate in order to satisfy continuity. The accelerated flow increases both turbulence and bed shear stress, which increases the sediment transport (Federico, 2003). Of these three classifications, local scour has been the subject of the most intensive study with respect to bridge piers.

2.2 Clearwater verses Live Bed Scour

Two conditions for scour are clearwater scour and live bed scour. Clearwater scour refers to conditions in which no sediment is entering the study area from upstream. This condition occurs when the velocity upstream is less than the critical velocity required to transport sediment in that particular river. The critical velocity changes depending on the river due to the size and distribution of the sediments. The velocity of the water translates into shear stress which when reaching a value greater than the critical shear stress, moves the sediments and thus creates scour.

The second condition of scour is called the live bed condition which occurs when sediment is being moved into the study area from upstream. Contrary to clearwater scour, this condition occurs when the water velocity is higher than the critical velocity

(Dey & Raikar, 2007) , (Roads, 2013). In general, live bed scour occurs in cycles depending on the seasonal conditions. For example, when there is more water in the river during the rainy season, more shear stress is generated causing increased live bed scour (Roads, 2013).

2.3 Local Scour Mechanism

In general, when a fluid flows around an object, its pattern changes and can be quite complex. This happens when water flows around a bridge pier. In order to understand these processes, it is important that one examines the actual mechanisms and flow patterns that occur as water flows around a bridge pier.

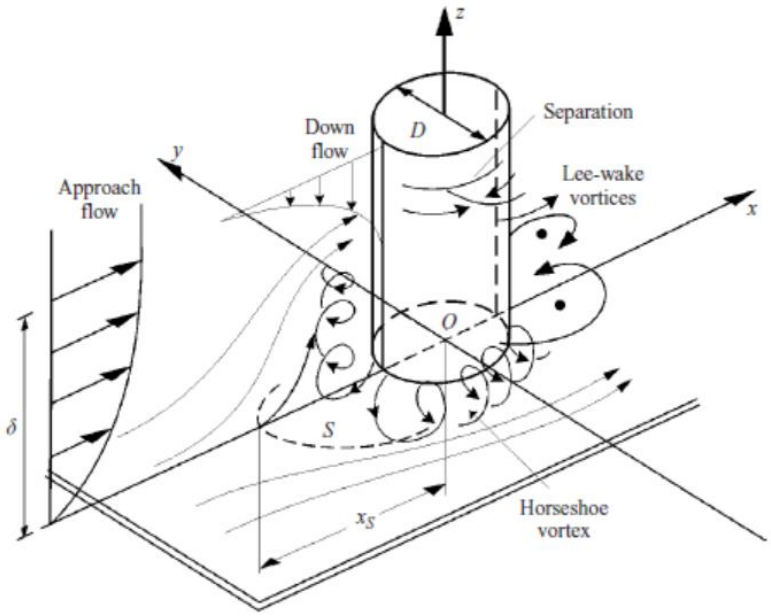

Figure 3: Flow pattern around a bridge pier (A. Roulund, 2005)

Figure 3 above provides a schematic of the flow field around a bridge pier. As one can see, the approach flow has a velocity gradient that increases with height as expected due to the no slip condition at the bed. When the water hits the pier, it decelerates at the front of the pier. This causes a stagnation pressure which is highest at the top of the pier and decreases downwards (Melville & Coleman, 2000). This pressure

difference causes downflow which scours the area directly in front of the pier. As the scour hole develops, a slope is created which causes sediments to slide into the hole where the downflow jet is located, causing more scour.

A horseshoe vortex forms because of the water being “piled up” just upstream of the pier and because of the acceleration around the pier (Richardson et al, 2001). It removes the newly mobile sediment away from the scour hole to a downstream location (Melville & Coleman, 2000). The presence of the horseshoe vortex creates velocity gradients near the bed which cause scour. At the beginning of the local scouring process, there is no scour hole but it deepens until equilibrium scour is reached. As the scouring develops, the horseshoe vortex weakens until it matches the critical shear stress of the particles at the bottom of the scour hole (Richardson et al, 2001). At this point, no more scouring can occur because the vortex is too weak to move any sediment.

As shown in Figure 3 and also in more detail in Figure 4, another coherent structure that forms around a bridge pier is a wake vortex. Along with the horseshoe vortex, the wake vortex causes increased bed shear stress and therefore scouring. It has been found that the strength of the wake vortex decreases quickly downstream of the pier resulting in a rapidly dropping shear stress distribution. Practically, this translates into deposition close to the pier. In the area directly behind the pier, there is reduced pressure which causes a recirculation zone which contributes to the deposition in the wake region.

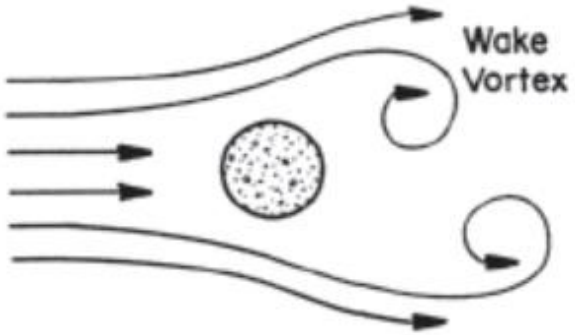

Figure 4: Plan view of a circular pier highlighting the wake vortices (Richardson & Richardson, 2008)

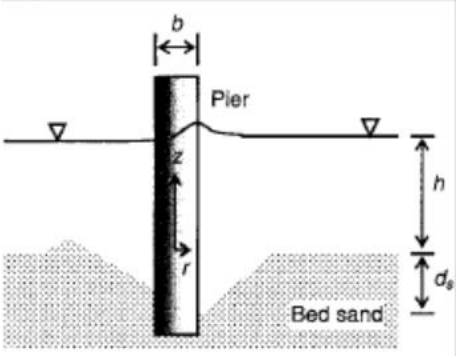

Figure 5: Experimental scour field around a square pier; flow from right to left (Raikar & Dey, 2007).

Figure 5 shows the profile view of scour results from a flume experiment. Note that the scour hole is deepest directly in front of the pier as caused by the horseshoe vortex and there is also scouring behind the pier caused by the wake vortices. As the wake vortices weaken to the point where they produce less than the critical shear, deposition happens as seen in the figure above.

2.4 Effect of Pier Shape and orientation

The amount of scour is also affected by the pier shape, size as well as orientation (Roads, 2013). For example, one would predict that an elliptical pier may produce less

scour than a square pier due to its shape. Various experiments have been performed to examine closely the effect of pier shape on scour. Figure 6 summarizes the results of one such study (Mostafa, 1994, cited in Melville and Coleman 2000).

Shape	l/b	Projected width of pier (mm)	$\frac{d_{s(noncircular)}}{d_{s(circular)}}$
A	4	140	1.50
B	4		1.33
C	1		1.29
D	200		1.28
E	1		1.28
F	1		1.07
G	1		1.00

Figure 6: The shapes A to G on the scour depth relative to a circular pier (Melville, 2000)

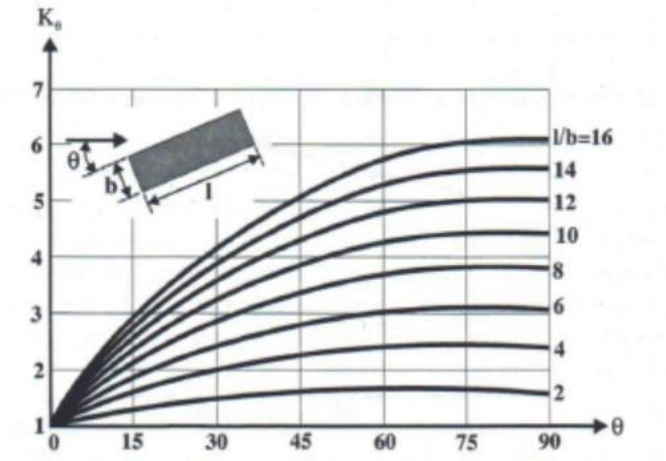

Figure 6.17. Local scour depth variation with pier alignment.

Figure 7: The effect of pier orientation on the scour depth. (Melville, 2000)

With the exception of circular piers, the angle at which the water hits the pier is an important factor in the depth of local scour as shown in Figure 7. The K_θ axis represents the factor by which the scour depth is expected to increase as found in experiments by Ettema (Ettema, 1998) .

Local scouring has been studied fairly extensively which has resulted in a wide range of equations. An example of this is the equation developed by Richardson and Davis which is used in HEC-18 (Melville & Coleman, 2000). According to this equation, the scour depth depends on the width of the pier, the velocity, the shape of the pier, the approach angle of water onto the pier, armouring by bed material as well as the width of the pier.

$$\frac{d_s}{b} = 2.0 K_s K_\theta K_3 K_4 \left(\frac{y}{b}\right)^{0.35} F_1^{0.43} \quad (8)$$

Where

K_s= factor for the shape of the pier, K_θ= factor for the angle of approach, K_3 = factor for the mode of sediment transport, K_4 = factor for armouring by bed material, b = width of the pier, d_s = scour depth, Fr = Froude number, y = water depth before the constriction

One of the most detailed measurements of the flow field was performed in a study by Dey (Dey & Raikar, 2007). In this experimental study, the flow field around a developing scour hole is analyzed using acoustic techniques. Clearwater conditions were used in the flume with a flow velocity of around 95% of the critical velocity. The resulting data were extremely detailed, presenting the velocity, turbulent kinetic energy, and Reynolds stresses at various planes as well as at various times during the scour hole development. The plot for the cross sectional plane at equilibrium are shown in Figure 8. More details on the physical interpretation of the Reynolds stresses can be found in the Methods section below.

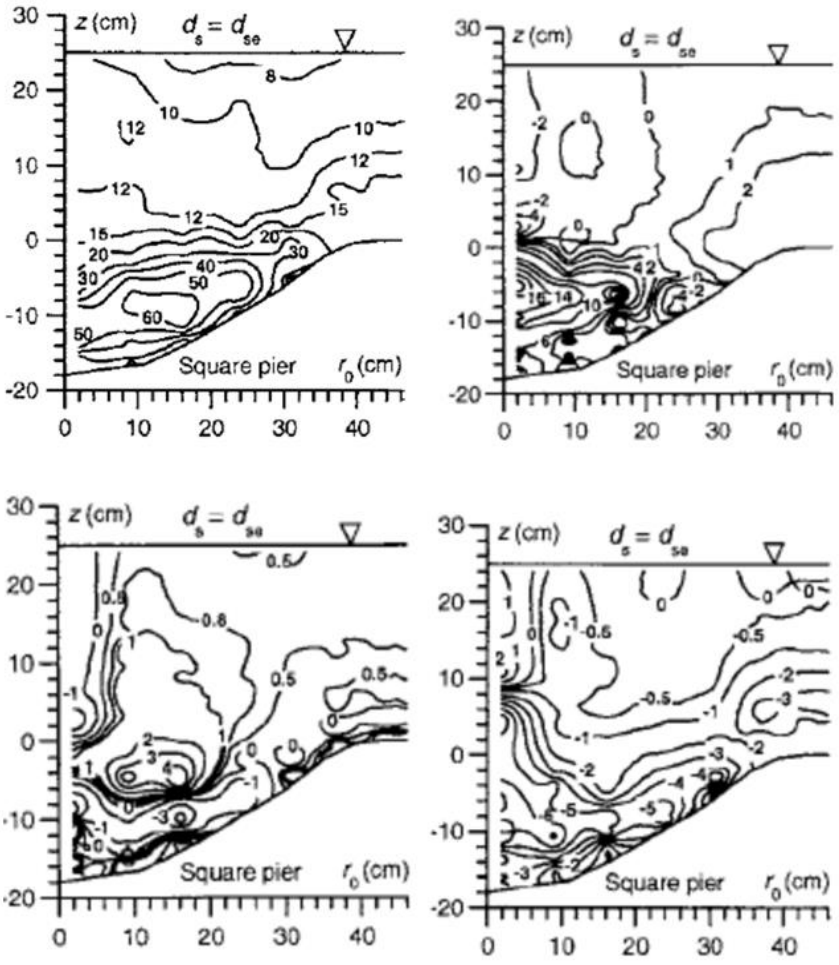

Figure 8: a) Total Kinetic Energy b) UV Reynolds Stress c) VW Reynolds Stress d) UW Reynolds Stress (Raikar & Dey, 2007)

In this study, the authors compared the scour and velocity fields in among similarly sized square and circular piers (Dey & Raikar, 2007). By examining Figure 9, one can see in both cases the maximum scour occurred at the front of the pier, and that the circular pier produces less scour than the square pier.

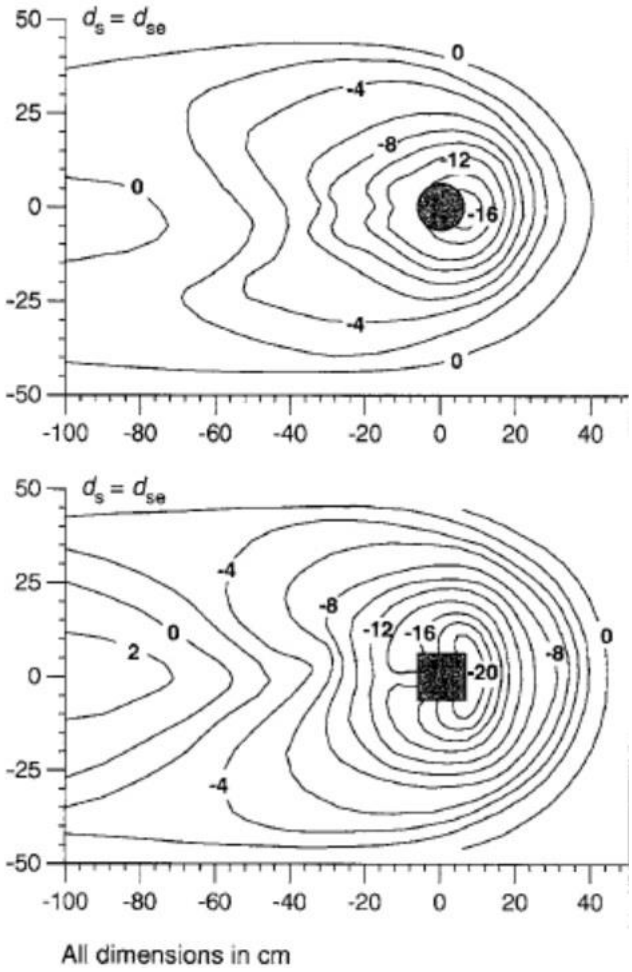

Figure 9: Scour pattern due to a circular and due to a square pier; flow from right to left (Raikar & Dey, 2007)

2.5 Equilibrium Scour time

In laboratory experiments, it is important to determine when the scour hole stops developing. This is known as equilibrium scour and is an intense area of research. When research began in the 1950s, it was found that while the scour process is quick at the start, it takes a long time to reach equilibrium (Chabert, 1956).

Ettema classified scouring into 3 phases which he called the initial phase, principal phase and the equilibrium phase (Ettema, 1980). He considers that a scour hole has reached equilibrium when its depth does not “practically” change anymore. Researchers have been attempting to define and agree upon what can be considered equilibrium scour. For example, Melville and Chow consider that equilibrium scour has been reached when the scour hole changes less than 5% of the pier diameter in a period of 24 hours (Melville, 1999). Researchers such as Oliveto argue that the scour hole never actually stops changing (Oliveto, 2002).

2.6 Constriction Scour

Constriction scour occurs due to the increased water velocity at a river constriction. An example of this would be a constriction in the floodplain caused by rocks which prevent the river from migrating (Queensland, 2013). By using the continuity principal, one will find that as the flow area decreases due to the constriction, the velocity must then increase, which increases shear stress causing scour. However, as scouring occurs, the stream deepens which increases the flow area. After some time, an equilibrium scour depth is reached.

Constriction scour can be combined with local scour at a bridge pier causing failure. Therefore, it is an important phenomenon to study. Illustrated below is a schematic of how constriction scour occurs (Dey & Raikar, 2005).

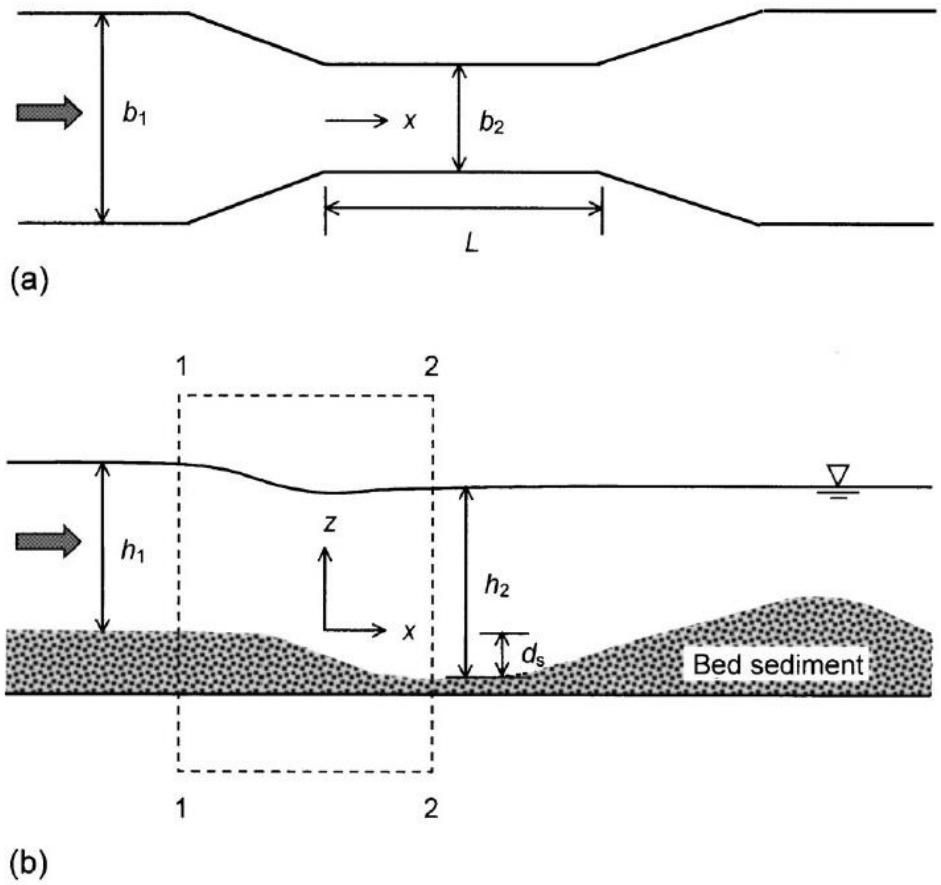

Figure 10: a) Plan view of a flume to examine constriction scour b) profile view of a constriction scour experiment (Dey & Raikar, Scour in Long Contractions, 2005)

It has been found that as the constriction narrows, the scour depth increases as seen in Figure 10. This can be explained because the increased acceleration caused by the narrowing will cause scouring. Further, for a given constant constriction ratio, scour increases with flow depth, except for the highest flow depths (Raikar, 2005).

The flow field around a constriction was studied both numerically as well as experimentally by Duc and Rodi (2008). The flow separates from the boundary at the expansion as seen by the low velocity values in that location (Figure 11). This experiment found that deposition began after the expansion when the velocity decreased (Duc & Rodi, 2008). Since the velocity was low, the water had less kinetic

energy and could no longer carry the same amount of sediments so deposition occurred (Figure 12).

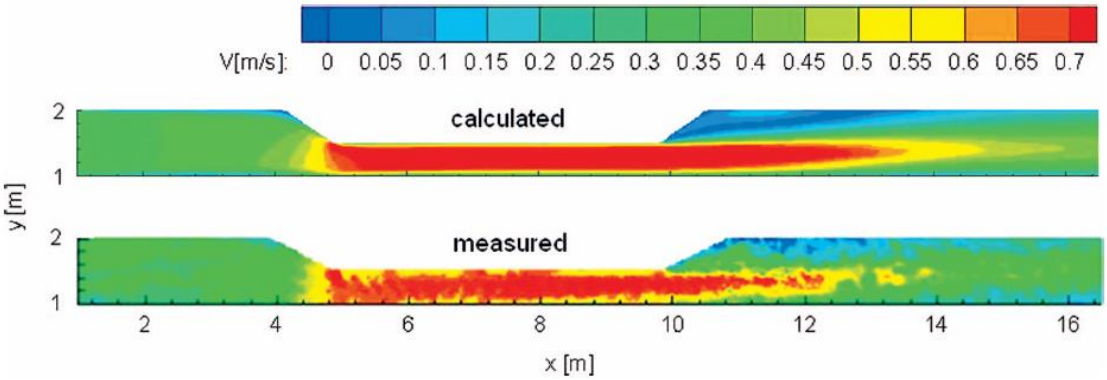

Figure 11: Experimental and numerical results of the Flow field in a constriction; flow from left to right (Duc & Rodi, 2008)

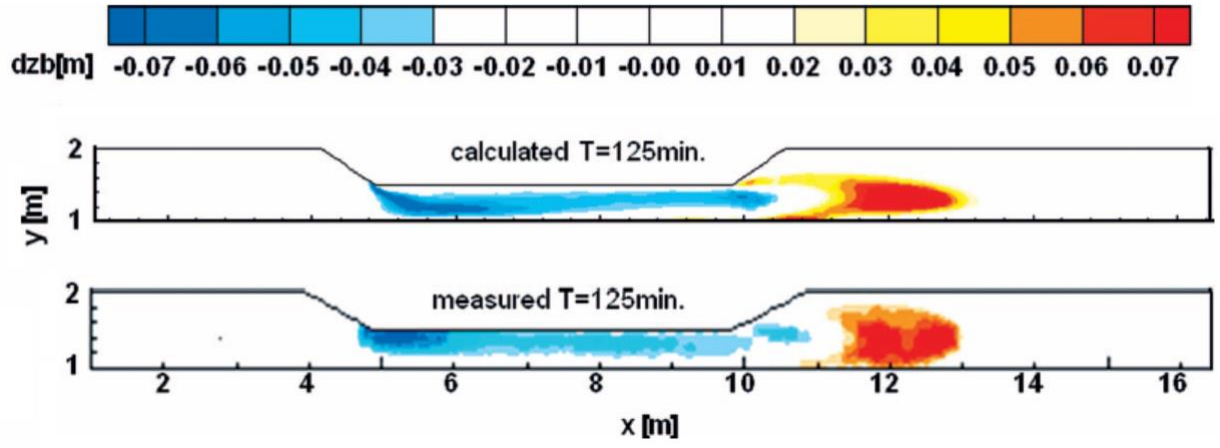

Figure 12: Experimental and numerical results of the scour distribution in a constriction; flow from left to right (Duc & Rodi, 2008)

2.7 Pier and Contraction Scour

When designing bridges, engineers must take into account total scour which combines both pier and contraction scour. Contraction scour can come from abutments built to support the bridge as well as from the natural narrowing of the river. It is advantageous to build bridges at natural river constrictions in order to decrease the span of the bridge and thus save on material costs.

Figure 13 displays the typical scour pattern at a bridge. The total scour is broken up into pier and constriction scour. (Dot, 2013).

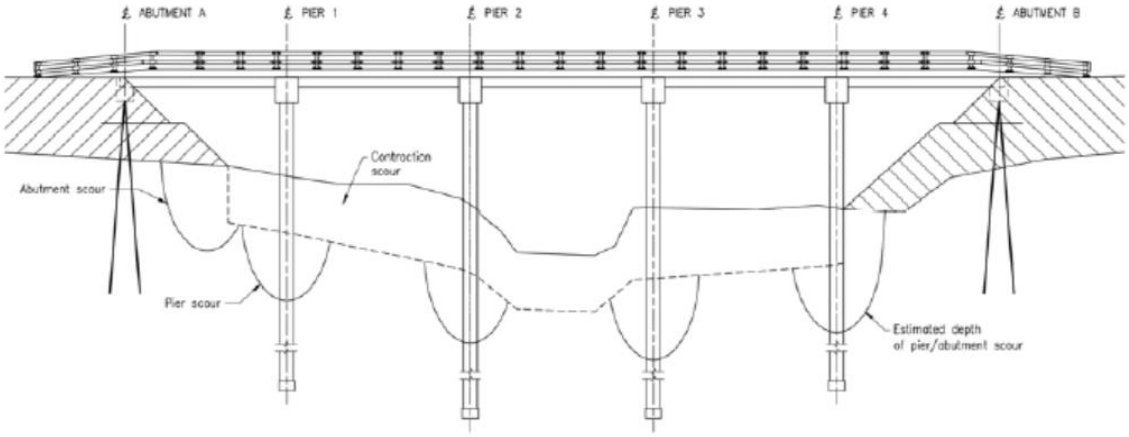

Figure 13: Constriction and Pier scour pattern at a typical bridge (Dot, 2013)

In general, engineers add up the depths caused by contraction and pier scour linearly in order to be conservative (Arneson et al, 2012), (Dot, 2013). However, there is limited research in the applicability of this assumption.

A recent study examined how the scour depth varied due to the distance between the pier and the abutment. It was found that when the pier was located immediately next to the abutment, the scouring was mainly caused by the abutment. As the pier was moved further away, it was observed that the pier scour had a greater contribution to the total scour (Kwaku Oben-Nyarko, 2011). It should be noted that the pier used for this study was extremely narrow compared to the width of the abutment so was less likely to cause scour as compared to larger piers.

The study presented in this thesis examines the effect of scour due to both a constriction and a pier and would appropriately apply to situations in which a bridge is

built at a river narrowing. The main goal is to examine the assumption of the linear addition of constriction and pier scour. As explained above, the current assumption is that the total amount of scour is the linear sum of pier and constriction scour.

Figure 14 shows a practical situation to which the results of the thesis could be applied (Conway, 2004). As explained above, scouring is caused by the acceleration of water due to the narrowing of the channel which is compounded by local scour at the bridge piers.

Figure 14: A bridge built across the Knik River, Alaska. Guidebanks result in a channel constriction thus the river is subject to both local and constriction scour (courtesy of Jeff Conway, United States Geological Survey)

2.8 Motivation:

Through a detailed review of current literature, it was found that a study on the combined effects of pier and constriction scour does not exist. Much work has been accomplished studying both of these phenomena as they occur separately resulting in equations to predict the scour depth. As previously mentioned, the current industry

practice is to determine the scour depth from the constriction and pier scour separately and use the linear sum to predict the amount of total scour for a case in which both types of scour are present (Arneson, Zevenbergen et al, 2012). However, through a series of experiments which examined blockage ratios from 0.1 to 0.6, this novel study shows that the assumption of linear addition is at times not conservative. Since the constriction of bridges within a constricting channel is a common practice, this practical study will shed light on how to increase safety by decreasing bridge failures.

3 Methods:

3.1 Experimental Program

In this study, the experiment was performed in two flumes. The large flume had a length of 11.94m and a width of 1m while the smaller flume had a length of 2m with a width of 0.61m (Table 1). Throughout the experiments, sand with a median diameter of 1mm was used.

In the smaller flume, the constrictions had widths of 0.148m. The pier used in this flume had a width of 5cm. Within the larger flume, the constrictions had widths of 0.242m and angles of 45 degrees. In this case, the pier had a diameter of 8.3cm. These dimensions were derived through Froude number scaling.

Both experiments were run such that without the influence of the constriction or pier, there was no sediment movement. This corresponds to a discharge of 0.00428m^3/s for the small flume and 0.017 m^3/s for the large flume. In all flume runs, uniform flow was achieved by ensuring approximately equal flow depths (within measurement precision

of ~1 mm) at the upstream and downstream ends of the flume. The bed slope on the large flume is 0.007 while for the small flume it was close to 0.

Table 1: Summary of the properties of the flumes, constrictions, piers and flow rates for the experiments

		Flow Properties				Constriction Properties(cm)		Pier Properties		Measurements		
Test Number	Test Description	**Upstream Vel (m/s)**	**Flow depth (cm)**	**Flume Width**	**Fr**	**Width**	**Length**	**Width (cm)**	**Length (cm)**	**Flow Rate (m3/s)**	**Elev. Above initial bed (cm)**	**Relative Depth (%)**
1	2 Square Pier + Constriction	0.19	0.125	1	0.17	24	68.5	8.2	8.2	0.024	6	48
2	Constriction Alone	0.23	0.125	1	0.21	24	68.5	None	None	0.029	6	48
3	2 Square Piers Alone	0.28	0.125	1	0.25	None	None	8.2	8.2	0.035	6	48
4	2 Square Pier + Constriction	0.18	0.076	0.61	0.21	14.6	50	5	5	0.008	2	26
5	Constriction Alone	0.17	0.076	0.61	0.20	14.6	50	None	None	0.008	2	26
6	2 Square Piers Alone*	0.18	0.076	0.61	0.20	None	None	5	5	0.008	2	26
7	Elliptical Pier Alone	0.18	0.076	0.61	0.20	None	None	5	10	0.008	2	26
8	Circular Pier Alone	0.18	0.076	0.61	0.20	None	None	5	5	0.008	2	26
9	Constriction + Elliptical Pier	0.18	0.076	0.61	0.20	14.6	50	5	10	0.008	2	26
10	Constriction + Circular Pier	0.18	0.076	0.61	0.20	14.6	50	5	5	0.008	2	26
11	1 Square Pier	0.18	0.076	0.61	0.20	None	None	5	5	0.008	2	26
12	1 Square Pier + Constriction	0.18	0.076	0.61	0.20	14.6	50	5	5	0.008	2	26

3.1.1Rationale for Tests

Initially, three experiments (test 1 to 3) were run in the large flume at the University of Ottawa. The large flume provided sufficient length for the boundary layer to develop making the conditions similar to what would be expected in a real river. The velocity field was measured for these tests in order to compare with tests 4-6 which had the same arrangement of piers and constrictions but were performed on the smaller flume. It was found that the small flume was not long enough to provide room for the boundary layer to develop fully but through comparison of the flow field between tests 1-3 and tests 4-6, it was found that the flow field around the piers and constrictions was similar to a flow field with a fully developed boundary layer.

From this, it was concluded that despite the short length of the small flume, it provided reasonable results. Therefore, tests 7-12 were performed in the small flume in order to save time. For these tests, only the scour pattern was recorded due to time constraints.

3.2 Equipment Used

3.2.1 Acoustic Doppler Velocimeters for Turbulent Flow Field

In order to measure the flow field in the flume, Acoustic Doppler Velocimeters (ADV) were used. The particular ADV model was a Vectrino+, created by Nortek International, which measured the turbulent three-dimensional velocity with a tolerance of ± 0.1mm/s in a small sample volume located 5 cm away from the unit.

The velocity is determined by measuring the phase difference between backscattered acoustic pulse (Rennie, 2010). The acoustic instrument sends a sound wave that is reflected off of particles in the water as seen in Figure 15 (Water Survey of Canada, 2004). The water was seeded with particles which were spherical hollow glass

spheres with a diameter of 10 microns and a specific gravity of 1.1. Particles with these parameters were chosen so they would follow the flowfield.

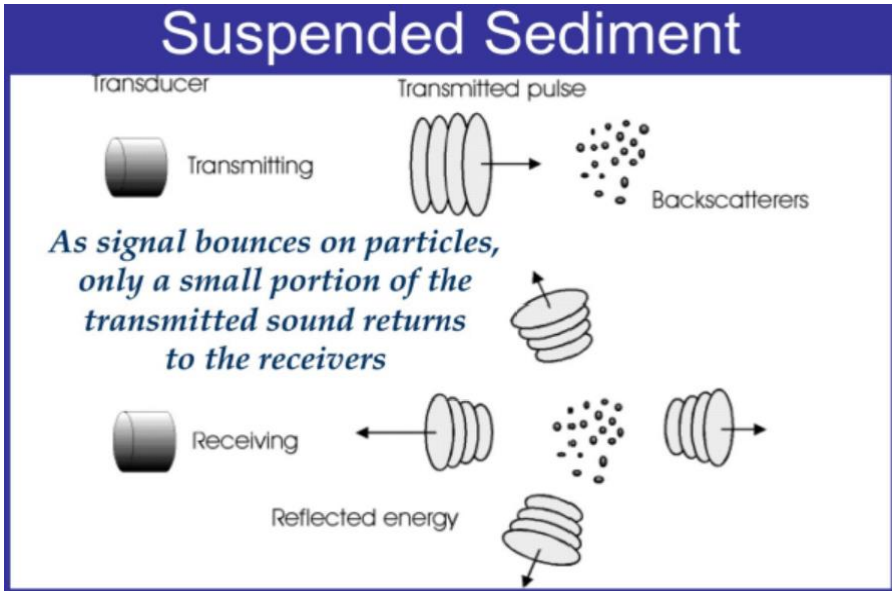

Figure 15: The schematic of acoustic measurements (Environment Canada)

In general, acoustic velocimetry employs the assumption that the particle is moving at the velocity of the water. By calculating the Doppler shift in frequency of the reflected pulse, which is due to particle velocity along the acoustic beam axis, one can determine the flow velocity. The Vectrino+ incorporates pulse coherent signal processing, in which the Doppler phase shift between sequential pulses is used to measure velocity. The velocity within the sample volume is calculated from the following equation

$$b_i = c\frac{\frac{d\theta}{d\tau}}{4\pi f} \quad (9)$$

where c is the speed of sound, τ is the time between pulses in a pulse pair, f is the acoustic operating frequency (f)., dθ is the Doppler phase shift for a pulse pair, and

$\frac{d\theta}{d\tau}$ is the average phase shift for several pulse pairs. Averaging is used because if only one pair were used, the correlation between the pulses would be too close to one.

Using several pairs also allows the user to check the data for quality assurance and reduce computational time (Water Survey of Canada, 2004). Figure 16 shows a typical ADV sampling methodology (Nortek).

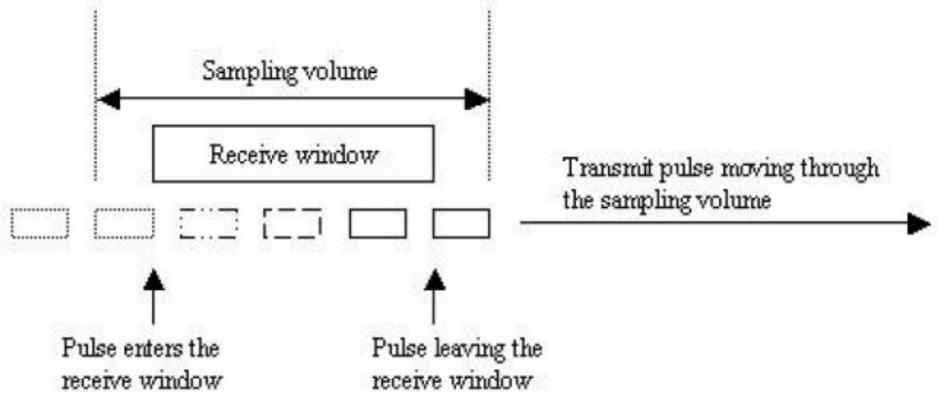

Figure 16: Schematic of ADV measurement (Nortek)

The Vectrino+ incorporates four receive beams, thus velocity is measured along four axes, from which a Cartesian three-dimensional velocity is determined, as well as a redundant vertical velocity that is used as an estimate of error.

A major advantage of acoustic measurements is that the sample volume is away from the device which means that the flow field is not disturbed. This is also the case with optical techniques but it has been found that optical techniques do not function as well in river environments because the turbidity is too high. Therefore, acoustic techniques are frequently used in river engineering.

In each flume run, ADVs were used to measure the spatially distributed velocity field at a single horizontal plane. ADVs were also used to measure vertical profiles of velocity at key locations. At each sampling point three-dimensional velocity data were recorded at a rate of 100Hz with a sampling time of 2 minutes. Two configurations of the ADVs were used in order to best obtain velocity measurements throughout the flow field. The

downlooker measured velocity in a sample volume below the device, and this configuration was used to measure the spatially distributed field at a single horizontal plane. The first available sampling point for the downlooker was 6 cm below the water surface. The second configuration was a sidelooker, which had a sample volume located 5.5cm horizontally adjacent to the probe tip. It was necessary to use both arrangements because of the limited flow depth. The first available sampling point for the sidelooker was approximately 2 cm below the water surface. Thus, the sidelooker allowed for velocity measurements closer to the water surface, and it was used to complete vertical profiles of velocity at some locations. Within the large flume, vertical profile measurements were taken at 0.5cm, 1cm, and 2cm from the bed and additionally with increments of 2cm until 10cm from the bed. For the small flume, data points began at 2.5cm from the bed and with increments of 0.5cm.

The locations in which data were gathered for the various experimental runs are described in detail in section 3.5

Furthermore, as explained in detail in section 3.3 and section 3.6, after processing the data with Matlab, Tecplot was used to interpolate the flow field for each flow statistic.

3.2.2 Bathymetry

The bathymetry was measured using the DISTO Pro4 handheld laser. The accuracy of the measurement was +/- 1.5mm. Generally, a 5cm by 5cm measurement grid was used but the density was increased to 2cm by 2cm for areas with more erosion.

3.3 Analytical Methods:

3.3.1 Turbulent Parameters

Data collected using the ADVs were processed using a Matlab code developed by Dr. Rennie. The mean velocities in the X,Y,Z directions as well as turbulence parameters were calculated. Some of these turbulence parameters included the Reynolds stress and turbulence kinetic energy (TKE). The vorticity in the Z direction was then calculated within Tecplot. This section briefly defines each of the calculated parameters.

3.3.2 Turbulent Kinetic Energy

The TKE is the sum of the mean of the product and square of each of the fluctuating components of the velocity fluctuations (Jamieson et al, 2013). This is mathematically represented by the following equation:

$$TKE = \frac{1}{2}\left(\overline{u'^2} + \overline{v'^2} + \overline{w'^2}\right) \quad (10)$$

Where u', v', and w', are respectively the fluctuating components of velocity in the X, Y and Z directions.

3.3.3 Reynolds Stress

Turbulent momentum exchange can be estimated by calculating the Reynolds stress terms. In the notation shown in Table 2 below, the subscripts show the plane in which the stress acts upon and the direction of shear stress.

Table 2: Reynolds stress notation (E. C. Jamieson, 2013)

Measurement	Stress Component	Plane	Direction	Velocity Gradient

$-\rho\overline{u'w'}$	τ_{uw}	yz	Z	$\frac{\partial_w}{\partial_x}$
	τ_{wu}	yx	X	$\frac{\partial_u}{\partial_z}$
$-\rho\overline{u'v'}$	τ_{uv}	yz	Y	$\frac{\partial_v}{\partial_x}$
	τ_{vu}	zx	X	$\frac{\partial_u}{\partial_y}$
$-\rho\overline{u'w'}$	τ_{vw}	zx	Z	$\frac{\partial_w}{\partial_y}$
	τ_{wv}	yx	Y	$\frac{\partial_v}{\partial_z}$

3.3.4 Vorticity

The total vorticity is calculated by adding the vector sum of the individual components of rotation. The average of the angular velocity perpendicular to each axis of rotation defines the rotation about that axis. For the Z vorticity which was calculated in the results, this is given by the following equation. The first term represents the angular velocity about the x axis while the second represents angular velocity about the y axis (Jamieson et al, 2013).

$$\omega_z = \frac{\partial \overline{V}}{\partial x} - \frac{\partial \overline{U}}{\partial y} \quad (11)$$

Where ω = vorticity, and$\overline{U}$, $\overline{V}$ = mean velocities in the x, y directions respectively

3.3.2 Data Filtration

In order to remove data spikes, a series of despiking filters was employed. A velocity value in a time series was deleted if: 1) the two estimates of vertical velocity measured by the Vectrino+ ADV differed by more than 0.1 m/s, or 2) the apparent velocity acceleration between sequential velocity measurements exceeded gravitational acceleration, or 3) the velocity value was more than three standard deviations above the mean for the time series. Finally, the despiked data time series was evaluated for measurement noise by comparison of the observed turbulent velocity spectrum to the expected -5/3 power law, and if excessive noise was observed, high frequency noise as well as low frequency oscillations were removed using a 4th order Butterworth filter (Rennie and Hay 2010).The cutoff frequency was 20Hz which was reasonable as the data were collected at 100Hz., and noise did not substantially influence the observed spectra at frequencies lower than 20 Hz.

It was found that for the one test case of the large flume with 2 piers, the ADV ambiguity velocity was exceeded (Rennie and Hay 2010). The ambiguity velocity is given by the following equation

$$v_{amb} = \pm \frac{c}{4\tau f} \quad (12)$$

where c = the speed of light, $\tau = time\ lag\ between\ pulses\ in\ a\ pulse\ pair,$ and f =acoustic frequency.

The ambiguity velocity is set by the user which changes the time lag between pulse pairs. If the measured velocity is greater than the ambiguity velocity, the Doppler phase

shift will be shifted by 2pi radians (i.e., 2 x the ambiguity velocity) and must be unwrapped by either adding or subtracting this amount.

3.3.3 Phase Wrapping

When setting up the experiment, the user set the ambiguity value to be lower than the measured velocity which can result in wrapped data in the streamwise direction.

For the experiment using two square piers and constriction (C32) within the large flume, it was found that phase wrapping occurred. This happened because the setting for the ambiguity velocity was exceeded. Initially, the streamwise velocity obtained by the Matlab processing code was far smaller than expected which aroused suspicions of phase wrapping. Upon further examination, it was found that the data were indeed wrapped. Figure 17 shows an example of wrapped data. It is expected that there should only be one band, which represents a mean velocity and turbulent fluctuations for that particular sampling location.

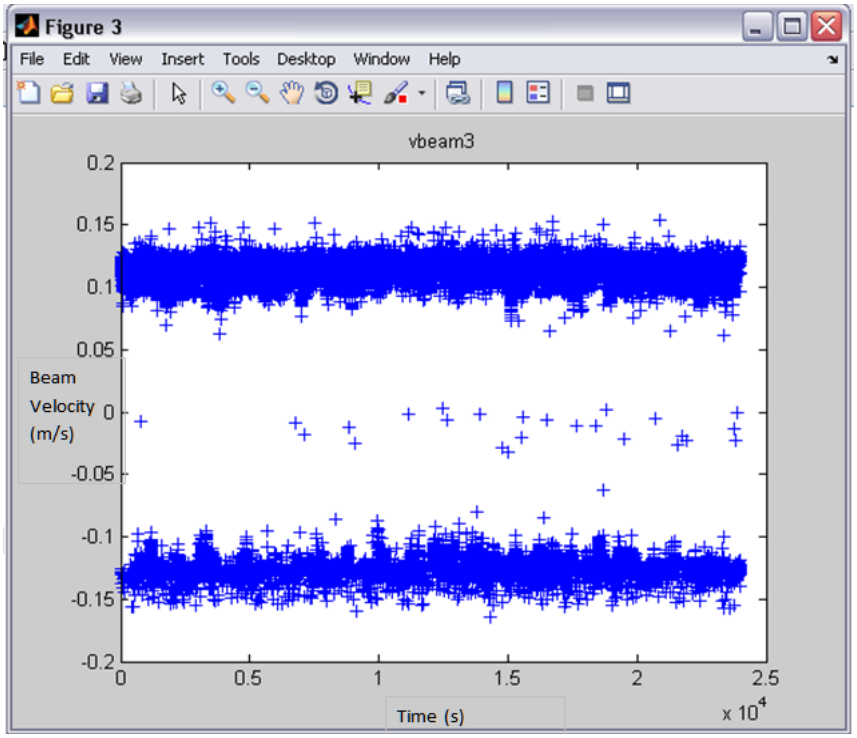

Figure 17: Beam Velocity from ADV showing wrapped Data

An unwrapping procedure was implemented in order to recover the data. While this was successful in the streamwise direction, the results in the cross stream and vertical directions were more ambiguous. Since reliable data were not available for two of the three velocity components, it was not possible to calculate turbulent statistics such as the vorticity or the Reynolds stresses for the case with two square piers and constriction in the large flume.

In order to resolve the issue of wrapped velocity data, an unwrapping procedure was used similar to Rennie 2010 (Rennie & Hay, 2010). The general procedure was to use a transformation matrix to convert the 3 dimension velocities back into beam velocities that were recorded on the ADV. After this, a judgement call was made as to whether the velocity data were phase wrapped and if so, the addition or subtraction of the

phase velocity was used in order to unwrap this data. A total of 22 velocity points were unwrapped.

It was found that depending on whether the phase velocity was added or subtracted, the resulting velocity field would differ. In the cases where it was not obvious as to whether unwrapping should proceed with addition or subtraction, both were tested. The obtained velocity values were then compared to the small flume and the one that most resembled this was used. This adds an element of uncertainty and since the small flume values were used to check the flow field of the large flume, it is difficult to compare these two.

This unwrapping procedure was successful for the streamwise velocity but it was not possible to unwrap the cross stream and vertical velocities. These velocities are required to calculate the Reynolds stresses, vorticity as well as total kinetic energy so for the case with simultaneous pier and constriction scour in the large flume, these parameters were not obtained.

The scour field for this case was collected accurately but due to the fact that the unwrapped procedure was only successful in the streamwise direction it was not possible to correlate turbulence parameters to the scour field.

3.4 Scaling

In many physical problems, scaling is used in order to save time and money. Generally, experiments are performed on a smaller scale and the results are then applied to a full-scale prototype situation.

In order to properly scale a physical experiment, engineers use the concept of similitude. The three types of similitude are geometric, kinetic and dynamic (Prashun, 1992). Geometric similitude requires that the geometry of the model and prototype are similar. Therefore, the length ratio as defined by the length of the model divided by the length of the prototype must be the same for all dimensions. In order to satisfy kinetic similitude, the velocity and acceleration of the flow must be scaled between the model and prototype. Dynamic similitude requires that forces such as pressure, gravity and viscous forces are scaled correctly (Prashun, 1992).

In problems involving a free surface and gravity driven flow as seen this study, engineers frequently make use of Froude Number scaling. If one assumes a constant value for gravitational acceleration, the Froude law is

$$\left(\frac{V}{\sqrt{L}}\right)_m = \left(\frac{V}{\sqrt{L}}\right)_p \quad (12)$$

Where
V = velocity
L = Length
From (Prashun, Fundamentals of Hydraulic Engineering, 1992)

Scouring presents an important transportation problem so the results from laboratory tests are often to be applied back into field cases. Due to the cost, it is difficult to perform full sized tests and laboratory scales are often much smaller than in reality. Therefore, if the model is much smaller, a smaller sediment size should be used. However, when the sediment becomes too small, interparticle forces which are not found at prototype scale begin to play a role (Lee & Sturm, 2009). In addition, it is impossible to scale for gravity.

It has been found that the scour depth depends on the ratio of the width of the pier over the median sediment size (b/d_{50}). An investigation was performed to study the effect of scaling the sediment size by studying scour over a range of b/d_{50}. This was accomplished by using 3 different sized piers and 3 different sized sediments (Lee & Sturm, 2009). It was found that by distorting the ratio of b/d_{50}, the horseshoe vortex which plays a large role in scouring is distorted. This generally causes larger scour depths to be measured in the laboratory as compared to in the field (Lee & Sturm, 2009).

3.4 1 Scaling for the Experiment

3.4.1.1 Length Scaling

For this experiment, it was decided that the width of the flumes be used to scale between the two flumes. The large flume has a width of 1m while the small flume is 0.61m wide. The following equations were used in order to obtain the depth ratio. Substituting the flow depths gives a scale ratio of 1.64. Therefore, the dimensions of the piers and constrictions were set to be 1.64 times larger in the large flume as compared to the small flume. The complete dimensions are given in Table 1.

$$\text{Scale Factor: } D_r = \frac{D_m}{D_p} \quad (13)$$

Where
Dm = model dimension
Dp = prototype dimension
(Prashun, Fundamentals of Hydraulic Engineering, 1992)

3.4.1.2 Froude Scaling

This analysis provided the dimensions for the piers based on the width of the flume and Froude Scaling was used in order to determine the flow rate in the two flumes. Since this experiment revolves around gravity driven flow with a free surface, Froude scaling is appropriate.

$$Froude\ number = \left(\frac{V}{\sqrt{gy}}\right)_m = \left(\frac{V}{\sqrt{gy}}\right)_p \quad (14)$$

(Prashun, Fundamentals of Hydraulic Engineering, 1992):
Where
V = velocity
L = Length

For the flow analysis, the experiments that were completed first in the large flume were scaled down to the small flume while making sure that both flumes are run at the same Froude number.

The flow depth in the large flume was 12.5cm with a velocity ranging from 0.19m/s to 0.28m/s which yielded Froude numbers between 0.17 to 0.25. The flow depth between the large and small flumes was scaled using the scale factor of 1.64. Since the large flume was run with a flow depth of 12.5cm, the depth for the small flume was to be set at 7.6cm. Knowing the flow depth and velocity, the next step was to determine the flow velocity in order to obtain a Froude number of 0.2. This was calculated to be about 0.2m/s.

One thing to note is that there is a range in the approach velocity within the large flume. In order to maintain a consistent flow depth of 12.5cm, the downstream gate had to be adjusted. In order to maintain uniform flow, the discharge had to be slightly changed which is what caused the variation in the approach velocity which then varied the Froude number.

This was not avoidable and is a consequence of running a large flume. The case with only two square piers in the large flume was particularly affected. Therefore, scaling back from the case with the constriction and two piers simultaneously was used to determine the scouring that would have occurred if this experiment had with run with the same Froude number as the other runs. More detail on this procedure is discussed in section 4 which details the results of the experiments.

3.4.1.3 Sediment Scaling

Due to the fact much of the experiment revolved around scouring, it would also be ideal to scale the sediment when moving between the two experimental set ups. This is known as sediment similitude and is given by the following expression.

$$\left[\frac{\tau_0}{(\gamma_s-\gamma)d_s}\right]_m = \left[\frac{\tau_0}{(\gamma_s-\gamma)d_s}\right]_p \quad (15)$$

Where
τ_o= shear stress, γ= specific gravity of water, γ_s=specific gravity of sediment, d_s= diameter of sediment, m = model parameters, p = prototype parameters

The optimal case would be to run both experiments at the incipient clear-water scour conditions.

In order to achieve this type of scaling, the sediment size between the two runs must be different. For this experiment, the two sediment sizes that were available had median diameters of 1mm and 0.7mm. In an initial test case, it was found that the 0.7mm sediment would scour to the bottom when run at the conditions required for Froude scaling between the large and small flumes. Scouring to the bottom would mean that it would not be possible to measure the scour depth so the decision was made to forgo perfect sediment scaling. Even so, the decision to use 1mm sand for both flumes ensured that clear water scour was achieved in both cases.

The large flume experiments were first run and the goal was to match the shear velocity of this to the small flume. The shear stress during the large flume experiment was calculated to be 0.026m/s with a water surface slope of 0.007 which represented a shear stress of 0.0262 close to the threshold of motion. Attempts were made to create conditions within the small flume to produce a shear stress that is close to the critical value by adjusting the slope while having the velocity and depth governed by Froude scaling. It was not possible to replicate sediment similitude given the restrictions set by Froude scaling so efforts were made to ensure that both flumes were run in clearwater conditions. Although clearwater conditions were observed, it is not possible to calculate the shear stress within the small flume because velocity profiles did not yield reasonable values and the slope of 0.005 was too high for the depth-slope product approach to be valid.

3.5 Data Gathering Locations

It required 2 and 5 hrs for equilibrium conditions to be met in the small and large flumes respectively. In order to save time, velocity measurements were completed upstream of the flume while scouring was occurring near the piers. When it was noted that scouring ceased, measurements were taken at the obstructions.

For the experimental set up, data were collected in such a form to optimize accuracy and save time. Therefore, a plan was devised such that data were taken at increased densities where more turbulence and sediment transport was expected. Figure 18, Figure 19 and Figure 20 show the planned data collection positions for the small flume while Figure 21, Figure 22 and Figure 23 show the actual data collection positions. It was found during the experiments, that some of the positions were not accessible due to the position of the piers, constrictions, and the water depth.

In the figures showing the data gathering locations, the green dots represent positions in which the data were to be collected at various depths resulting in a velocity profile. Due to time limitations, much of the spatial velocity data were only collected at one vertical position at a constant horizontal plane, which is represented by the red dots. It was expected that increased turbulence would occur at the constriction and also the area around the piers. An increased density of data gathering points was chosen at these locations in order to best capture how these velocity and turbulent parameters affect the scouring. A side-looking ADV was used for the profiles (green dots) while a down looking ADV was used for the rest of the data (red dots).

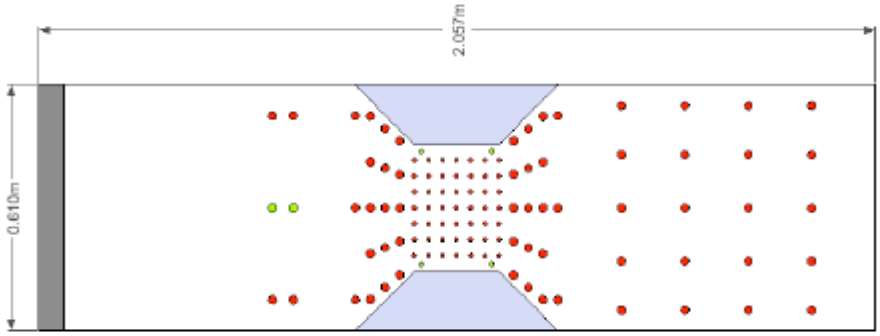

Figure 18: Planned data gathering locations for the constriction only in the small flume.

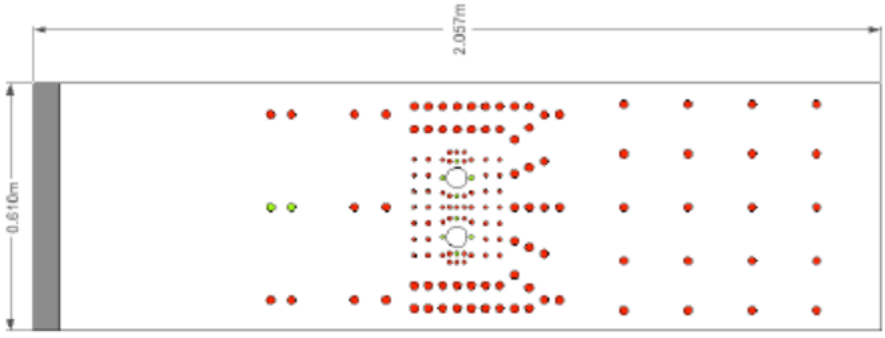

Figure 19: Planned data gathering locations for the piers only case in the small flume.

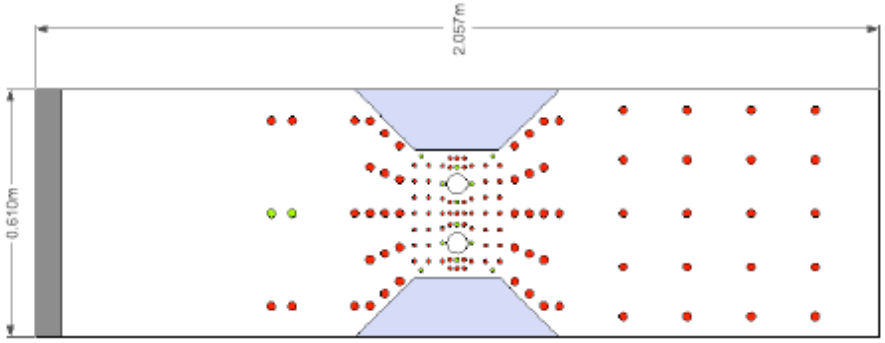

Figure 20: Planned data gathering locations for the constriction and the piers in the small flume.

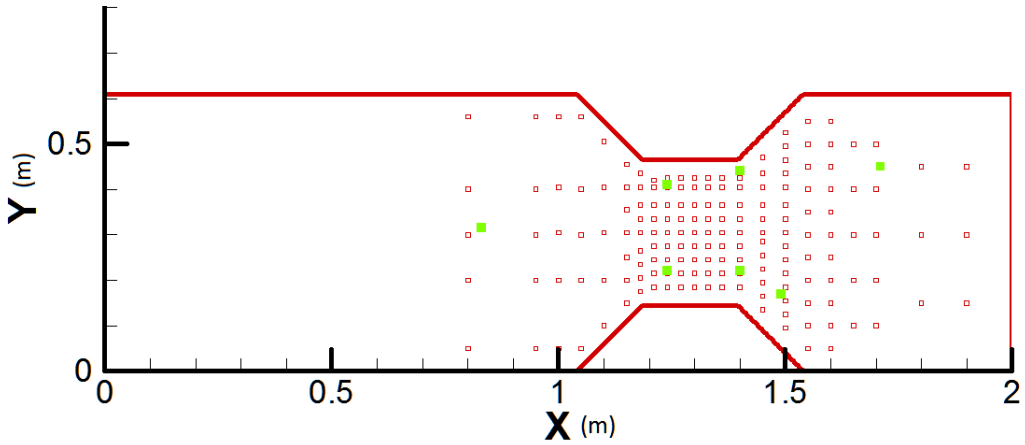

Figure 21: Actual data gathering location for the small flume with the constriction only

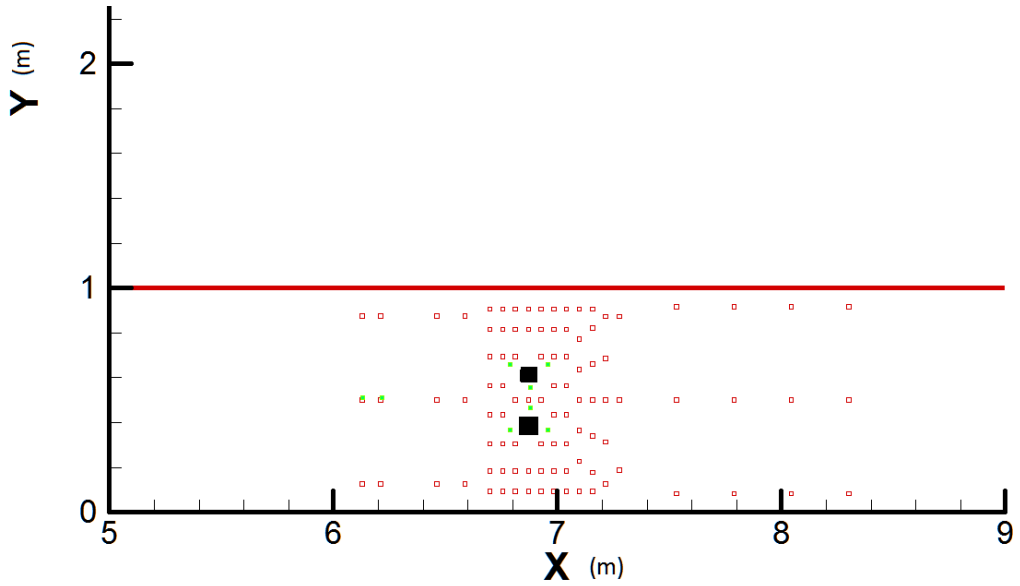

Figure 22: Actual data gathering locations for the small flume with the piers only

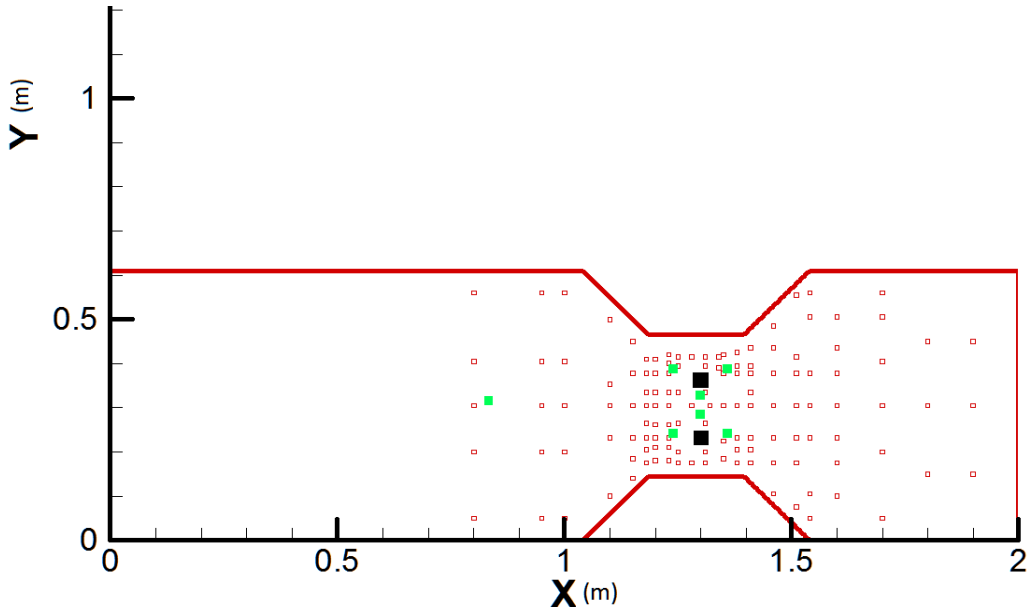

Figure 23: Actual data gathering locations for the small flume with both the piers and constriction

Figure 24, Figure 25, and Figure 26 show the actual data gathering positions for the large flume.

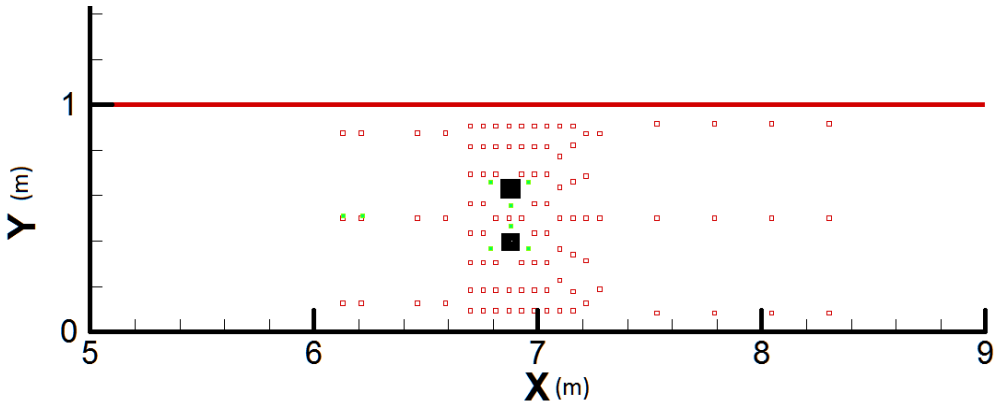

Figure 24: Actual data gathering locations for the large flume with the pier only

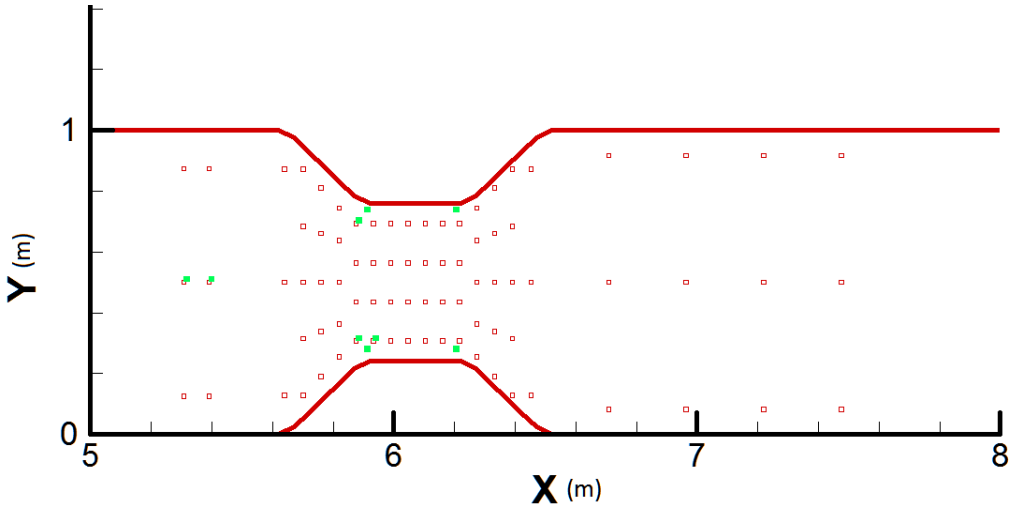

Figure 25: Actual data gathering locations for the large flume with the constriction only

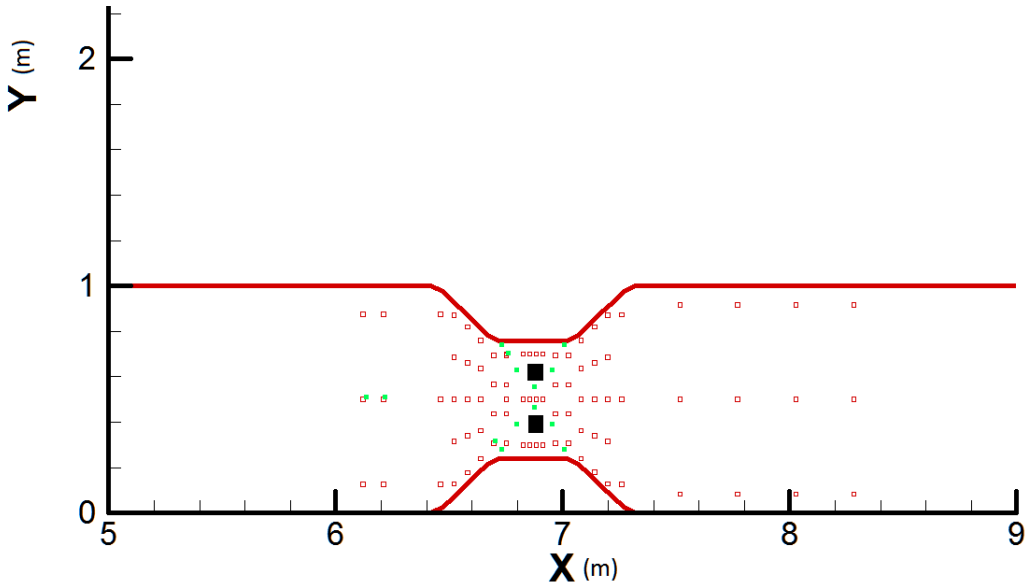

Figure 26: Actual data gathering locations for the large flume with both the constriction and the piers.

3.6 Tecplot

After the flow data were processed using Matlab, the visualization software, Tecplot was used. Tecplot was used to interpolate the flow data in order to provide visualization of the flow patterns. An example of this is shown in Figure 27 below. Also, a step by step guide to interpolation within tecplot is provided in the appendix of this thesis.

The mesh for interpolation was created using Sediment Simulation in Intakes with Multiblock Option (SSIIM). This mesh had 0.5cm squared grids for the small flume and 2.5cm squared grids for the large flume. Using Tecplot, the flow data were interpolated onto the mesh using kriging.

Tecplot was also used to interpolate and provide visualization for the bathymetric data.

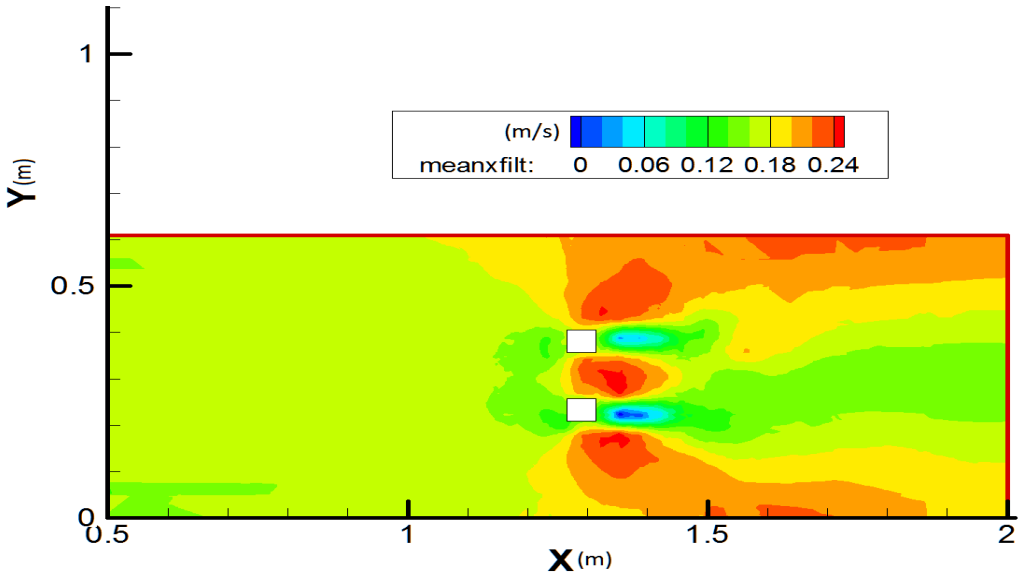

Figure 27: Example of Tecplot visualization: X velocity for 2 piers alone.

4 Results:

In the following section, development of the boundary layer and the results of the experiment using the post-processing software, Tecplot are presented. In both flumes, the flow field was measured for the cases with two square piers only (case C02), the constriction only (case C30), and both the two square piers and the constriction together (case C32). For these cases, the velocity in the streamwise, cross stream and vertical directions are plotted, followed by the Reynolds stresses. These statistics are followed by the turbulent kinetic energy, Z vorticity and the equilibrium bed bathymetry scour field. The order of data presentation has been chosen as such because one of the goals of the experiment is to find relations between the velocity field, turbulence parameters and how these influence the equilibrium scour conditions. Correlations between the turbulent properties and the scour field are mentioned in the results

section and then further expanded upon in the discussion. While examining the spatial distributions of velocity and turbulence parameters, the reader may find it useful to refer to the equilibrium scour patterns shown at the end of each sub-section. Furthermore, photos of the equilibrium conditions within the experiments are provided in the appendix to this thesis. Also, as explained in Section 5.5, it is useful to recall that spatially distributed velocity measurements were conducted at different relative depths in the large and small flumes.

This section concludes with the scour field for the experiments involving the elliptical and circular piers. Unfortunately, due to time constraints, the velocity field was not measured for these tests so the turbulent statistics are unavailable. However, comparisons between square, elliptical and circular piers have important industry applications because many piers are not square.

4.1 Boundary Layer Development:

When performing flume experiments, it is ideal to have a long enough flume such that the boundary layer is able to develop as it would in a real system. However, a large flume would also require more material thus a disadvantage would be the increased cost and time required to perform the experiments. It was found by (Kirkgozl & Ardichoglu, 1997) that it requires more than 50 flow depths to produce a fully developed boundary layer within a smooth flume. This is why the boundary layer is better developed in the large flume than its shorter counterpart.

Presented in Figure 29 is the velocity profile at two locations of the large flume before any obstruction is encountered. The velocity is low near the bottom due to the no slip condition and increases with height as expected. From this, one can conclude that the flow is developed because there is little change within the velocity profile moving downstream. The boundary layer development is shown for the small flume in Figure 29. Between the two downstream locations, there is a change in the shape of the velocity profile which means that the flow boundary layer has not quite developed.

It is ideal to have fully developed boundary layers in both experiments but due to the time constraints, it was found that more experiments could be performed if the small flume, thus the small flume was used. In order to compensate for the boundary layer development, the experiments were Froude scaled. In addition, as shown in the results below, the flow fields in the two flumes are very comparable in regards to spatial patterns of mean velocities and turbulence statistics.

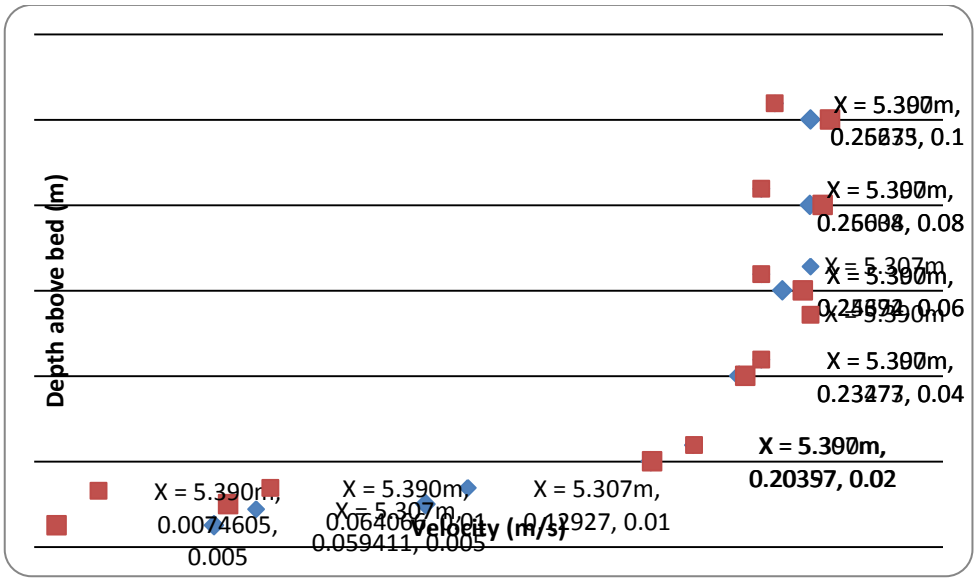

Figure 28: Boundary layer development for the large flume C30 case down the centerline at X = 5.307m and X = 5.390m

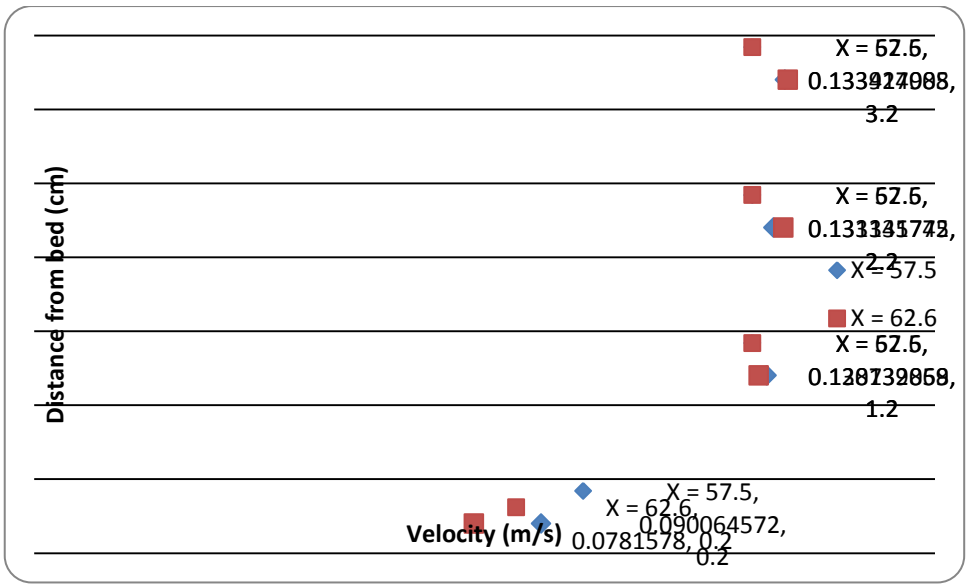

Figure 29: Boundary layer development for the small flume down the centerline at X = 57.5cm and X = 62.6cm

4.2 Two Square Piers Only

The following section shows the velocity, turbulence and scour distribution fields for the case with two square piers alone.

4.2.1 Streamwise Velocity

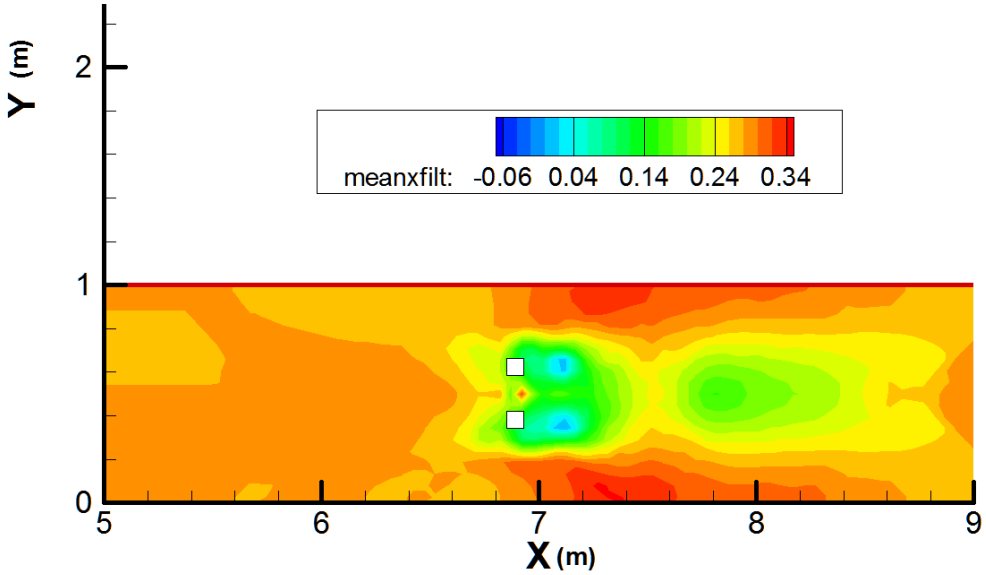

Figure 30: Large flume streamwise velocity with 2 piers only

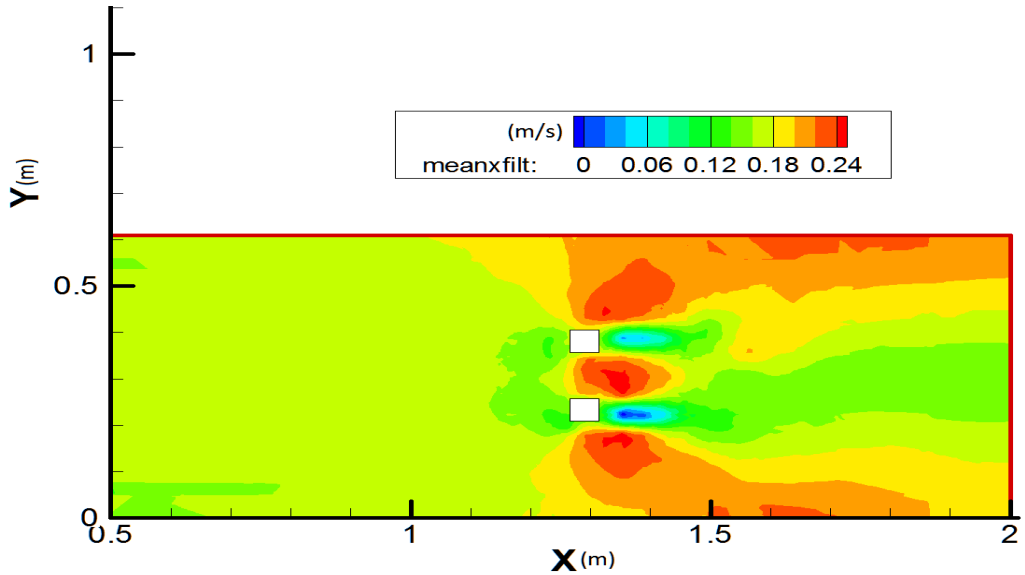

Figure 31: Small flume streamwise velocity with 2 piers

In the large flume, the approach velocity was approximately 0.26m/s. As the water impacted the piers, it slowed down in front of the pier as shown in Figure 30. There is a reduction in cross sectional area due to the space taken up by the pier so the velocity increased around the pier. There is also a low velocity behind the pier due to the wake that is generated. There was also a small section of high velocity in between the two piers. After around the 9m mark, the flow disturbance due to the piers dissipated and the flow conditions were close to what they were upstream of the pier.

Within the small flume, the approach velocity was around 0.18m/s as per Froude scaling. Similarly to the large flume, the streamwise velocity increased both between the piers and the constriction due to the lower cross sectional area within that location. There was also low velocity in the wake behind the pier. One observed difference between the large and small scaled experiments for the case of the pier only was that with the small flume, there was an area of maximum velocity in between the two piers

while this did not occur to the same extent in the large flume experiment as shown in Figure 31.

4.2.2 Cross Stream Velocity

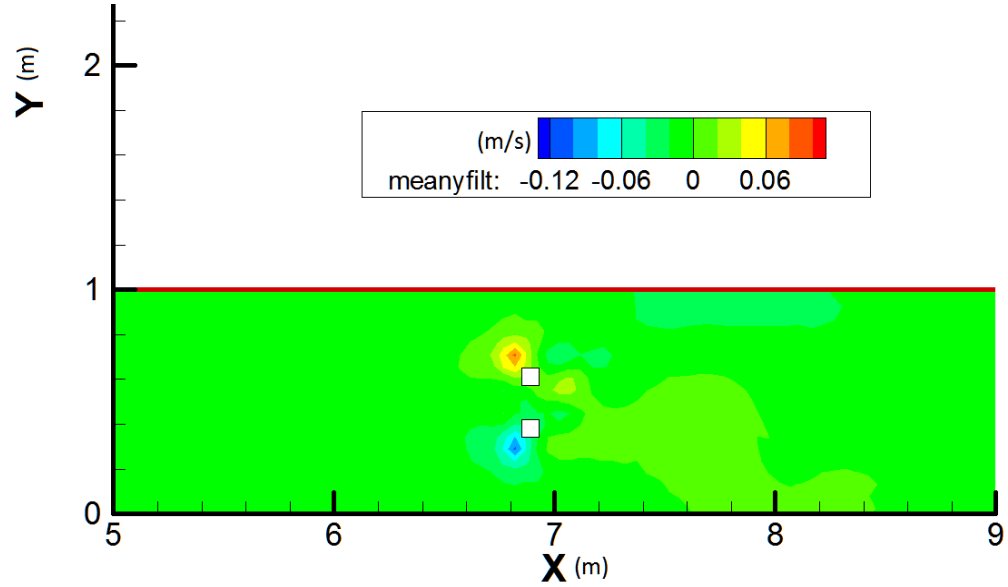

Figure 32: Large flume cross stream velocity with 2 piers only

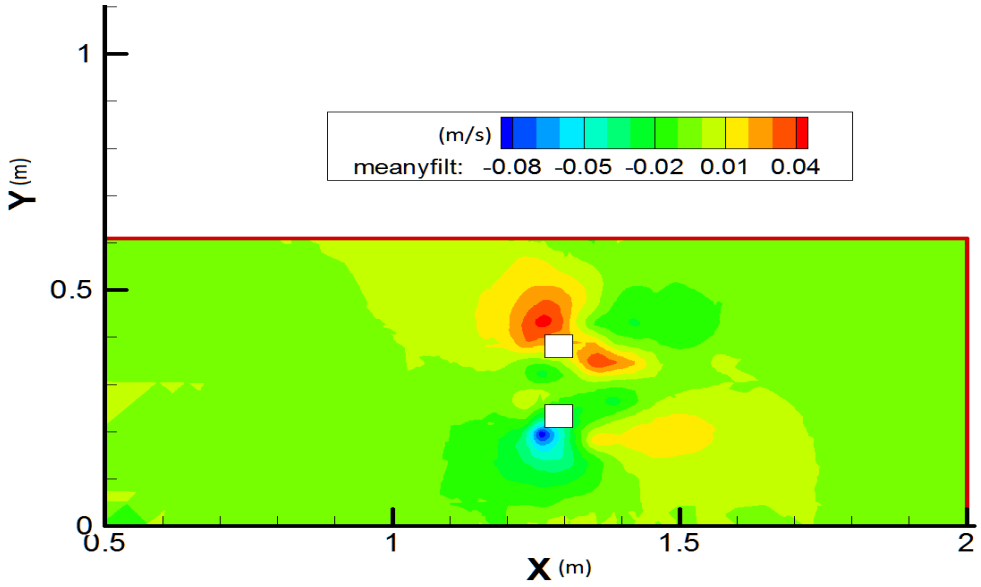

Figure 33: Small flume cross stream velocity with 2 piers only

For the majority of the flume, there was not much cross stream flow. However, once it reached the pier, the water flowed around the piers generating cross stream velocities as seen in Figure 32 and Figure 33. This was true for both the case of the large and small flume where the maximum magnitudes of cross stream velocity are 0.1m/s and 0.08m/s respectively. One observation is that the flow structure near the piers was more coherent within the small flume as opposed to the large flume. This was unlikely to be reflective of reality, but rather because there was a lower sampling density within the large flume. This resulted in less of the coherent structure being captured.

4.2.3 Vertical Velocity

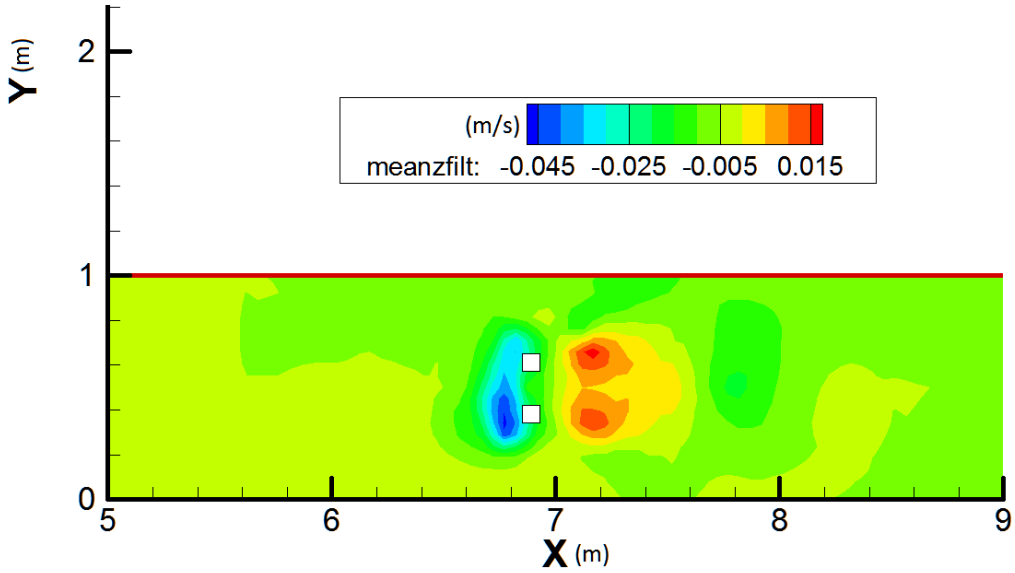

Figure 34: Large flume vertical velocity with 2 piers only

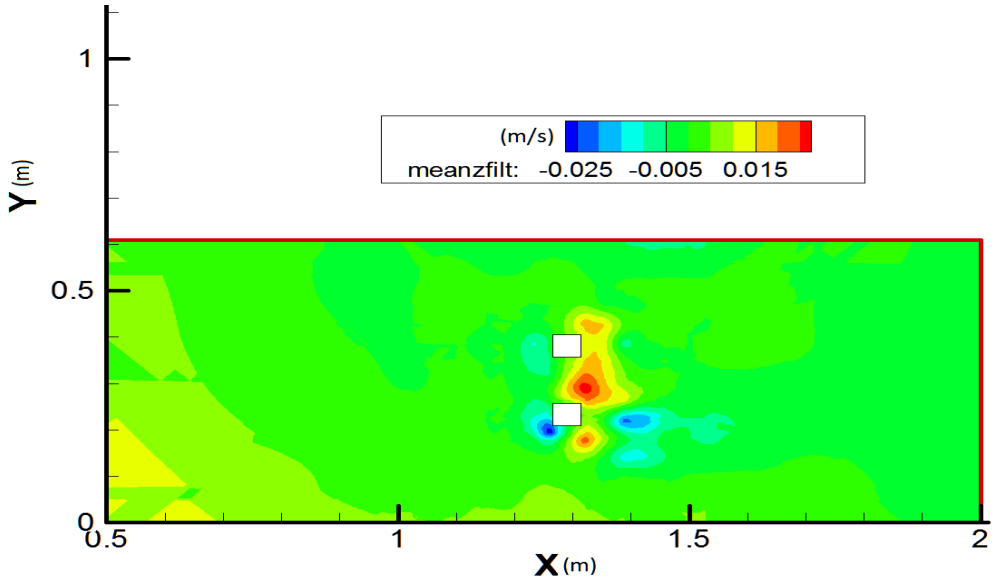

Figure 35: Small flume vertical velocity with 2 piers only

In the large flume, there was minimal vertical velocity in the approach flow but as the water hit the pier, a diving effect was created as shown in Figure 34. After the pier, a resurgence occurs that satisfied the continuity principal. The decrease in the streamwise velocity was met with an increase in magnitude of the vertical velocity. This can be explained by the fact that when the water hit the pier, it flowed downward as found by (Dey et al, 2007)

As seen in Figure 35, the small flume demonstrated a similar velocity distribution but the downflow before the pier is not as pronounced. This seems strange at first but upon further comparison with the scour patterns, as shown in Figure 46 and Figure 47, the differences in flow are related to the differences in the observed bathymetry. The difference in bathymetry was likely a scaling issue; since the grain size for the small flume was not scaled down, there was not enough shear stress in the zone of expansion to transport the sediment. Overall, for the case of two piers without a constriction, the flow fields between the small and large flume were reasonably similar.

The maximum vertical velocity found in the large flume was -0.045m/s while for the small flume it was -0.025m/s.

By examining Figure 34 and Figure 35 and comparing them with Figure 46 and Figure 47, one will note that the vertical diving velocity occurred at the location of the deepest scour.

4.2.4 Reynolds Stresses

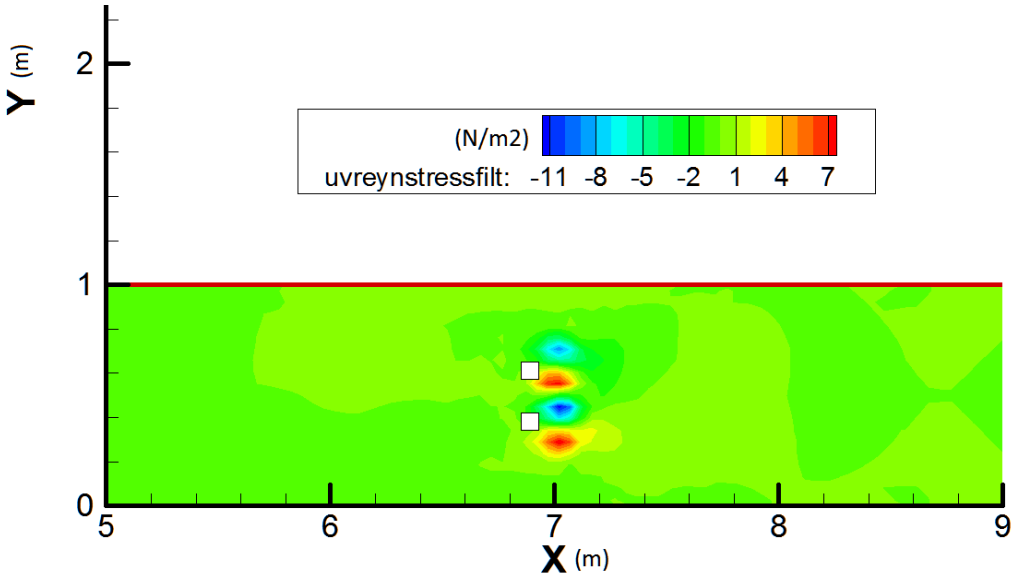

Figure 36: τ_{UV} for the large flume for the case of 2 piers alone

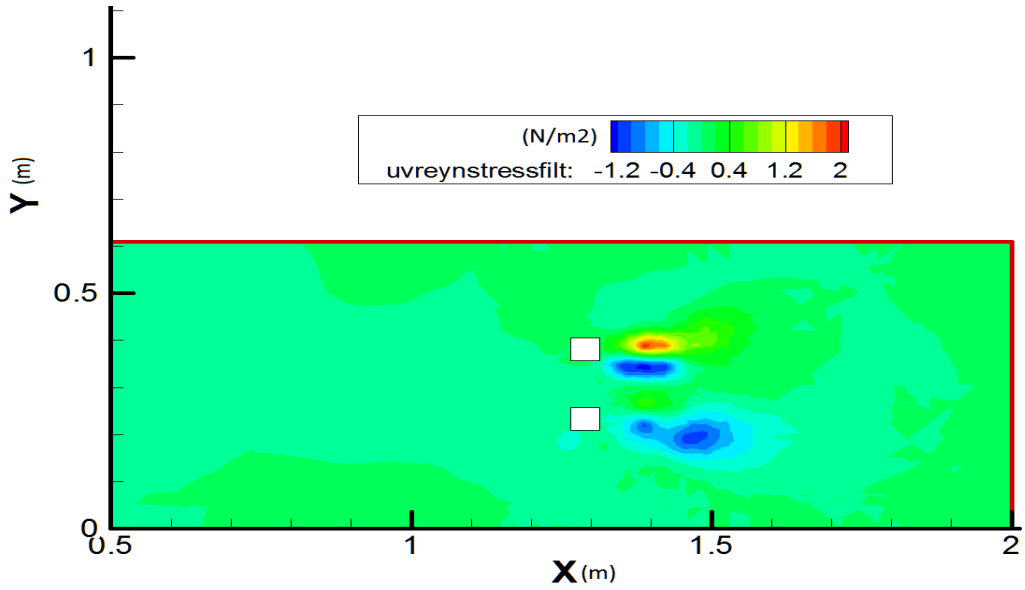

Figure 37: UV Reynolds Stress for the small flume for the case of 2 piers alone

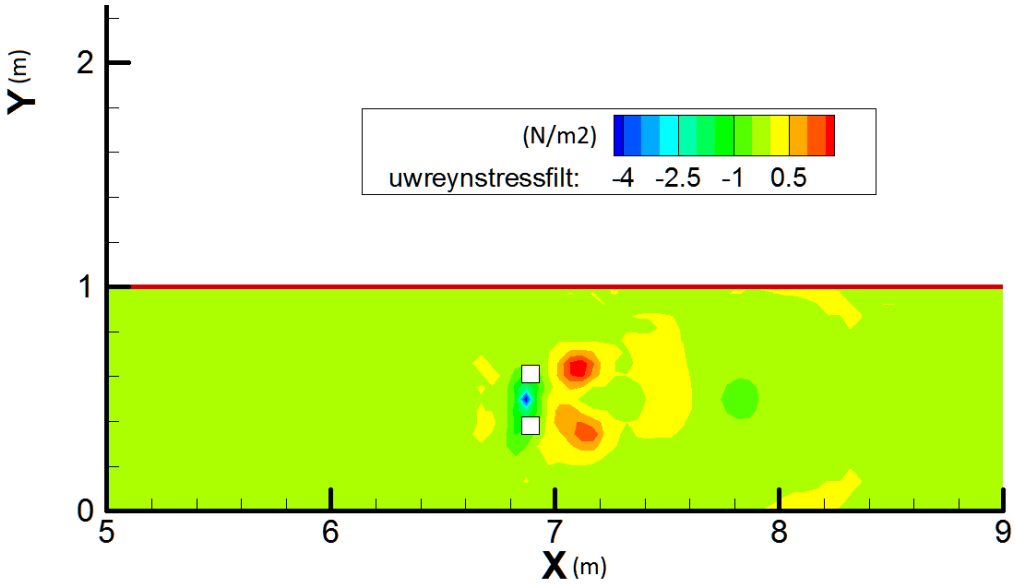

Figure 38: τ_{uw} for the large flume for the case of 2 piers alone

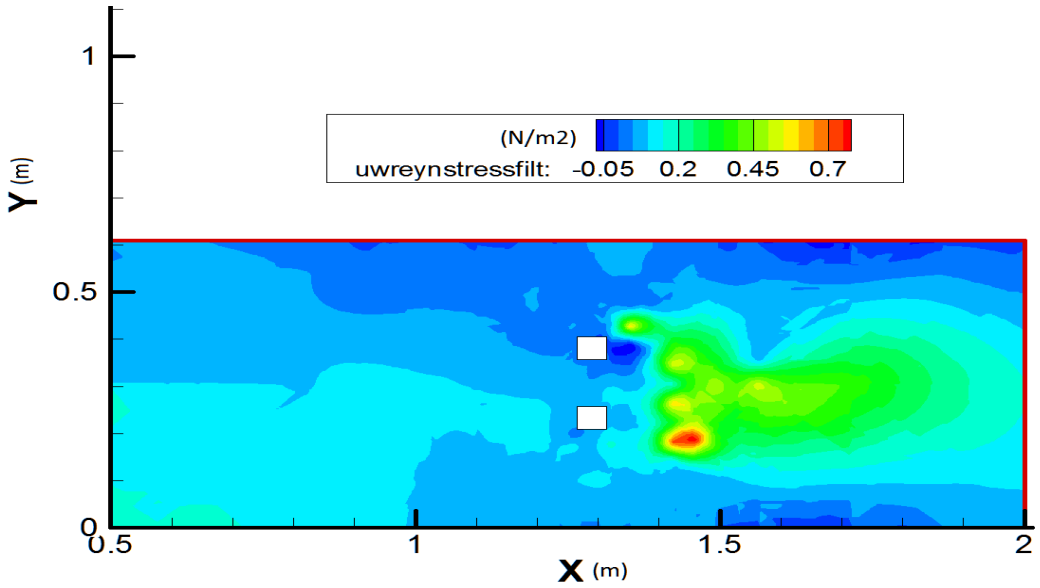

Figure 39: τ_{uw} for the small flume for the case of 2 piers alone

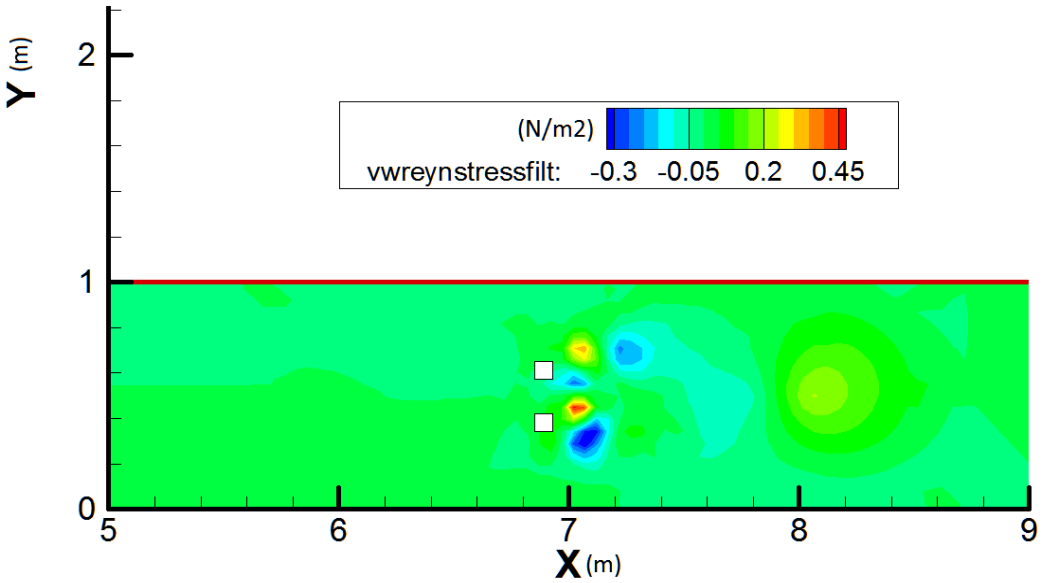

Figure 40: τ_{vw} for the large flume for the case of 2 piers alone

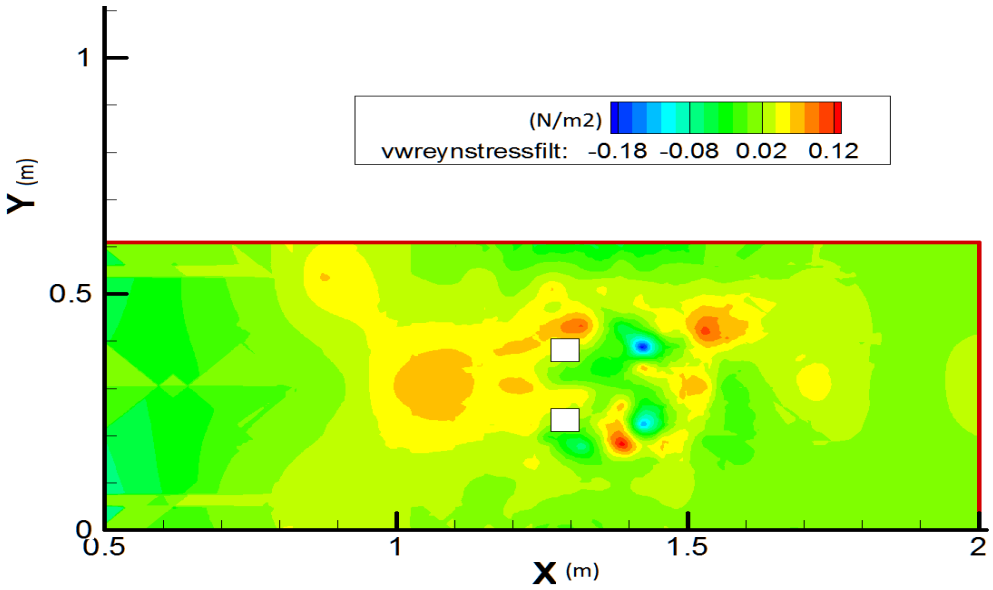

Figure 41: τ_{vw} for the small flume for the case of 2 piers alone

By viewing the Reynolds stresses distribution in Figure 36, Figure 38, and Figure 40, it appears that for the large flume, the largest magnitude of Reynolds Stress was the UV component with a maximum magnitude of -14N/m^2. The deepest scoured area occurred upstream of the piers while the maximum Reynolds stress occurred downstream in the area between the piers.

This was also true for the case of the small flume as observed in Figure 37, Figure 39, and Figure 41 with a maximum value in the UV direction of 1.8 N/m^2.

When comparing the distribution of Reynolds stresses between the large and small flumes, one will note the significant differences. The large flume results clearly showed the wake vortices but this was not the case within the small flume. This difference will be explained in the discussion section below.

4.2.5 TKE Distribution

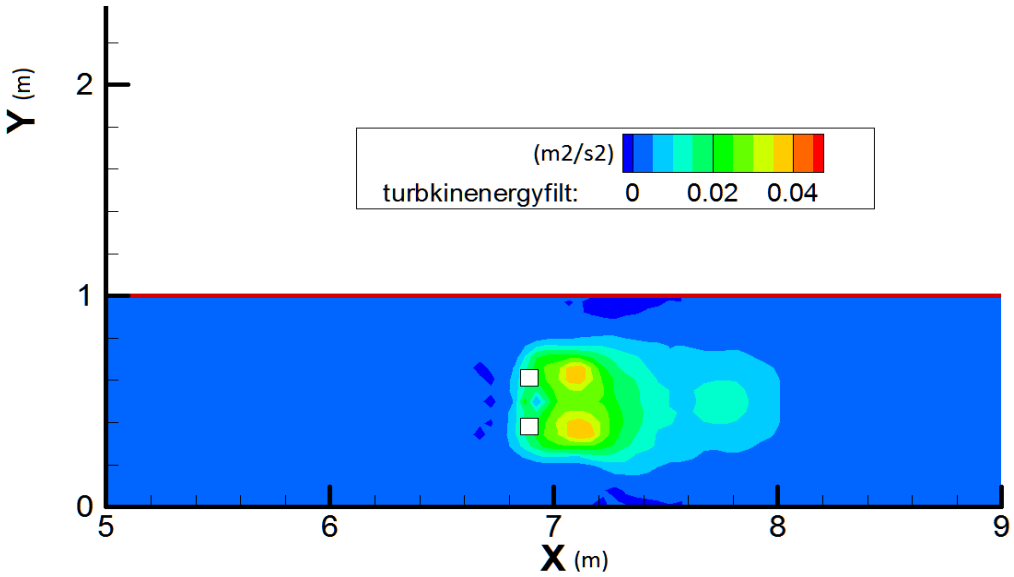

Figure 42: TKE Distribution for the large flume with 2 square piers

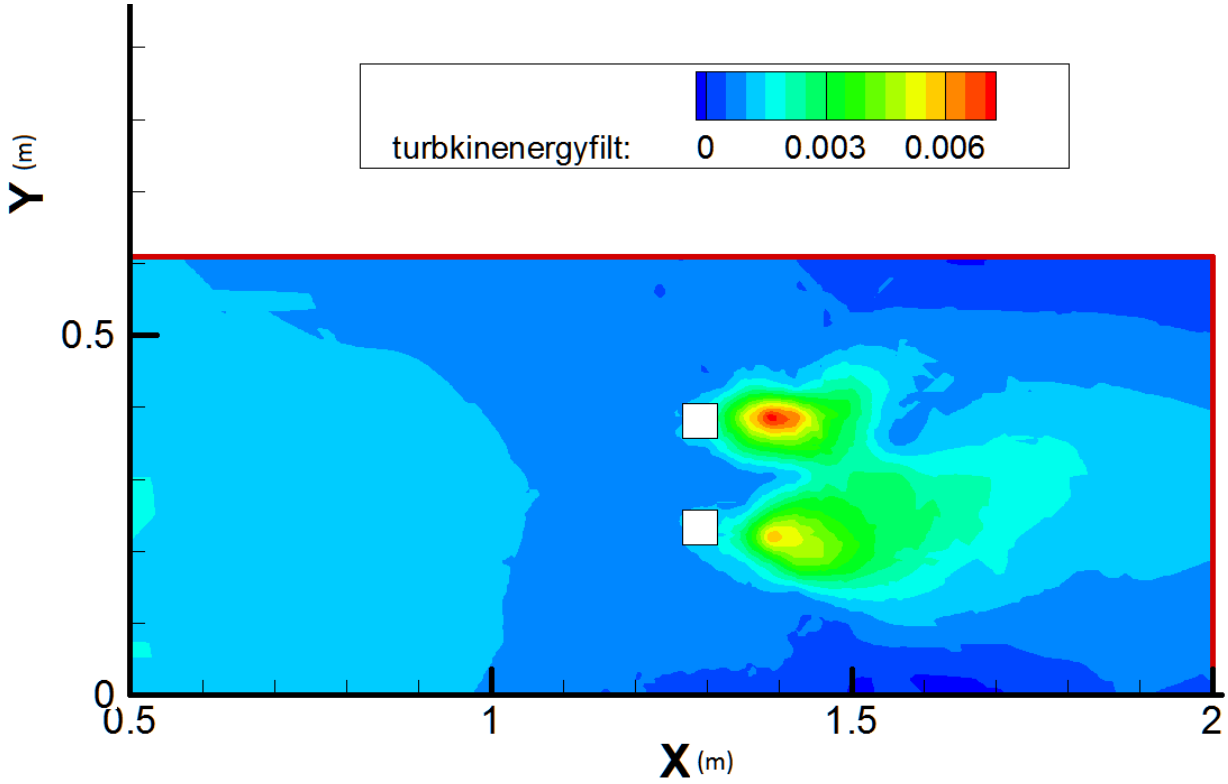

Figure 43: TKE Distribution for the small flume with 2 square piers

By examining Figure 43, TKE had a maximum value of 0.04m^2/s^2 for the large flume and 0.006 m^2/s^2 for the small flume as seen in Figure 43. For both cases, the highest values of TKE were found in the turbulent wake caused by the piers. Upstream of the piers, the TKE was fairly close to nominal values due to minimal flow disturbance, but

then increased substantially due to the wake vortex formed because of the two piers. This flow pattern was consistent in both the large and small flume.

4.2.6 Z Vorticity

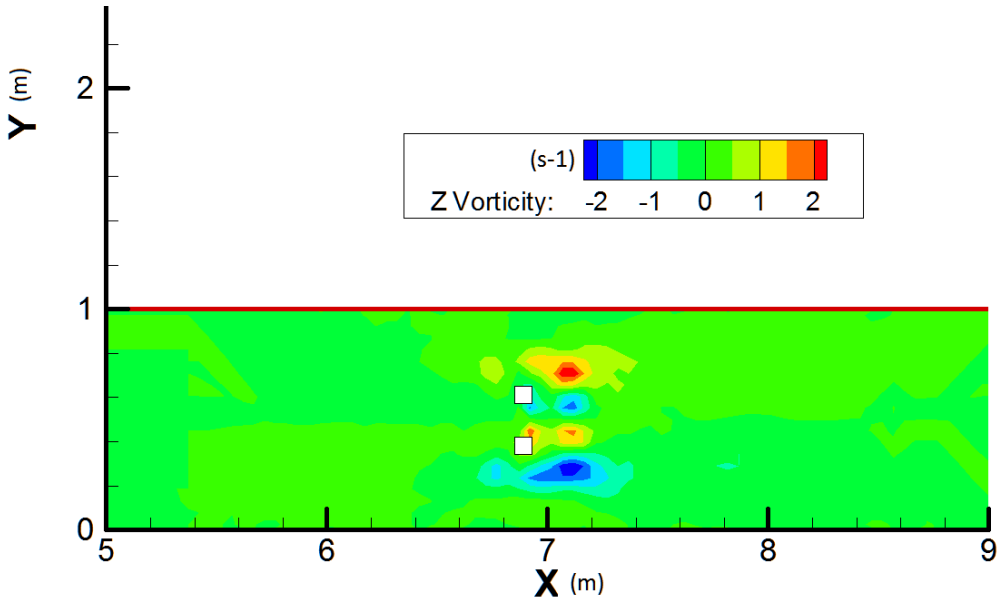

Figure 44: Z-Vorticity distribution for the large flume with 2 square piers

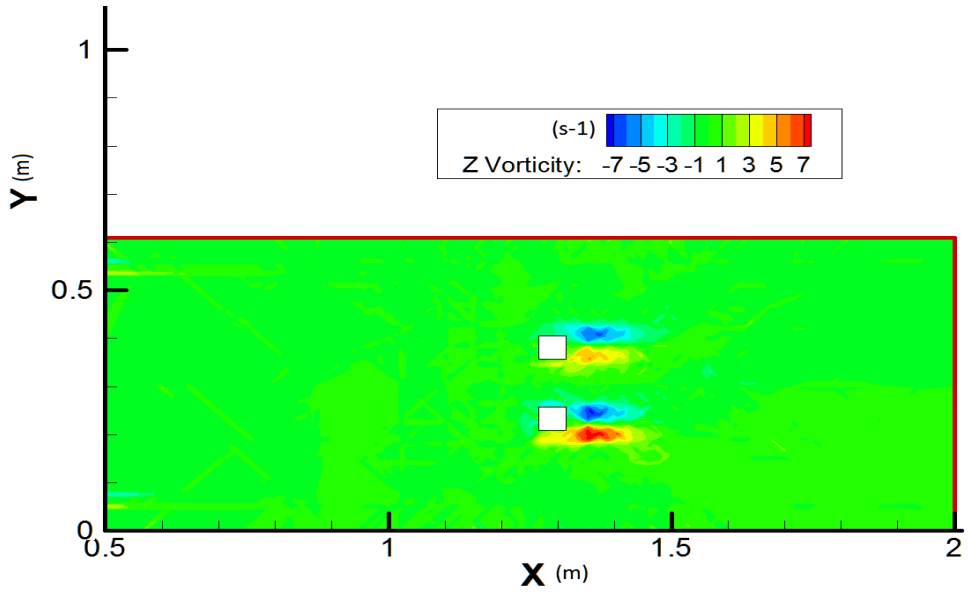

Figure 45: Z- Vorticity distribution for the large flume with 2 square piers

The vorticity in the z direction was calculated using Tecplot and is presented in Figure 44 and Figure 45respectively. For the large flume, the z vorticity had a maximum magnitude of $2s^{-1}$ while for the small flume, the maximum value is $7s^{-1}$. The non zero values of vorticity were closely correlated with the locations of high turbulence and high scour.

4.2.7 Scour Pattern

The scour distributions are plotted in the figures below. The maximum scour depth is given by the largest negative number while the maximum deposition is shown by the largest positive number.

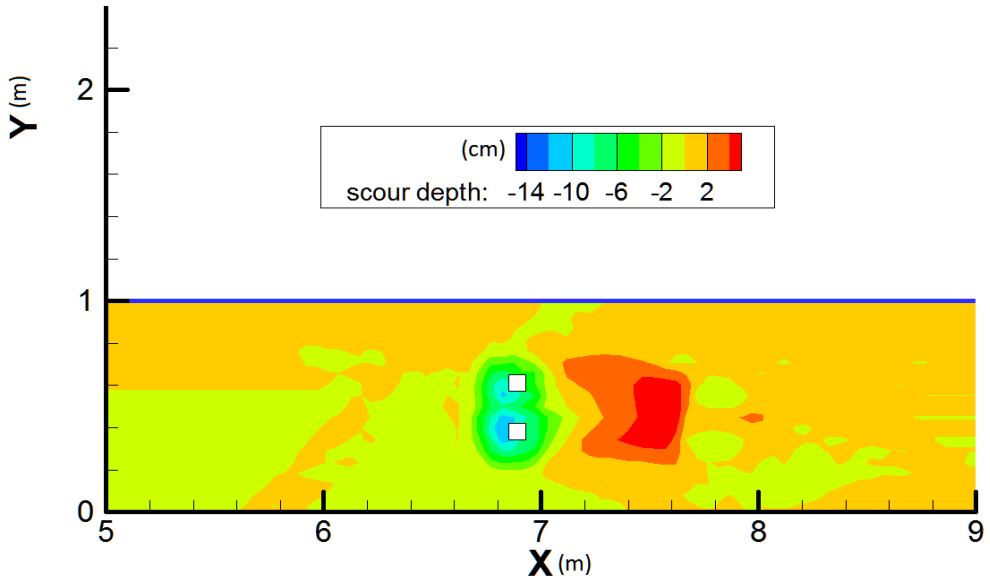

Figure 46: Scour pattern for the large flume with 2 piers only

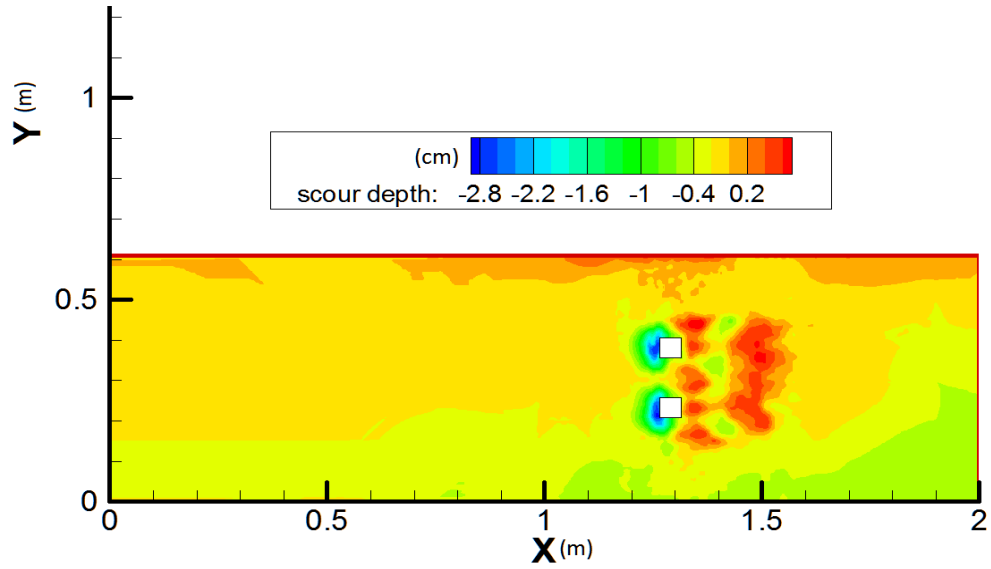

Figure 47: Scour pattern for the small flume with 2 piers only

The location of maximum scour occurred at the foot of the piers and correlated well with the location of the maximum downward velocity. Just after the pier, there was an area of deposition. This is observed in both flumes as seen in Figure 46 and Figure 47, but one difference is that the two scour holes connected for the large flume but they remain separate for the small flume. This will be explained in the discussion section below.

4.3 Constriction Only

The following section provides the velocimetry and scour results for the experiments with only the constriction.

4.3.1 Streamwise Velocity

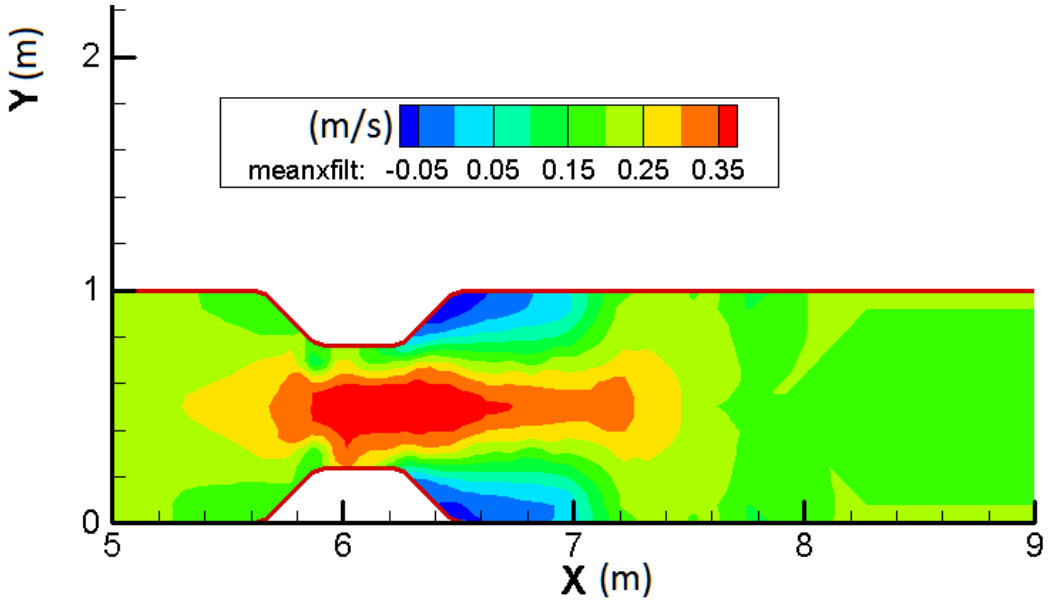

Figure 48: Streamwise velocity for the large flume in the case of a constriction alone

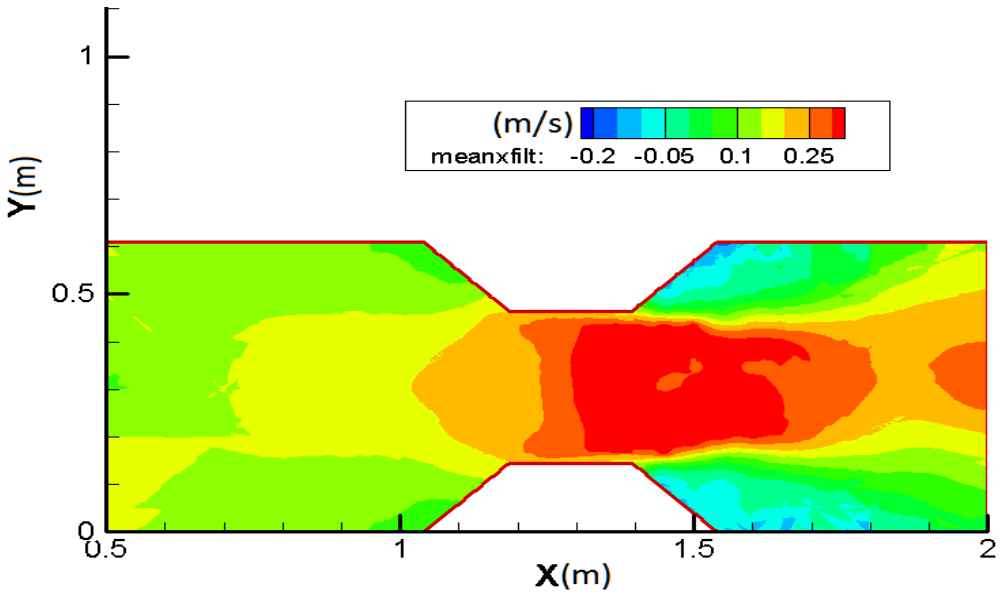

Figure 49: Streamwise velocity for the small flume in the case of a constriction alone

The streamwise velocity was constant in the approach flow and increased due to the constriction. This was due to the reduction in flow area and satisfies the continuity principle. This flow pattern was observed for both the large and small flume as seen in Figure 48 and Figure 49 with maximum velocities of 0.35m/s and 0.25m/s respectively. Note there was flow separation after the contraction in both the small and large flume. This is consistent with the flow pattern that was observed by (Duc & Rodi, 2008) and is presented in Figure 11.

4.3.2 Comparison of Velocity Profile

Thus far, the velocity fields on a plane have been shown but due to equipment limitations, these are not along the same plane. Presented below, are velocity profiles taken within the constriction for the small and large flume. These were measured at the same relative location between the flumes thus providing an opportunity for data validation.

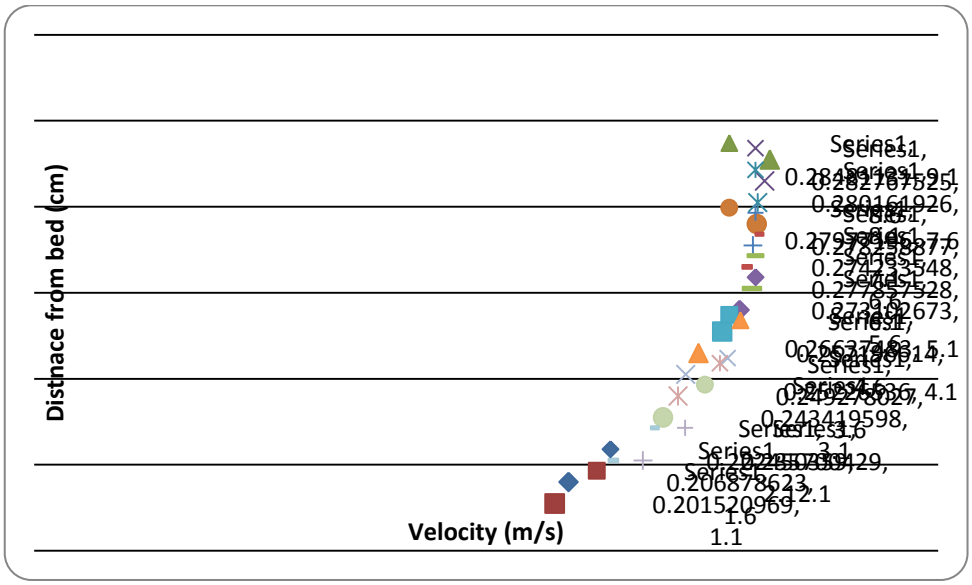

Figure 50: Velocity profile for small flume at the start of the Constriction for the constriction only case (x = 123m, y = 23.2m)

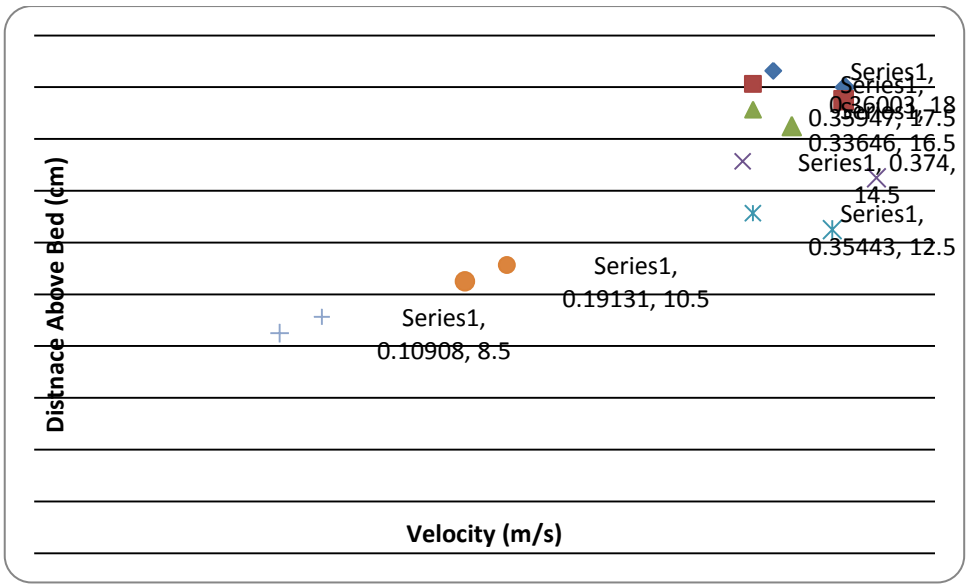

Figure 51: Velocity profile for large flume at the start of the Constriction for the constriction only case (x = 5.93m, y = 0.31m)

The velocity profiles for the constriction only case at a position that is close to the start of the fully constricted area are shown in Figure 50 and Figure 51. A similar distribution of velocity was observed in the large and small flumes, in that the velocity was highest towards the surface and lower at the bed. Since both flumes show a similar distribution, it gives credibility to the velocity measurements.

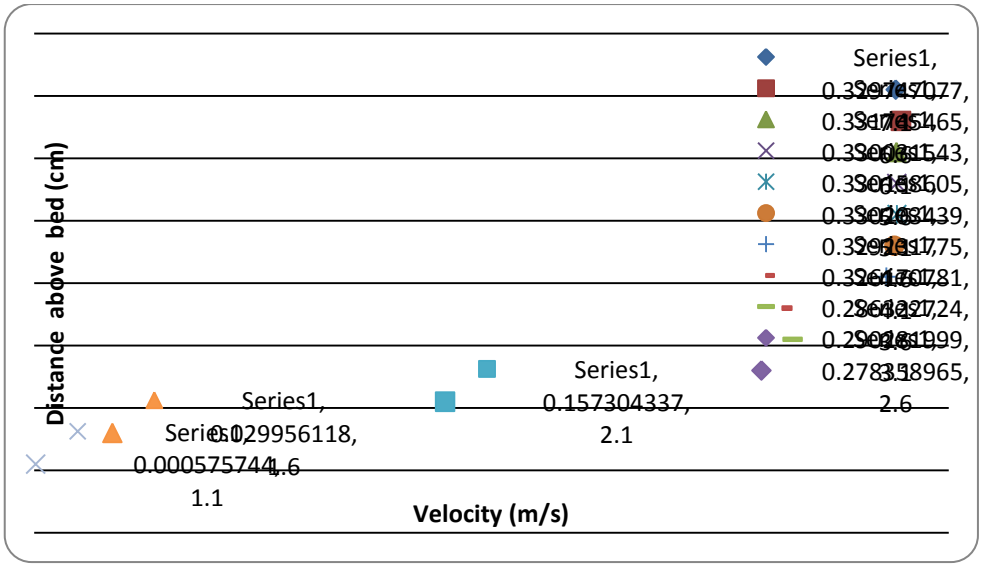

Figure 52: Velocity profile small- constriction only: end of constriction (X = 129cm, Y = 31.7cm)

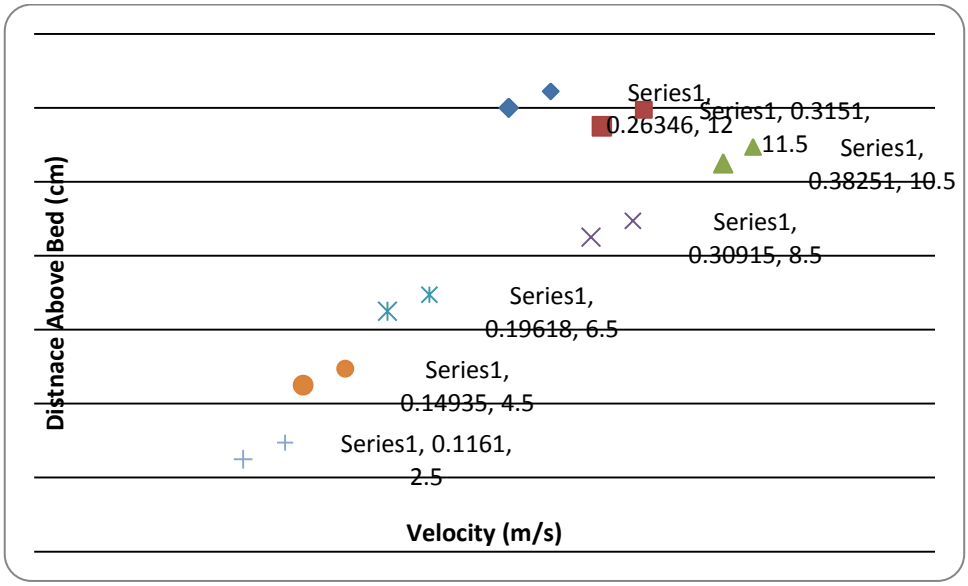

Figure 53: Velocity profile for large flume- constriction only: End of constriction (X = 6.2m, Y = 0.27m)

Figure 52 and Figure 53 show the velocity profile at the end of the constriction. Both velocity profiles show a general trend where the velocity was higher at the top and increases with depth as expected. With the large flume, the velocity seems to decrease in velocity at the surface.

4.3.3 Cross Stream Velocity

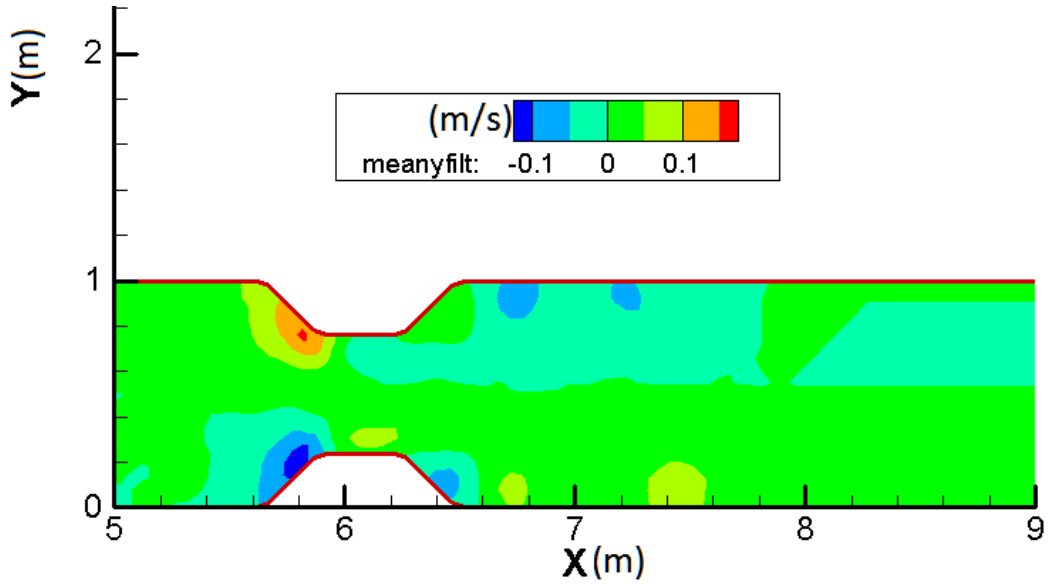

Figure 54: Cross stream velocity for the large flume for the case of the constriction alone

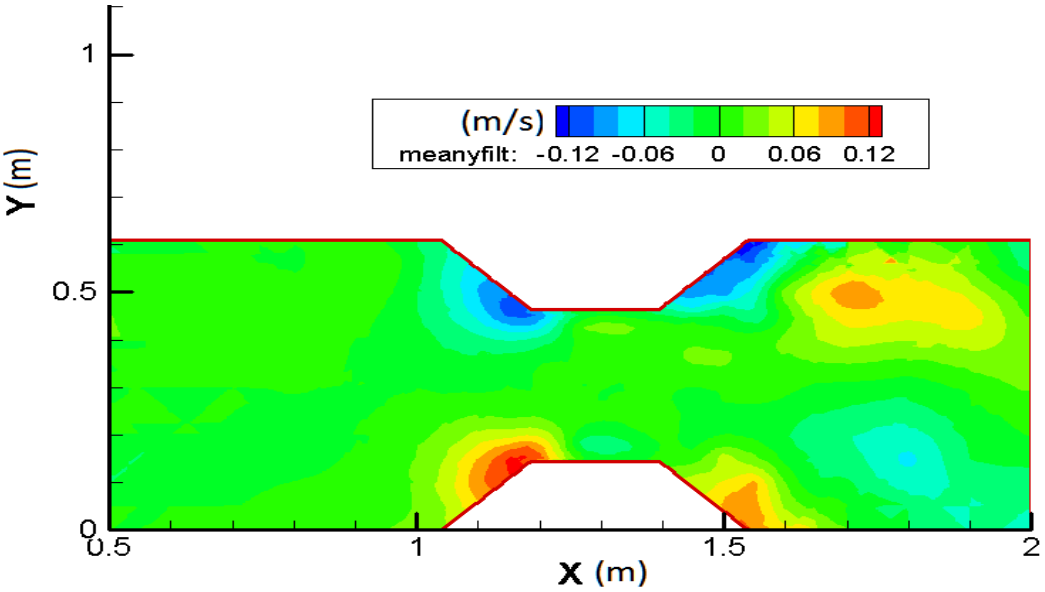

Figure 55: Cross stream velocity for the small flume for the constriction alone

As seen in Figure 54, when the water approached the constriction, it is forced to flow into the constricted area. This is shown by the non-zero values of cross stream velocity

at the constriction areas. In the small flume in Figure 55, this is true although the cross stream velocities created in the expansion were more pronounced. The maximum magnitudes of these cross stream velocities are 0.1m/s and 0.12m/s for the large and small flumes respectively.

4.3.4 Vertical Velocity

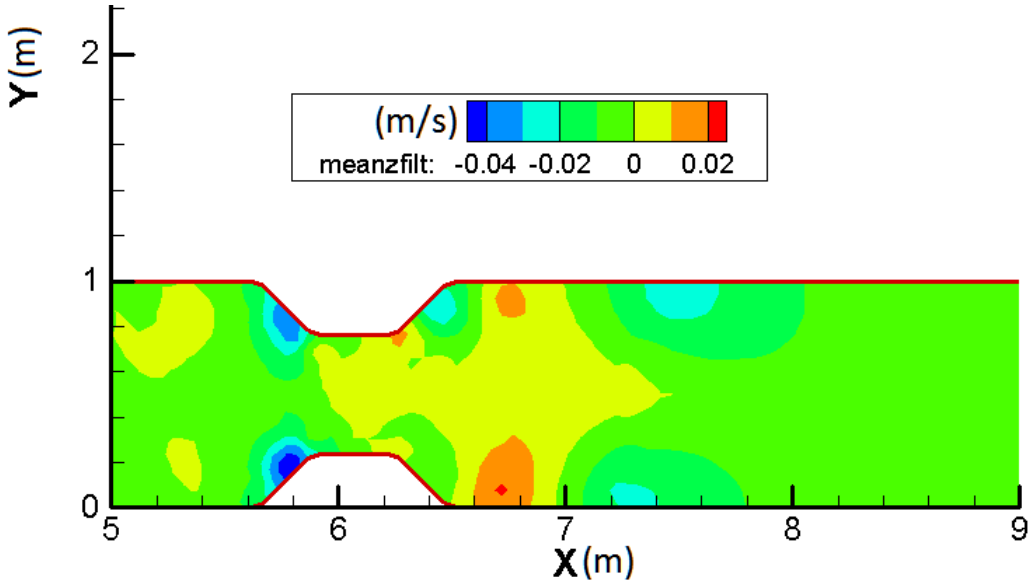

Figure 56: Vertical velocity for the large flume for the case of the constriction alone

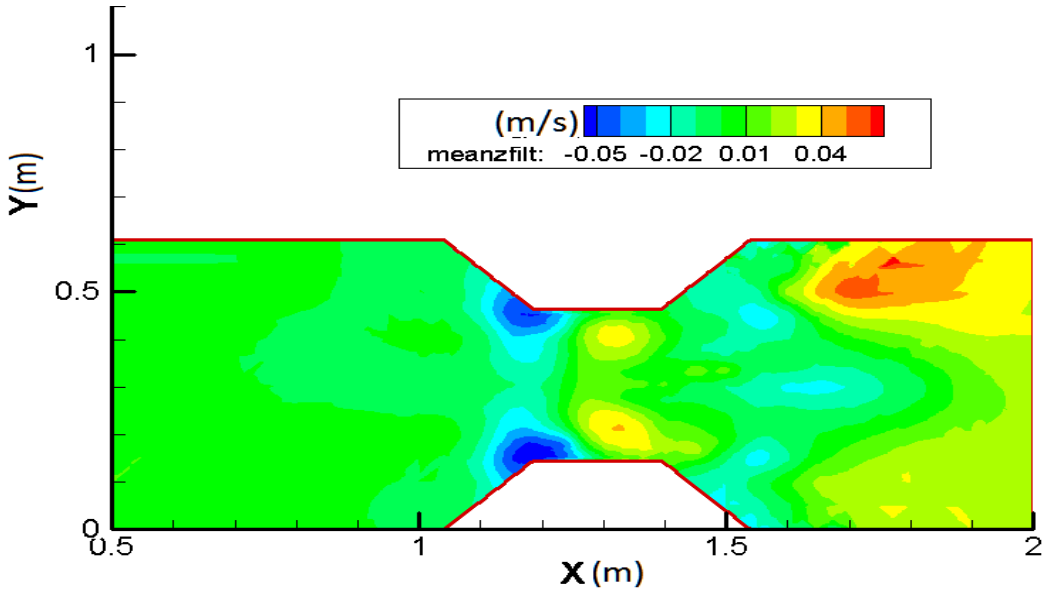

Figure 57: Vertical Velocity for the small flume for the case of the constriction alone

When the water flowed into the sides of the constriction on the large flume, it plunged downward as seen in Figure 56. After the constriction, an upward flow is observed. Once again, this location of downward flow was where the areas of high scour are found. Looking at Figure 57, it is observed that the small flume produced a similar flow pattern. However, one difference is that there exists a downward velocity in the middle of the expansion zone in the small flume. Comparing this to the bathymetry section shown in Figure 68 does not readily explain this. A possible explanation is presented in the discussion below.

The maximum downward flows for the large and small flumes were 0.04m/s and 0.05m/s respectively. It is interesting to note that the small flume actually had a larger downflow as compared to the large flume yet the large flume had more scour. This indicates that is it not only the magnitude of the vertical velocity that governs the scour depth.

4.3.5 Reynolds Stress

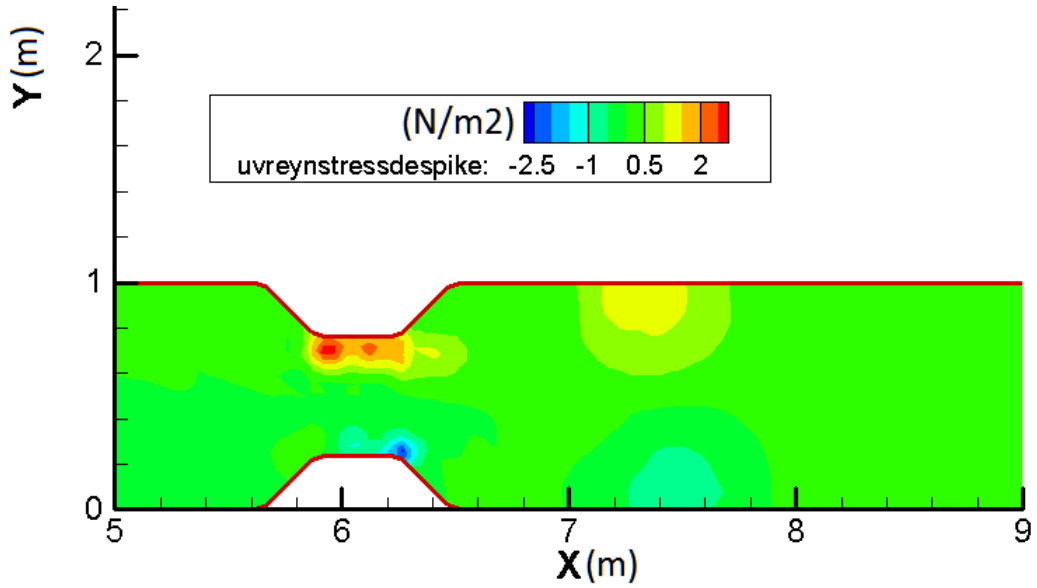

Figure 58: τ_{UV} for the large flume for the case of the constriction alone

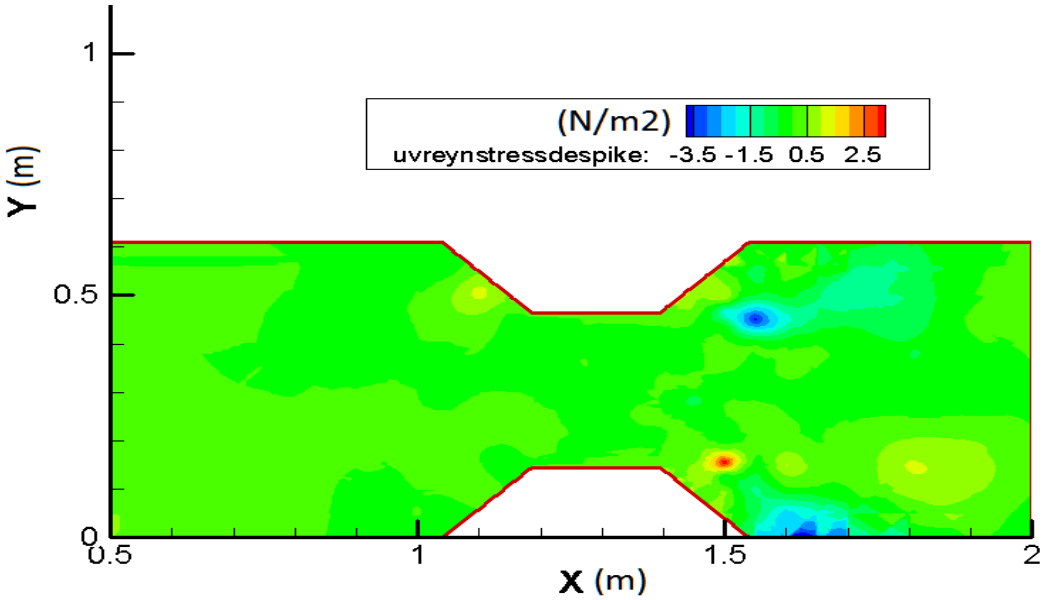

Figure 59: τ_{UV} for the small flume for the case of the constriction alone

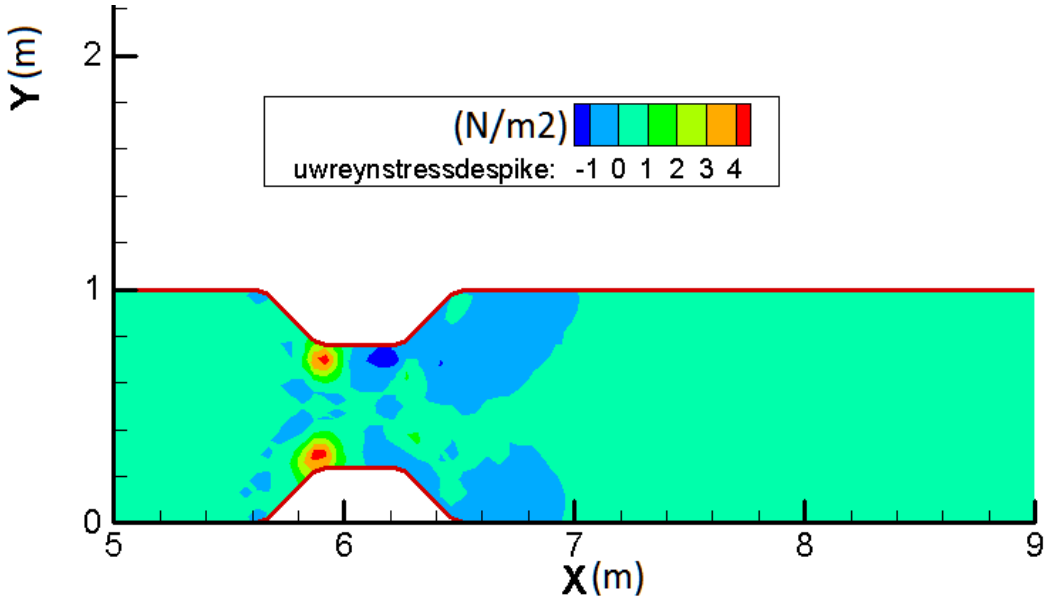

Figure 60: τ_{UW} for the large flume for the case of the constriction alone

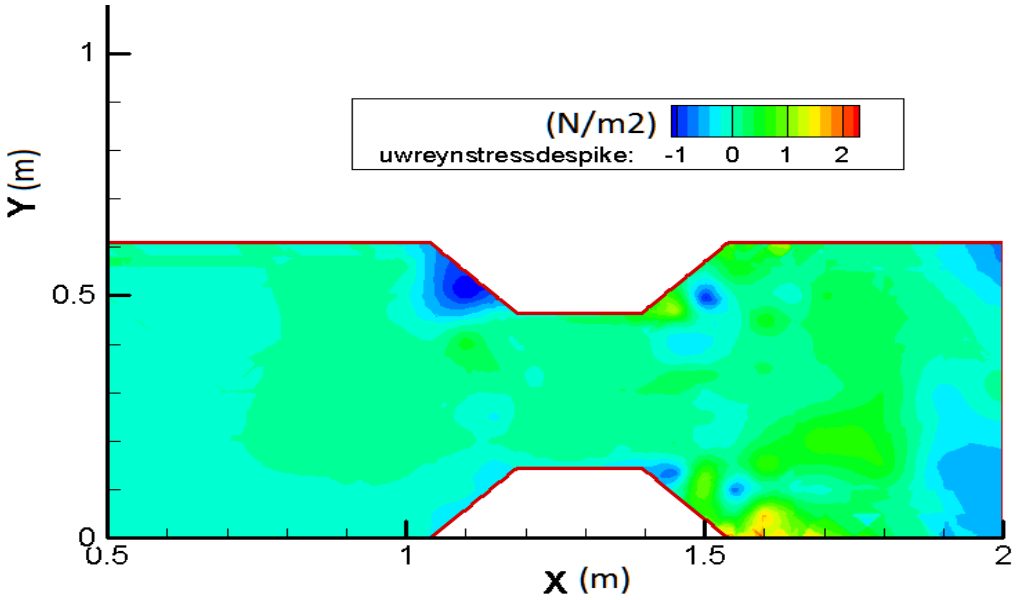

Figure 61: τ_{UW} for the small flume for the case of the constriction alone

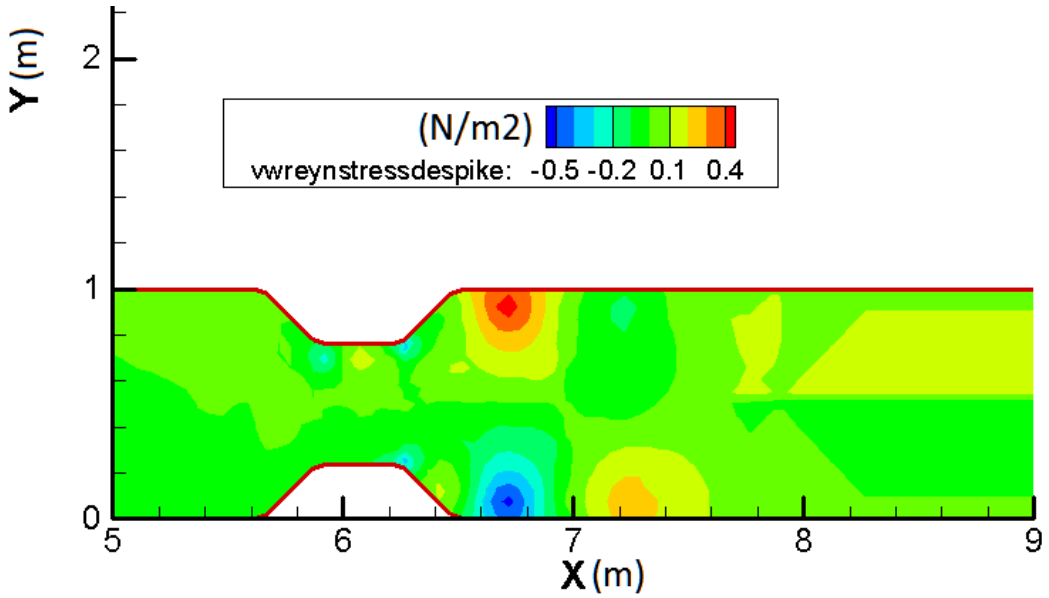

Figure 62: τ_{vw} for the large flume for the case of the constriction alone

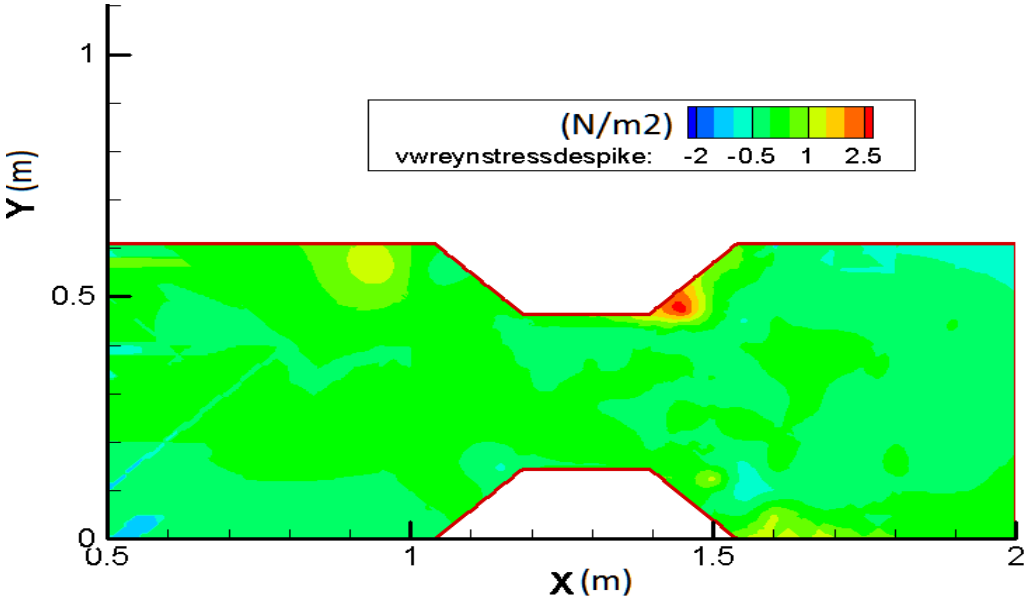

Figure 63: τ_{vw} for the small flume for the case of the Constriction alone

By examining the Reynolds Stress distributions of the large flume as displayed in Figure 58, Figure 60 and Figure 62, one can see that the largest magnitude of Reynolds stress occurred in the UV component similarly to the case with the only two piers. This correlated well with the location of maximum scour as seen in Figure 68.

Looking at the results of the Reynolds stress in the small flume in Figure 59, Figure 61 and Figure 63, it appears that the highest magnitude was in the UV direction as well and occurred downstream of the constriction. The Reynolds Stress distributions found in the large flume were closer to the expected results. When interpreting these results, one should consider the fact that the velocimetry was performed on different planes between the two flumes. As seen in Table 1, the large flume measurements were performed at 48% of the relative depth while the small flume measurements were performed at 26% of the relative depth. It is expected that the Reynolds stress distribution vary with depth so part of the differences between the large and small flume could be explained by the fact that the measurement plane is different.

4.3.6 TKE Distribution

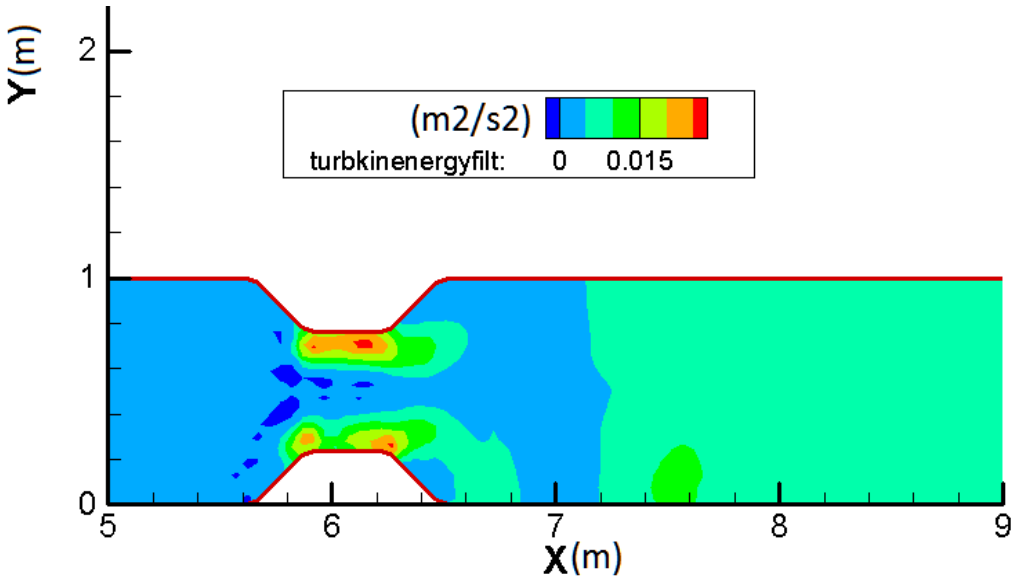

Figure 64: TKE distribution for the large flume with the constriction only

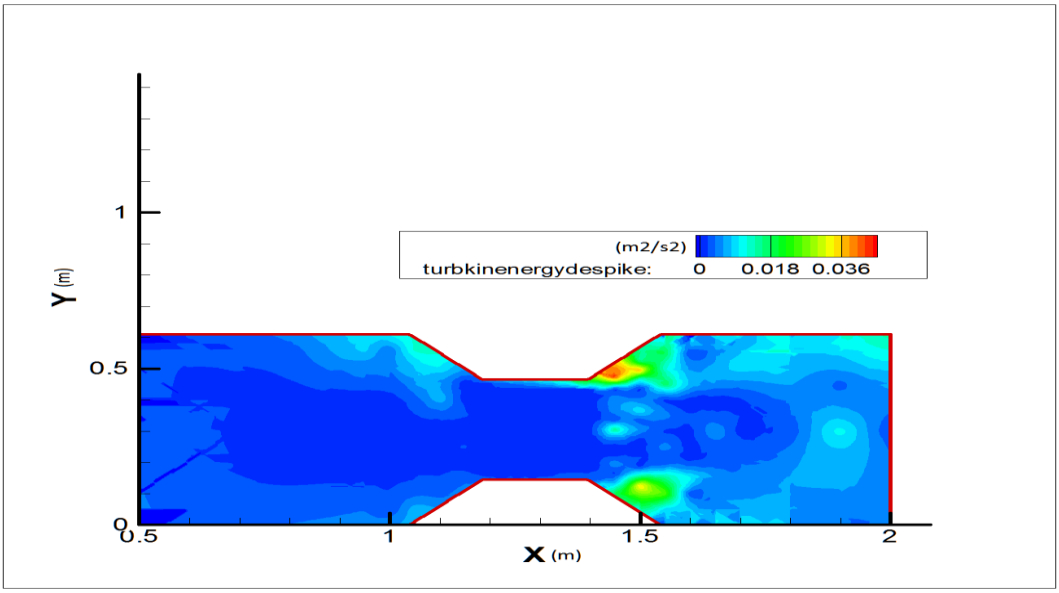

Figure 65: TKE distribution for the small flume with the constriction only

The TKE distributions for the large and small flumes were plotted in Figure 64 and Figure 65. For both the large and small flume, the maximum values of TKE occurred at the constriction but they were much more pronounced for the case of the large flume. For the case of the small flume, TKE remained close to nominal values except for at the expansion of the flume. The lower values of TKE in the small flume correlated with the lower amount of scour generated.

4.3.7 Z Vorticity Distribution

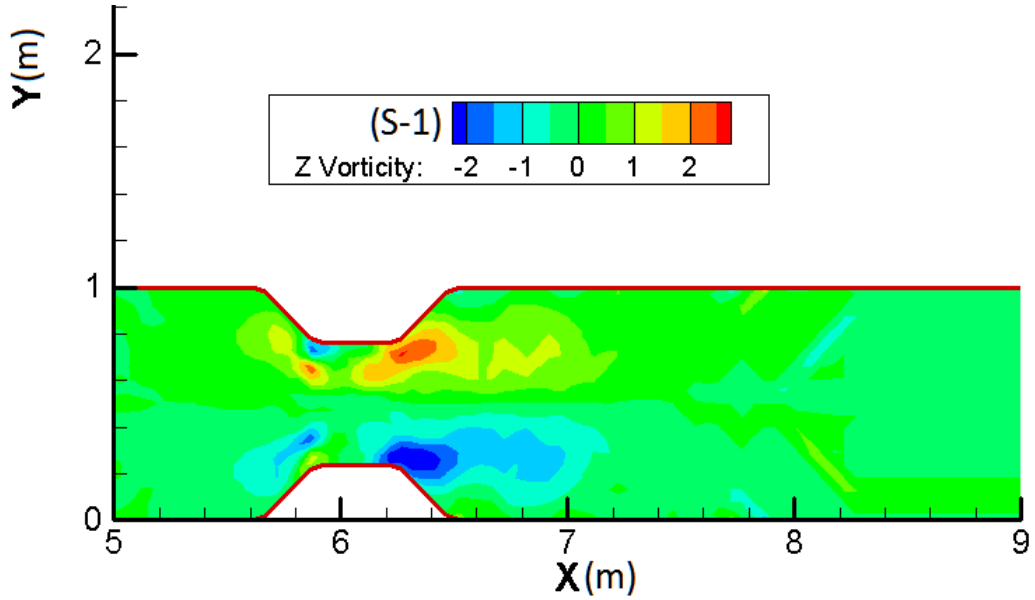

Figure 66: Z Vorticity distribution for the large flume with constriction only

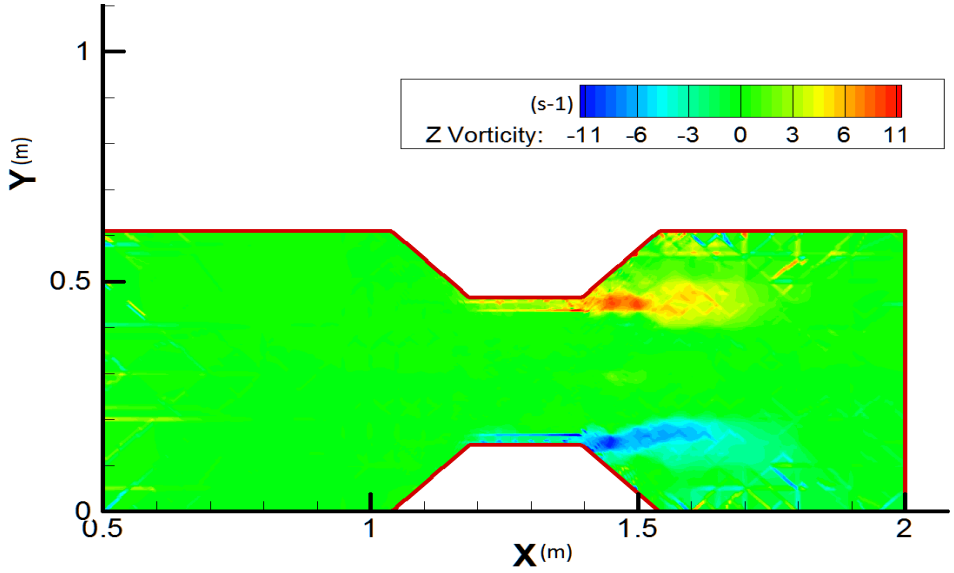

Figure 67: Z Vorticity distribution for the small flume with constriction only

The Z Vorticity distributions for the large and small flume for the case with the constriction only are shown in Figure 66 and Figure 67 respectively. For the large

flume, it was found that the distribution of Z vorticity was similar to the distribution of TKE as shown in Figure 64. The maximum value was $2s^{-1}$ in both the positive and negative direction. For the case of the small flume, it was found that the Z vorticity highest at the expansion from the constrictions showing the rotation of the water about the vertical axis.

4.3.8 Scour Pattern

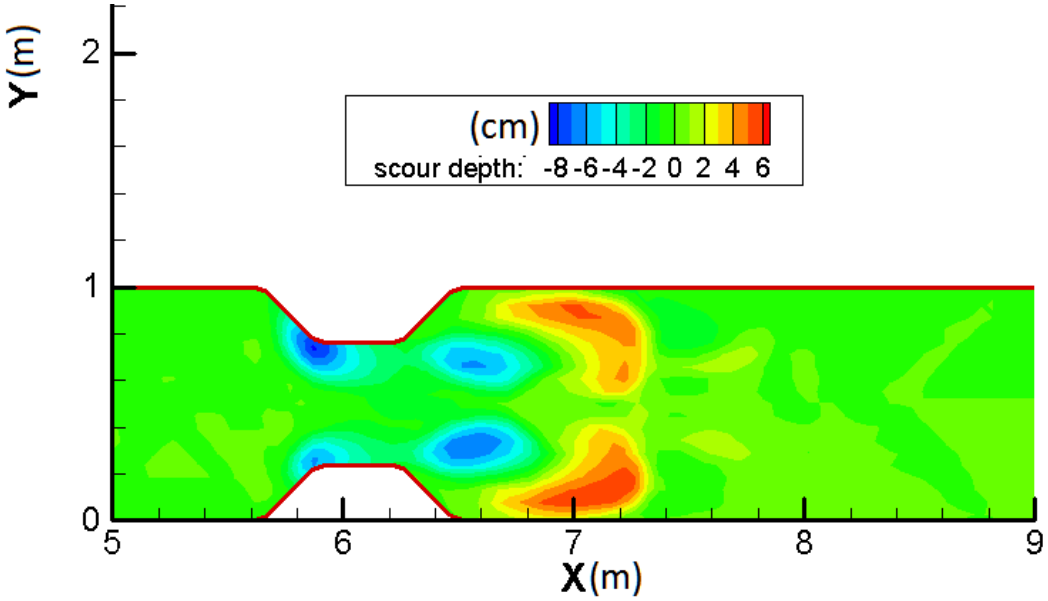

Figure 68: Scour distribution for the large flume for the case of the constriction alone

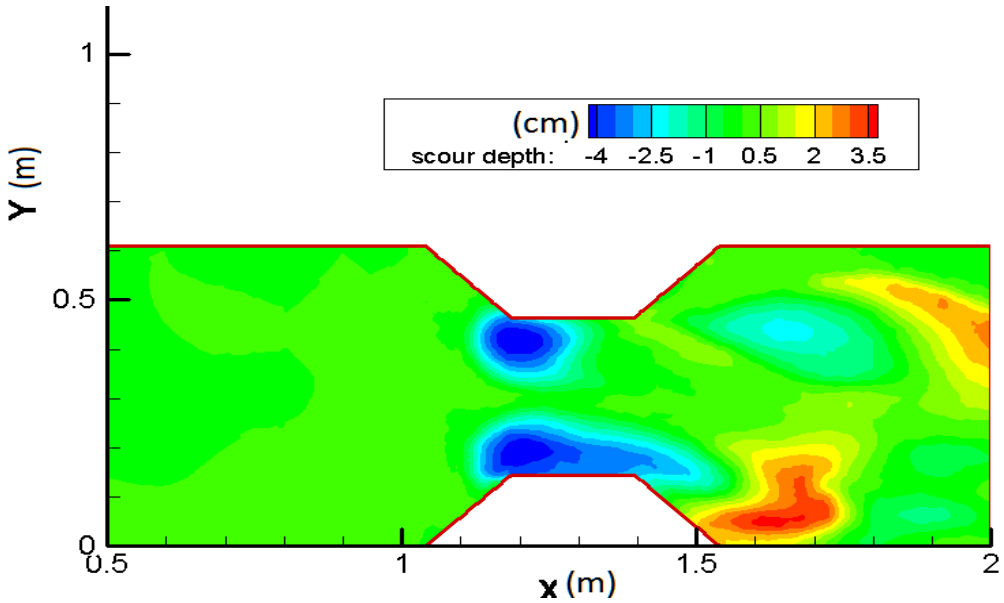

Figure 69: Scour distribution for the small flume for the case of the constriction alone

The scour pattern for the large flume is shown in Figure 68 while for the small flume, it is shown in Figure 69. Both flumes exhibit the maximum scour at the constriction which correlated well with the location of maximum downward velocity. In addition, both flumes showed deposition after the constriction which was reasonable because as the water velocity decreased after the expansion, it did not have the energy to transport the sediment. One difference between the scour distribution in the large and small flume is that in the small flume, the sediment distribution was asymmetric.

It is interesting to note that the scour pattern observed in the large flume as shown in Figure 68 shows scour at the beginning of the narrowest part of the flume and also at the end forming effectively four scour holes. However, for the small flume major symmetric scour holes occurred only at the start of the constriction as seen in Figure 69. The scour distribution for the large flume correlated well with both the Z vorticity and the TKE distributions shown in Figure 66 and Figure 64 and respectively.

4.4 Piers and Constriction Combined

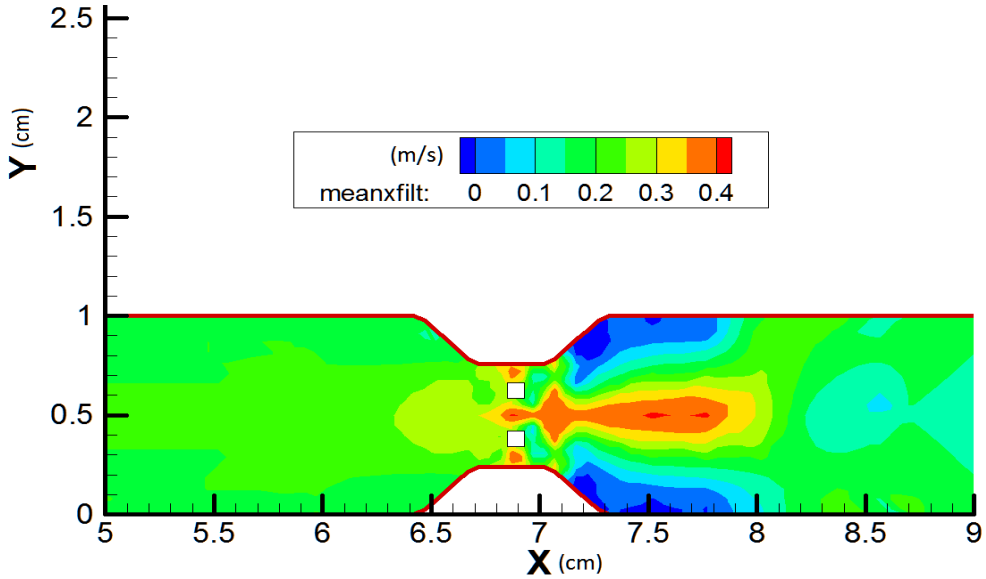

Figure 70: Streamwise velocity for the large flume in the case of two square piers and the constriction

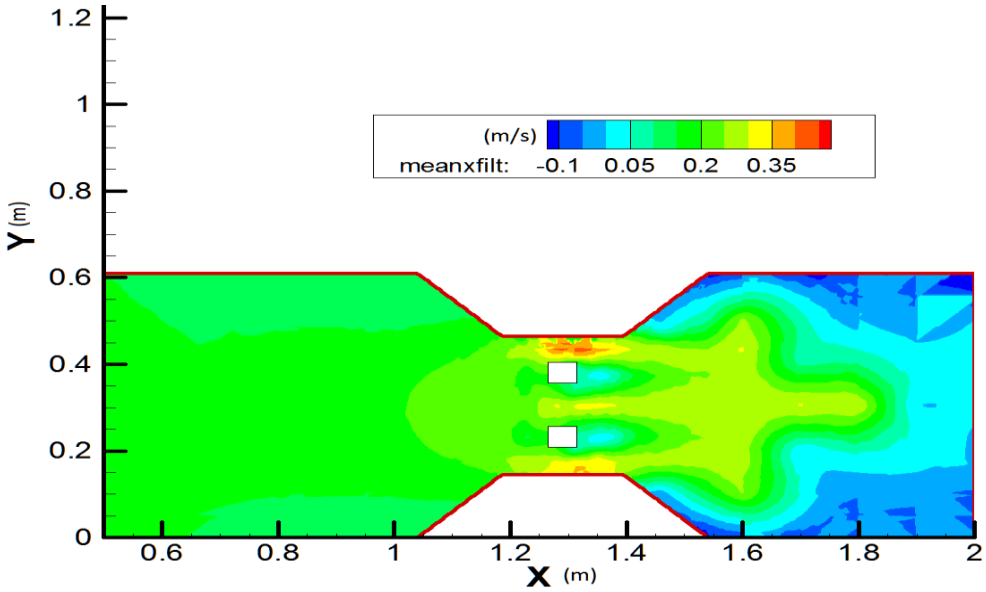

Figure 71: Streamwise velocity for the small flume in the case of two square piers and the constriction

For the case of having both the constriction and the two piers together at the same time, the streamwise velocity is shown in Figure 70 for the large flume and Figure 71 for the small flume. The maximum streamwise velocities for the large and small flumes were 0.4m/s and 0.28m/s respectively. In comparing the streamwise velocity

distributions between the large and small flumes, one notes a similar flow field in which flow accelerated between piers the constriction and then slowed down after the area of the constriction and piers.

Another observation is that the presence of the piers has minimized the recirculation zone in the flow expansion. The strength of the recirculation zone is defined by the cross stream velocity and when comparing the cross stream velocity for a constriction with and without the piers as shown in Figure 54 and Figure 76 respectively, one notes that the recirculation was weaker due to the piers.

Originally, the ADV data for the large flume was wrapped because the ambiguity velocity setting was exceeded. However, an unwrapping procedure was developed to recover the data. This was successful for the streamwise velocity but less so for the cross stream and vertical components which are not presented.

4.4.1 Comparison of Velocity Profiles

The following figures show the plots of velocity profiles at the 2 positions for the large and small flume. These positions are directly in front of the pier and in between the two piers. The exact coordinates can be found in the title of the graphs.

Velocity Profiles directly in Front of the Pier.

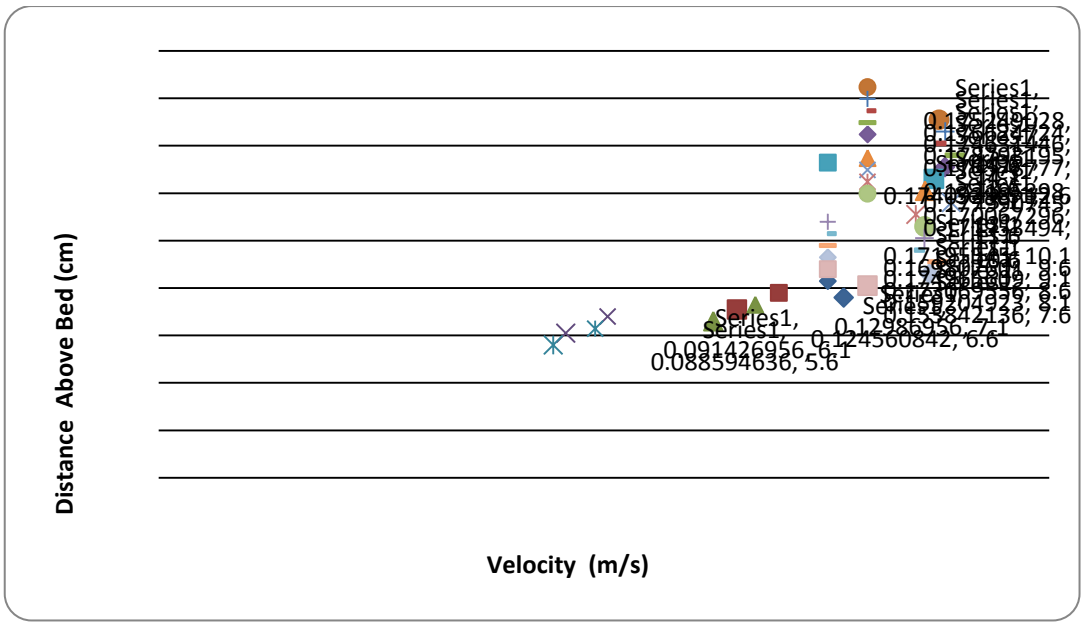

Figure 72: Velocity Profile: Small C32- Right before pier (X = 123cm, Y =23.2cm)

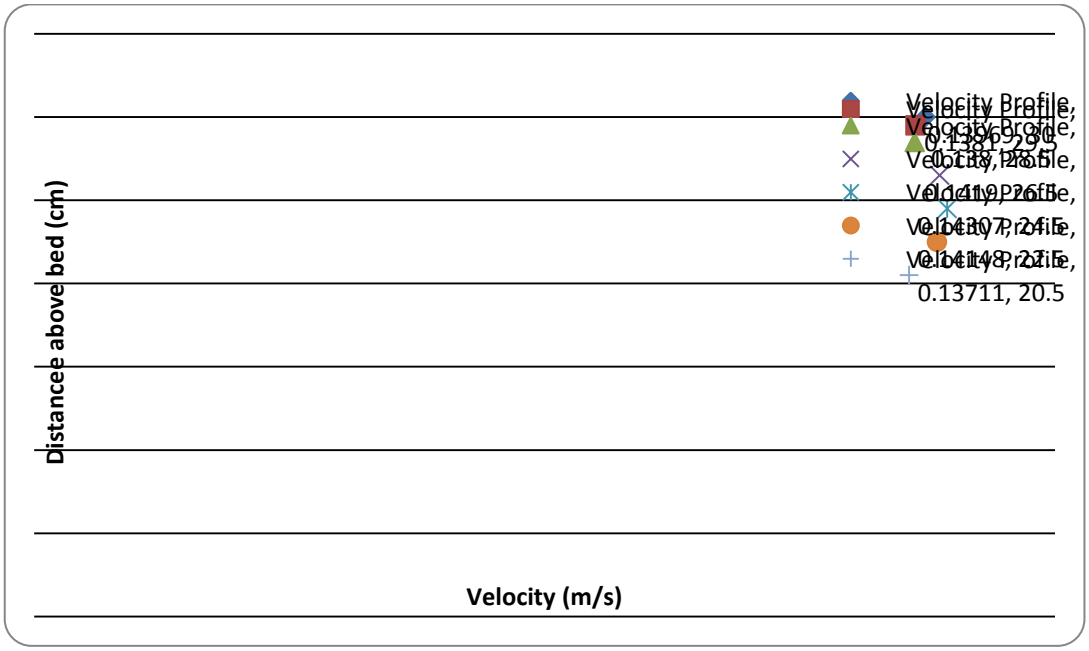

Figure 73 Velocity Profile Large C32- Right before pier (X = 679cm, Y = 62cm)

Figure 72 and Figure 73 show the velocity profile for the large and small flumes in the case of simultaneous pier and constriction scour measured directly in front of the pier. The small flume results show low velocity at the bottom with a higher velocity at the top

of the flume. For the large flume, there is high velocity close to the free surface but it is difficult to make a general conclusion because of the limited data collected. In this experiment, the slope of the deep scour made it impossible to collect velocimetry data at the bed.

4.4.2 Velocity Profiles in Between Piers

The next two figures show the velocity profiles in between the two square piers for both the small and large flume.

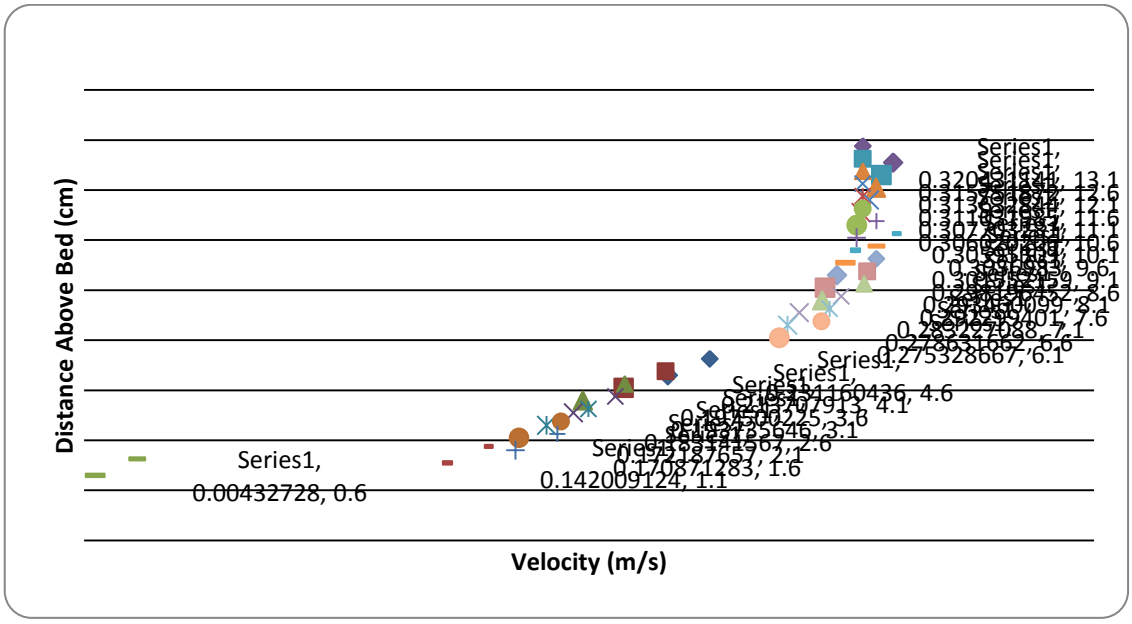

Figure 74 Velocity Profile In between piers (X = 129cm, Y = 31.7cm)

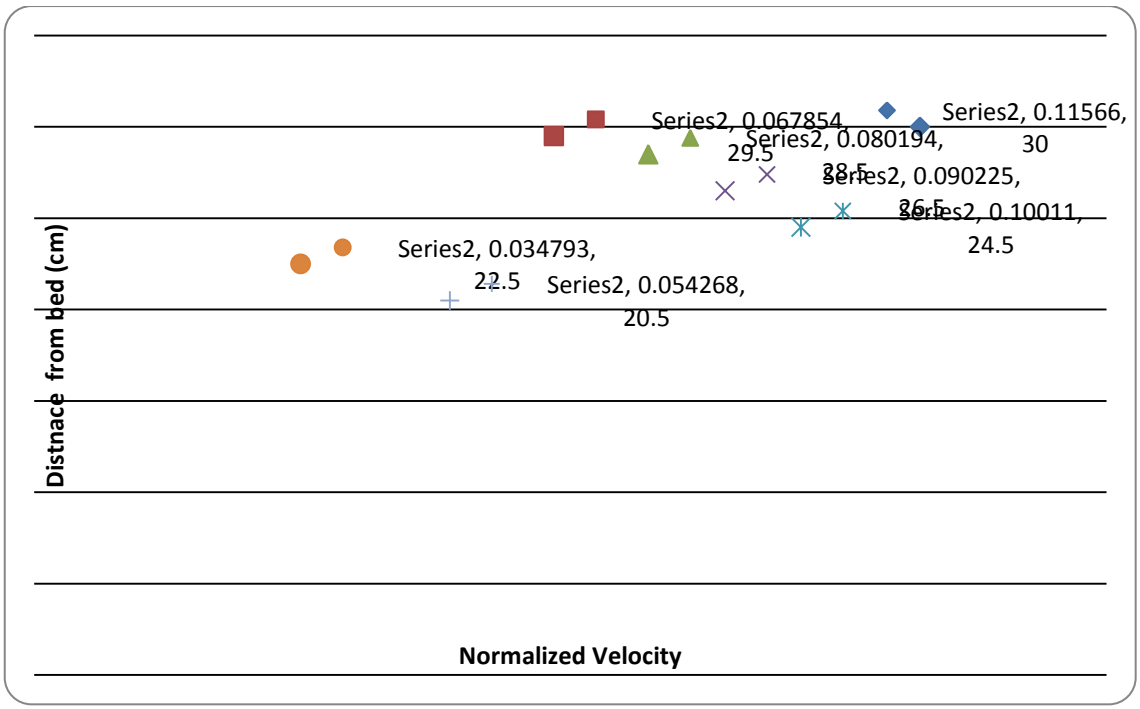

Figure 75: Velocity Profile In between piers for the large flume (C32) (X = 687cm, Y = 45.5cm)

Figure 74 and Figure 75 show velocity profiles taken in between piers for the case with both the constriction and two square piers. The small flume shows a fairly typical velocity distribution with lower velocity at the bottom due to the no slip condition at the bottom and a greater velocity closer to the free surface. The large flume profile provides the same general trend but deviates away from a typical velocity profile. This could be due to the high level of turbulence caused by constriction and piers.

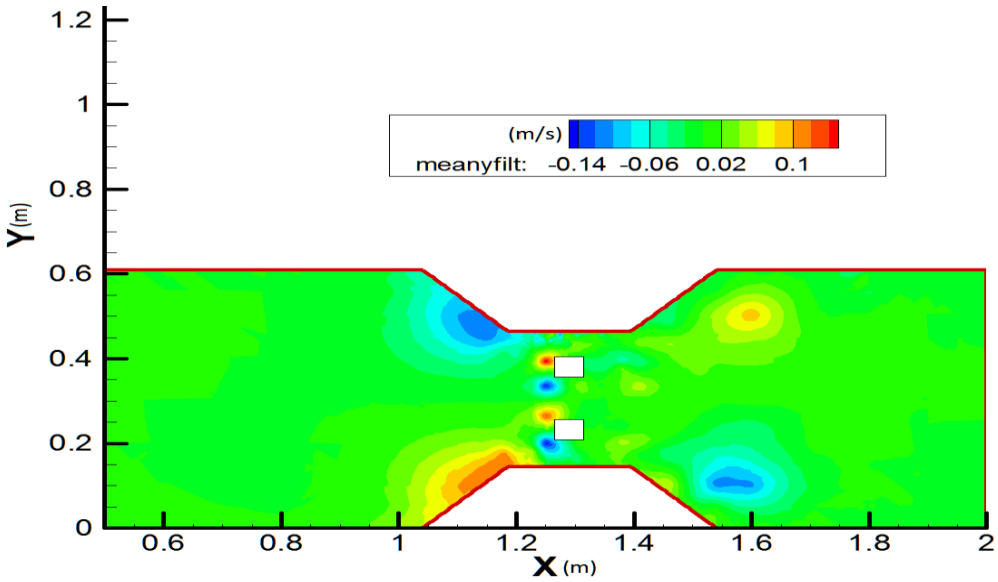

Figure 76: Cross stream velocity for the small flume in the case of two square piers and the constriction

The cross stream data are not available for the large flume due to phrase wrapping but is shown in Figure 76 for the small flume. Examination of the flow field showed convergence at the constriction and then divergence around the piers. The maximum magnitude for the cross stream velocity is 0.1m/s.

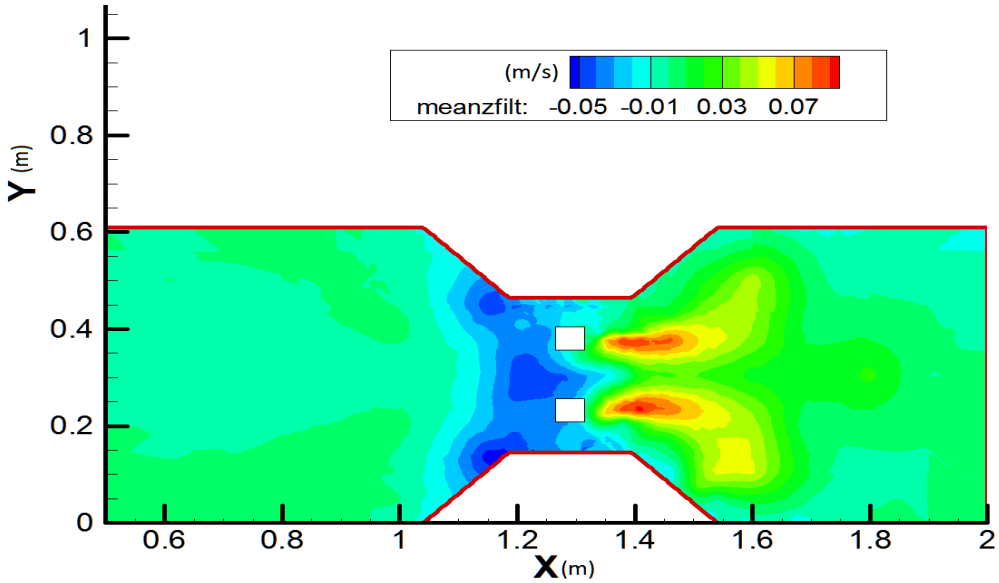

Figure 77: Vertical velocity for the small flume in the case of two square piers and the constriction

The vertical velocity is presented in Figure 77 for the small flume. A downward vertical velocity was created as the water hit the constriction and the piers with upwelling occurring as the flow exited the scour hole. The location of this downward flow was consistent with the location of maximum scour as seen in Figure 84.

4.4.3 Reynolds Stress

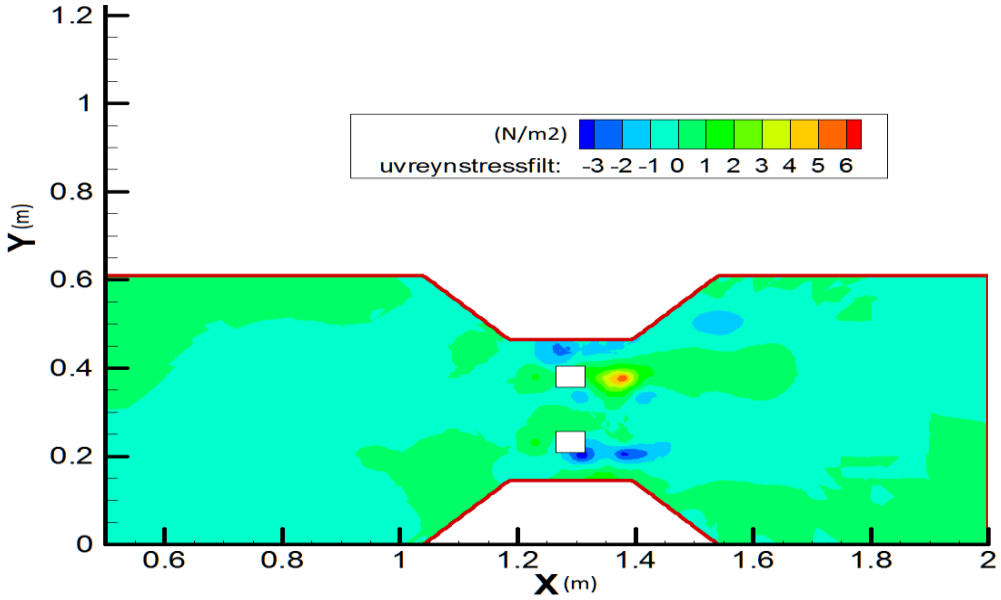

Figure 78: τ_{UV} for the small flume in the case of two square piers and the constriction

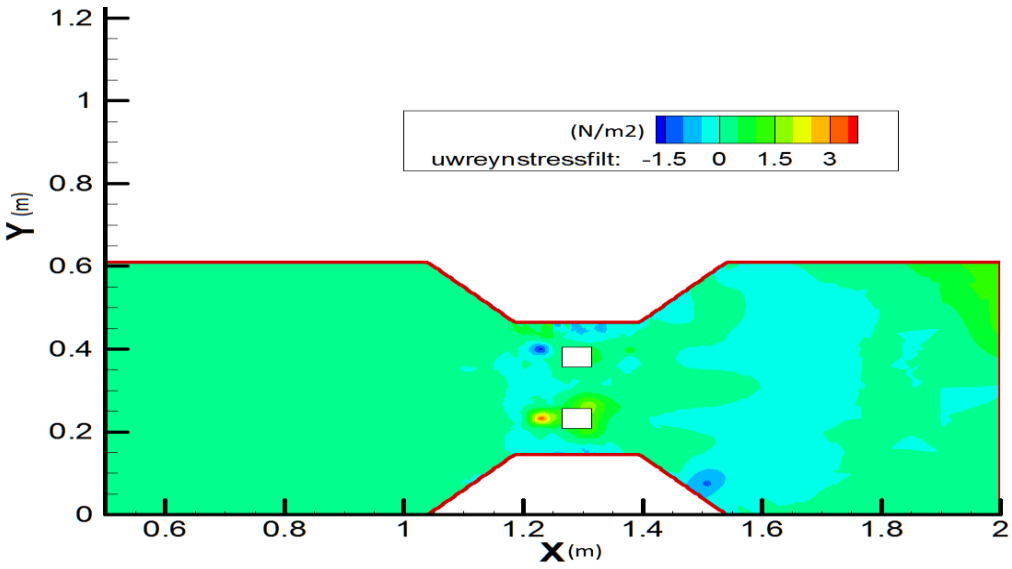

Figure 79: τ_{UW} for the small flume in the case of two square piers and the constriction

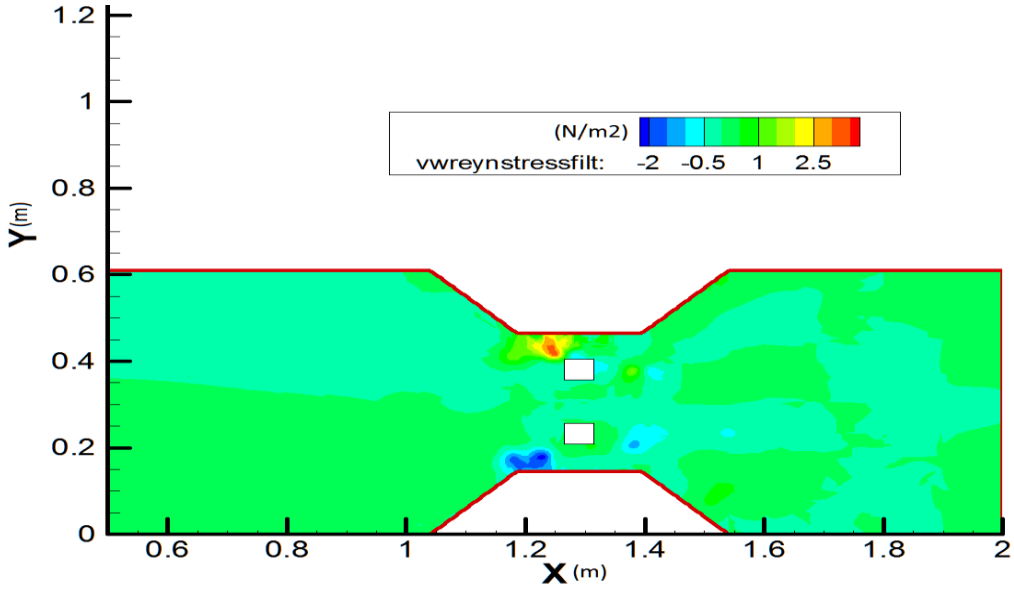

Figure 80: τ_{VW} Reynolds Stress for the small flume in the case of two square piers and the constriction

Figure 78, Figure 79 and Figure 80 show the distribution of Reynolds stresses in the UV, UW, and VW directions respectively in the small flume. The maximum Reynolds stress was found in the UV direction. In this case, the location of maximum Reynolds stress did not correspond to the location of maximum scour as shown in Figure 84.

For the case of the large flume with two square piers and the constriction, it was not possible to compare the Reynolds stress numbers with the others because the cross stream and vertical velocities were not reliable. This was due to phase wrapping.

4.4.4 TKE Distribution

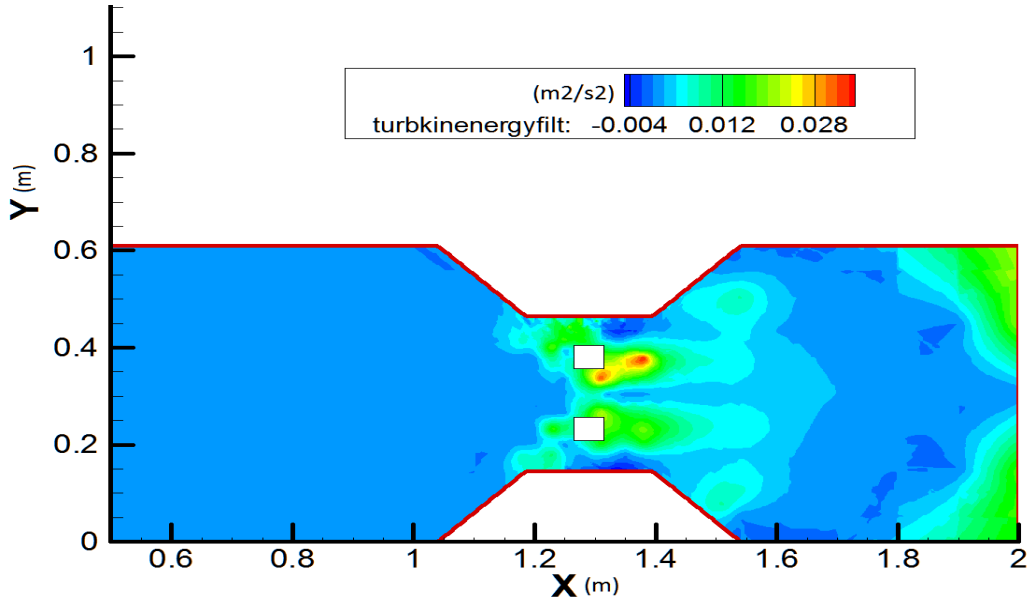

Figure 81: TKE distribution for the small flume in the case of two square piers and the constriction

For the large flume with the case of two square piers with the constriction, there were uncertainties in the cross stream and vertical velocities making it impossible to calculate the TKE and Z vorticities. Therefore, these parameters are only presented for the small flume. Looking at the TKE distribution in Figure 81, it appears that the maximum values of TKE correlate well with the locations of high scour.

4.4.5 Z Vorticity Distribution

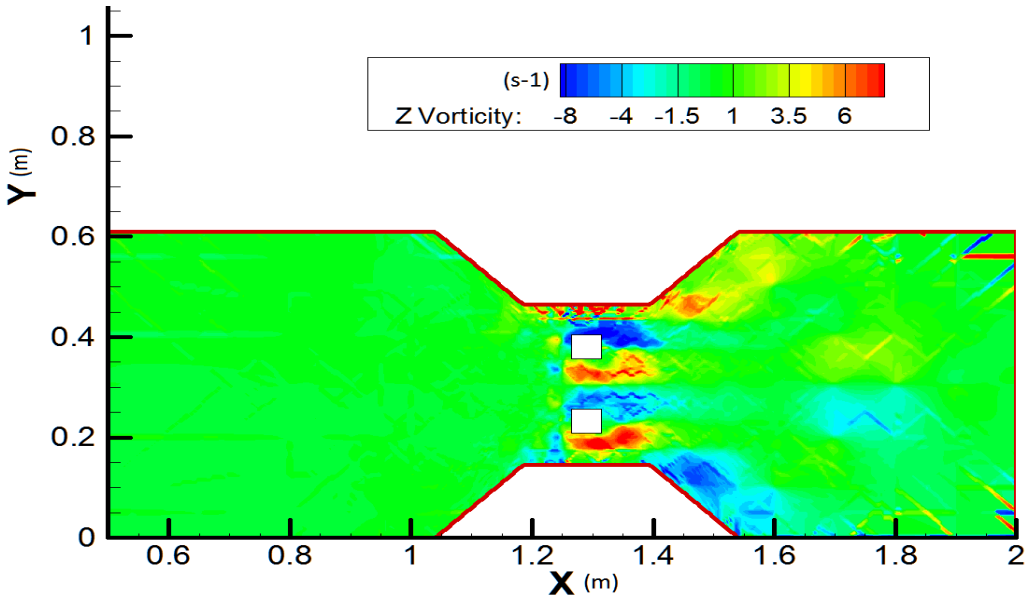

Figure 82: Z vorticity for the large flume in the case of two square piers and the constriction

The distribution of Z vorticity is presented in Figure 82. The greatest Z vorticity was -12s^{-1} and was found between the pier and the constriction. This region was located close to the area of maximum scour.

4.4.6 Scour Distribution

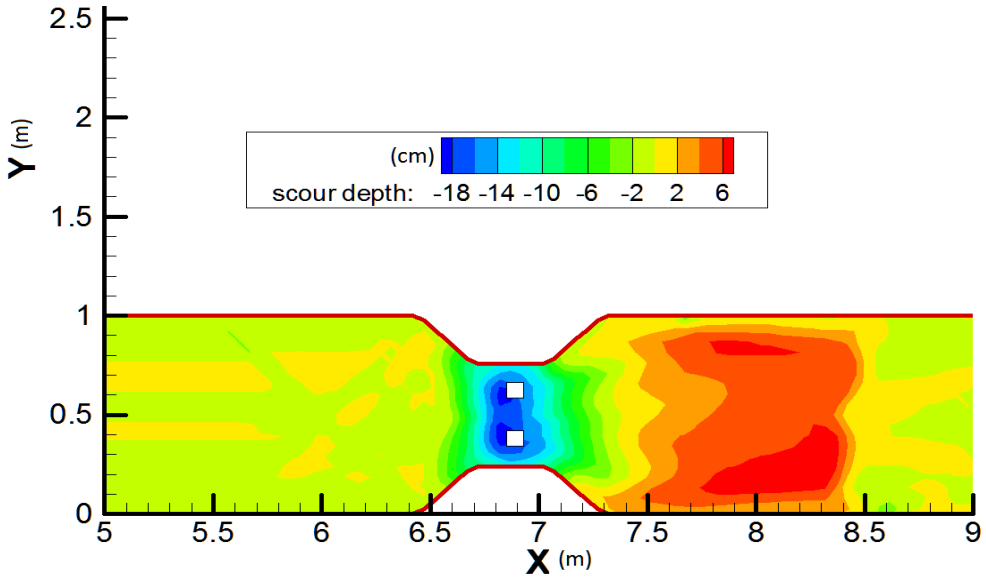

Figure 83: Scour distribution for the large flume in the case of two square piers and the constriction

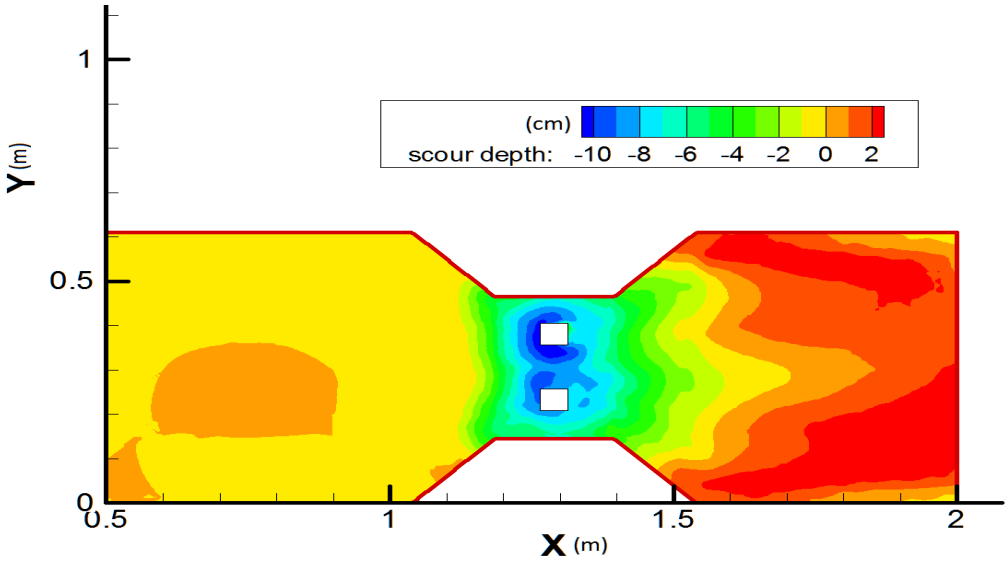

Figure 84: Scour distribution for the small flume in the case of two square piers and the constriction

The scour distribution for the case of having the pier and constriction together is shown in Figure 83 and Figure 84. It is found that for both the small and large flume, there was deep scour at the foot of the pier and a large area of deposition at the expansion. The

maximum scour depths were 18cm and 10cm for the large and small flumes respectively.

4.5 Effect of Pier Shape

In order to determine the effect of pier shape on the amount of combined local and constriction scour, experiments were performed on both circular and elliptical piers. Unfortunately, due to time constraints, velocity measurements were not taken for these cases so turbulent parameters were not calculated.

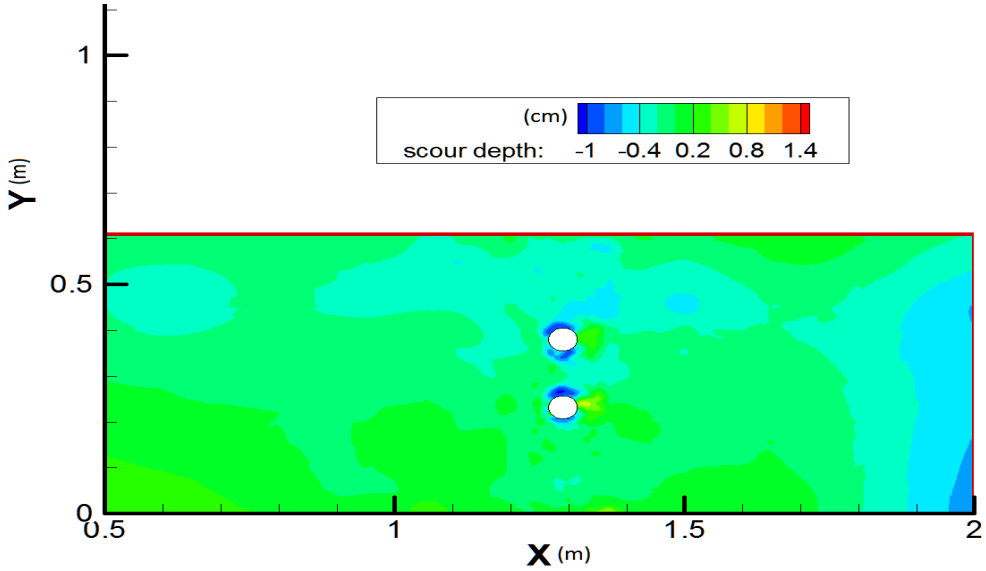

Figure 85: Scour distribution for the small flume in the case of two circular piers alone

Figure 85 shows the scouring caused by two circular piers. The scouring was reduced as compared to the case with just the square pier on its own but the distribution of the scour is similar. The scour field with two elliptical piers is not presented in the report because it was recorded that no scouring occurred.

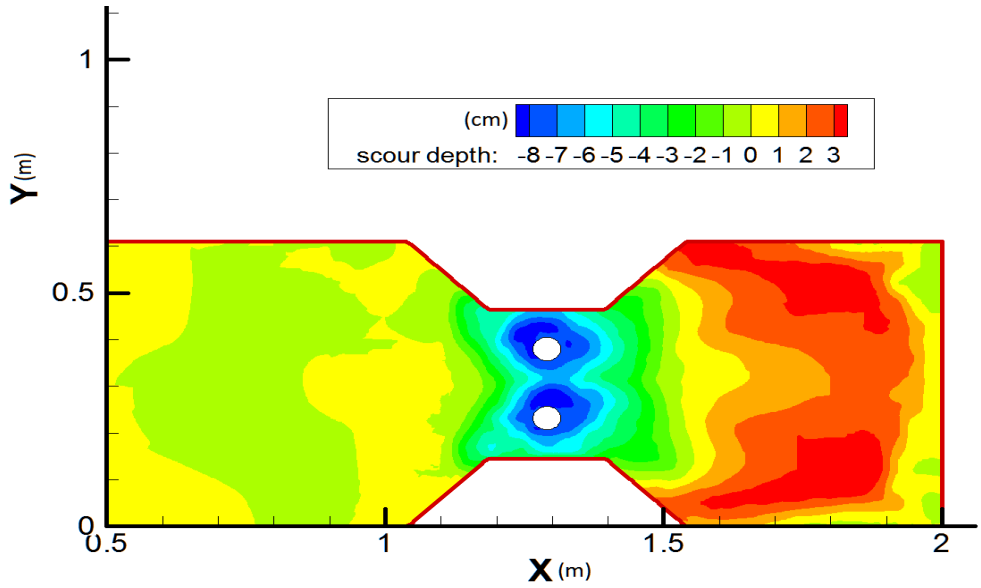

Figure 86: Scour distribution for the small flume in the case of two circular piers and the constriction

The scour result for the experiment on both the constriction and the two circular piers are shown in Figure 86. It was found that 8cm of scour was observed for the combined case. When the experiment was run with the circular pier alone, it was found that 1cm of scour occurred and with the case of the constriction alone, 4cm of scour was observed. The maximum scour depths due to the various combinations of pier shape and constrictions can be found in Table 5.

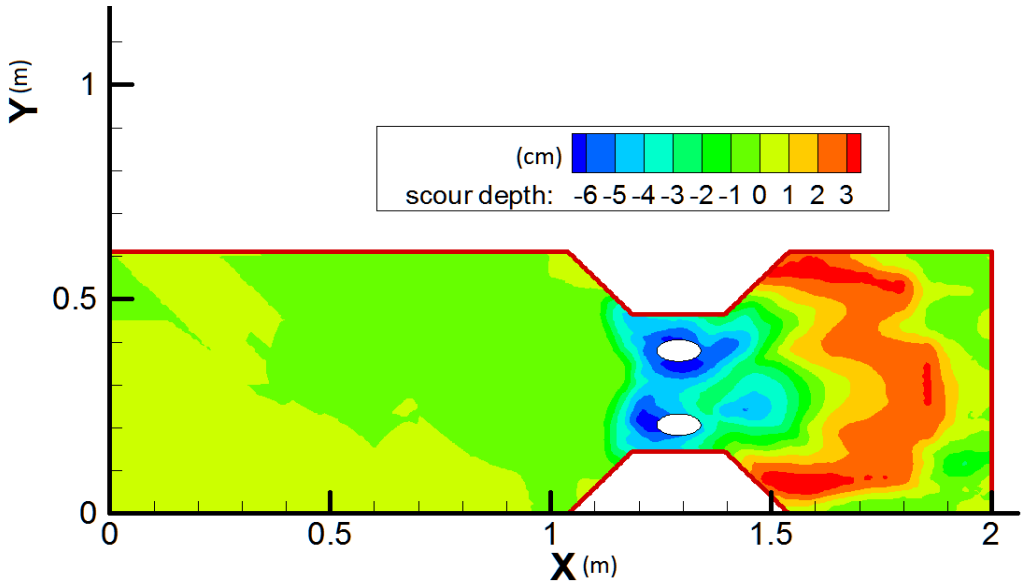

Figure 87: Scour distribution for the small flume in the case of two elliptical piers and the constriction

The scour pattern for case combined constriction and pier scour using the elliptical pier is shown in Figure 87. As stated above, the constriction by itself produced 4cm of scour while the elliptical pier alone did not produce any scour. However, when both the elliptical piers and the constriction are present, 6cm of scour was observed.

4.6 Tests with 1 square pier

In addition to studying the effect of pier shapes, experiments were also performed with one square pier instead of two which has been seen in all of the above studies.

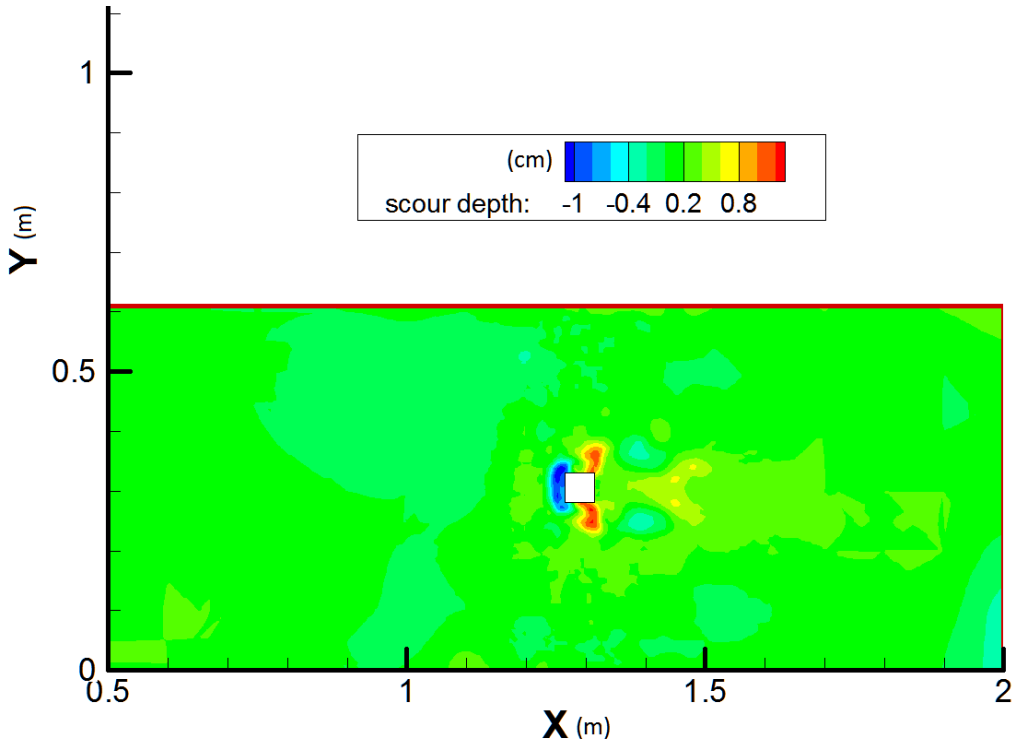

Figure 88: Scour due to one square pier only

The scour pattern for one square pier is shown in Figure 88. The scour hole was shallow compared to the other cases and occurred directly in front of the pier with deposition off to the sides.

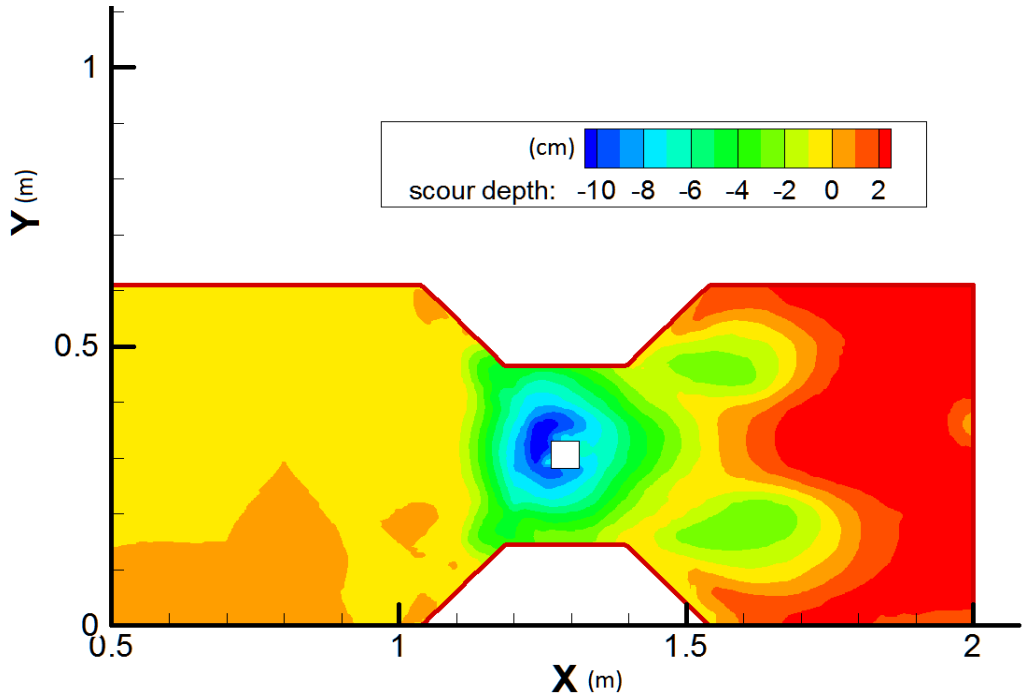

Figure 89: Scour due to one square pier and a constriction

The scour pattern for the case of one square pier and the constriction is shown in Figure 89. The scouring was 10cm deep with a large area of deposition occurring after constriction. When comparing this pattern Figure 69 which is the case with the small flume and only the constriction, one can see that the influence of one square pier has drastic effects on both the scour depth and distribution.

4.7 Summary of Results

4.7.1 Large Flume

The velocity, turbulences and scour results of the experiments performed in the large flume are shown in Table 3 below. This table enables a quick comparison between various test cases.

Table 3: Velocity and Scour Results with the large flume

Large Flume			
Arrangement	Constriction Alone	Square Piers Alone**	Constriction and Square Piers Combined

Max X Velocity (m/s)	0.35	0.34	0.28 (0.4)*
Max Y Velocity (m/s)	0.15	0.1	–
Max Z Velocity (m/s)	-0.04	-0.045	–
Max UW Reynolds stress (N/m^2)	4	-4	–
Max UV Reynolds stress (N/m^2)	2.5	-11	--
Max VW Reynolds stress (N/m^2)	-0.5	0.45	–
RMS Velocity (m/s)	0.22	0.21	--
RMS Reynolds Stress (N/m^2)	2.74	6.76	--
Scour Depth (cm)	8	14 / (**5.4** corrected)	18

**Note that for this case, the experiment was running at a higher flowrate compared to the other cases.

*unwrapped velocity in parentheses

When analyzing the large flume data, it was found that the approach velocity for the experiment with the piers alone was higher than the case with the constriction alone and the case with both the constriction and square piers. This was not part of the original experimental plan but unfortunately, it appears that this occurred during manipulation of the flume outlet gate and inlet discharge valve to obtain uniform flow of the required depth. This is an unfortunate consequence of running a large flume. The extent of the discrepancy in the inlet velocity was discovered only during the data analysis phase after the experimental apparatus had been taken apart. It is important to have the three experimental runs with the same approach velocity because it is correlated to the amount of scour.

In order to remedy the problem of a high flow rate in the case with only the square piers, the scour ratio was found for the case with the constriction only and the case

with the pier and constriction combined. The scour ratio was determined using the equation below.

$$Scour\ Ratio = \frac{Scour\ Depth}{Scour\ Depth\ + Inlet\ Flow\ Depth}$$

Calculating the scour ratio for the cases with the desired approach velocity, it was found that the results were similar between the large and small flume providing further evidence that the scaling between the flumes was performed correctly. Using the assumption that the scour ratio would be once again similar for the case of the pier alone, a new scour depth for the C02 case in the large flume was calculated to be 5.4cm.

Table 4: Scour Ratios for the large and small flumes

Large Flume (experimental)				Small Flume (experimental)			Large Flume (calculated)
	C32	C30	C02	C32	C30	C02	C02
Scour Depth (cm)	18	8	14	10	4	2.8	5.4
flow depth (cm)	12.5	12.5	12.5	7.6	7.6	7.6	12.5
scour ratio	0.59	0.39	0.53	0.57	0.34	0.27	0.3*

*assuming that the scour ratio for C02 in the large is similar to C02 in the small flume. This assumption is valid for the other two cases

4.7.2 Comparison of scouring for the three cases: Large Flume

In the case of the large flume, it was found that the constriction alone case (C30) produced 8cm of scour, while the 2 square piers alone (C02) produced 5.4cm of scouring (after correcting the scour depth using the scour ratio). On the other hand, within the large flume with both constriction and pier scour occurring at the same time (C32), a maximum scour depth of 18 cm was observed. A linear addition to determine the amount of scouring caused by both the pier and constriction at the same time would yield 13.4 cm of scour, which is substantially less than the experimental result of 18cm. Thus, the summation of individual scour components was less than the amount

measured in the combined C32 case. This is an important result because in industry, the current assumption is that the scour produced by combining pier and constriction at the same time is equal to the sum of the individual components (Arneson, 2012). Furthermore, this assumption is used because it is thought to be conservative which was not found to be true for the cases in this experiment. In the large flume experiment, the assumption that the simultaneous local and pier scour is the linear sum of the two components is not valid resulting in a 25% under prediction of scour.

4.7.3 Scour Field

As discussed above, it was found that locations of high Reynolds stresses correlate well with the regions in which high amounts scour were observed. Recalling that the Reynolds stress is due to the turbulent fluctuating components of the velocity field, it is likely that these fluctuations are causing scour. This correlation of the high Reynolds stresses at locations of deep local scour was also found in (Jamieson et al, 2013).

As seen in Table 2, the UW and UW Reynolds Stresses act upon the XY plane representing the bed. One would expect that since scouring occurs on this horizontal plane, these directions of Reynolds stress would be the highest. However, as seen in Table 5, the highest magnitude of the Reynolds Stress was in the UV direction which acts upon the YZ or ZX plane, neither of which represents the bed. This result is somewhat surprizing but is actually consistent with what was found by (Jamieson et al, 2013).

In Jamieson's study, it was explained that in the case of a sloping channel or in this case a scour hole, the UV Reynolds stress acts on the bed due to the slope of the bed. The slope of the bed determines the component of the UV Reynolds stress acting on the bed. A bed with a greater slope would have a greater component of UV Reynolds stress acting upon it (Jamieson et al, 2013).

4.7.4 Comparison of scouring for the three cases: Small Flume

As discussed previously, experiments were performed in the small flume to examine the scour and flowfield caused by obstructions. The velocity, turbulence and scour results are shown in Table 5 below.

Table 5: Velocity and Scour results for the small flume

Small Flume			
Arrangement	Constriction Alone	Square Piers Alone**	Constriction and Square Piers Combined
Max X Velocity (m/s)	0.3	0.24	0.35
Max Y Velocity (m/s)	0.1	-0.08	0.14
Max Z Velocity (m/s)	0.05	-0.025	-0.05
Max UW Reynolds stress (N/m^2)	1.4	0.75	3.5
Max UV Reynolds stress (N/m^2)	3	1.8	6
Max VW Reynolds stress (N/m^2)	2.4	-0.18	3.5
RMS Velocity (m/s)	0.19	0.15	0.22
RMS Reynolds Stress (N/m^2)	2.36	1.13	4.49
Scour Depth (cm)	4	2.8	10

4.7.5 Effect of Pier Shape

This project examined how the amount of scour is affected by the shape of the pier. This was performed on the small flume using the same flow conditions and pier size for each run. Due to the aerodynamic shape of the elliptical pier, it did not produce

appreciable scour while the circular piers and square piers without the constriction produced 1cm and 2.8cm of scour respectively.

Due to time constraints, velocity measurements were not taken for the elliptical and circular piers in the large flume but it is likely that the more aerodynamic shape of the circular and especially elliptical piers produces lower turbulence as well as a lower downflow which resulted in less scour.

4.7.6 Comparison of scouring for the three cases for non-square piers

The results of this study thus far have shown that the assumption that the combined scouring due to local and constriction scour is equal to the linear sum is not conservative for the case of a square pier. However, many piers are not square so a further goal of this study was to examine whether this result remains true for other shaped piers.

Therefore an experimental scheme using the same sized circular and elliptical piers was set up to test the assumption. This was performed on the small flume because of time constraints. The experimental set up involved determining the amount of scour in the following cases

1) Pier Alone
2) Constriction Alone
3) Pier and Constriction simultaneously

Table 6: The effect of pier shape on the scour depth

Small Flume									
Arrangement	Constriction Alone	Two Square Piers Alone**	Constriction and Square Piers Combined	Two Elliptical Piers Alone	Constriction and Elliptical Piers Combined	Two Circular Piers Alone	Constriction and Circular Piers Combined	One Square Pier	Constriction and One Square Pier Combined
Maximum Scour Depth (cm)	4	2.8	10	0	6	1	8	1	10

Table 7: Percentage Underprediction Error when assuming linear addiction to calculate combined scour

Flume Size	Piers Alone	Constriction Alone	Linear addition	Piers and Constriction	% Error
Two Square Piers (large flume)	5.4	8	13.4	18	26
Two Square Piers	2.8	4	6.8	10	32
Two Elliptical Piers	0	4	4	6	33
Two circular	1	4	5	8	38
One Square Pier	1	4	5	10	50
Two Square Piers (large flume)	5.4	8	13.4	18	26

The results are displayed in Table 6 and once again, it was found that the case of simultaneous local and constriction scour is greater than the linear sum of the two cases. The amount of underprediction error associated with adding the amount of scour linearly is 33% for the elliptical pier and 38% for the circular pier as seen in Table 7.

4.7.7 Case with one square pier

The scour depths for the experiments with one square pier are shown in Table 6. The pier alone and constriction alone cases produced 1cm and 4cm of scour effectively. Together, the experiment shows that 10cm of scour is produced which is significantly greater than 5cm (1cm+ 4cm) which would be the result of a linear addition. As consistent with the summary in Table 7, there is a large (50%) error due to linear addition of local and constriction scour.

4.8 Comparison Between the Turbulent Statistics and Scourfield

It is expected that the turbulence caused by the obstructions (piers, constrictions) lead to turbulence which then contribute to scour. The table below compares various turbulent statistics and whether or not they are correlated to the scour pattern.

Table 8: Correlation of velocity and turbulent parameters to obstructions

Test Number	Test Description	X Velocity	Y Velocity	Z Velocity	UV RS	UW RS	VW RS	TKE	Z Vorticity
1	2 Square Pier + Constriction	Yes	NA	NA	NA	NA	NA	NA	NA
2	Constriction Alone	No	Yes	Yes	Yes	Yes	Yes	Yes	Yes
3	2 Square Piers Alone	Yes	Yes	Yes	No	Yes	No	Yes	Yes
4	2 Square Pier + Constriction	Yes	Yes	Yes	No	Yes	Yes	Yes	No
5	Constriction Alone	No	Yes	Yes	No	Yes	Yes	Yes	No
6	2 Square Piers Alone*	Yes	Yes	Yes	No	No	No	Yes	Yes

It was found that the Y and Z velocity and Turbulent Kinetic Energy are always well correlated to the scour field. Reynolds stress in the UW component is correlated to the scour field except for in the two piers alone case in the small flume.

5 Discussion:

5.1 Reliability of Results: Large Vs. Small Flume

5.1.1 Reynolds Stress

One should note that part of the reason the Reynolds stress results differ between the large and small flume is that in the small flume the measurements we taken closer to the bed. Taking measurements closer to the bed yielded results that were more influenced by the equilibrium bathymetry and also the horseshoe vortex. This general statement applies to all test cases but is very prominent when comparing the Reynolds stresses between the large and small flumes in the case of the constriction alone.

5.1.2 Scour Distribution:

One advantage with the small flume was that since the area was smaller, it enabled a measurement grid with greater relative density, which produced more detailed results of the scour field.

5.2 Applicability of Linear Addition

In the field of bridge design, the situation of combined pier and constriction scour happens frequently. This is because when bridges are built at narrowing channels, less material cost is required than if a bridge were built at a wider section. A complication added to this cost saving measure is that in addition to the local scour at the pier, there is also constriction scour due to the narrowing of the bridge. In order to design for this situation, engineers must calculate the amount of total scour which is assumed to be the sum of the local scour and the constriction scour (Arneson et al, 2012) (Melville & Coleman, 2000).

However, a detailed literature review has suggested that there has been no previous research in the applicability of this assumption. Therefore, the main goal of this project was to perform experiments to determine whether this assumption is valid. The experiments were arranged such that the amount of scour was determined for the following cases.

1) Pier alone → to observe local scour
2) Constriction alone → to observe constriction scour
3) Pier and Constriction combined → to observe both local and constriction scour simultaneously.

Conventionally, case 3 is assumed to be the sum of case 1 and case 2 but for this thesis, results for all three cases were available so comparisons were made between the cases. Since square, circular and elliptical piers were used, analysis also determined whether the assumption of linear additively would hold for various pier shapes.

As seen in Table 5, case 3 is greater than case 1 and case 2 combined meaning that the assumption that for the case with local and constriction scour, the sum is greater than the individual components. For the blockage ratios tested which were between 0.1 and 0.6, assuming that the total amount of scour is the sum of the pier alone and the constriction alone severely under predicts the scour. It is therefore recommended that a factor of safety be used when predicting the combined pier and constriction scour. Based on the present experiments, the factor of safety should be at least 1.6 (see Tables 4 and 5), but further experimentation is required to determine a factor of safety appropriate for all design situations.

5.3 Improper Scaling

In order to save time, two different flumes were used. The large flume has the advantage of being closer to the physical representation but with the small flume, data can be collected quicker so more cases can be run within the same time frame. Also, it is more convenient to get the initial sand bed to be flat after the experiments with the small flume making it possible to perform more experiments. A more complete discussion of the advantages and disadvantages of the flumes can be found in the Methods section.

In order to scale the flow between the two flumes, Froude scaling was used. This means that the Froude numbers for the experiments within the two flumes should be the same. However, as seen in Table 1, this was not the case for all runs because of difficulties in replicating the flow depth and velocity between the flumes. Since the scaling was not perfect, it is difficult to make direct comparisons between the large and small flume data. Even so, it is still possible to compare the general pattern of the flow field as was completed in the results section.

One main difference between the large and small flume is that since the large flume is longer, it allows more time for the velocity profile to develop. It is interesting that both a well-

developed flow field (large flume) and a less developed flow field (small flume), show that the assumption of adding the scour due to constriction and local scour together linearly is not conservative.

5.4 Relative Depths

For the large flume, the flow field was measured at a relative depth of 48 % while for the small flume, it was measured at the relative depth of 26%.

Ideally, it would have been good to measure both flow fields at the same relative depth in order to have a direct comparison of the two flow fields. The measurements in the large flume were performed earlier with a relative depth of 48% from the initial bed surface. This measurement plane was selected so that that the velocity in the measured plane would be close to the mean profile velocity at each individual measurement location, which is typically at about 40% of the total depth from the bed. Ideally, the flow field would have been measured at the same relative depth in the small flume experiments that were performed months later. However, this was not possible because the ADV needed to be submerged, but at the same time the sample volume was 5cm away from the probe tip. Due to the limited flow depth that was required by Froude scaling in the small flume (7.6 cm), the flow field had to be measured at 26 % of the flow depth from the bed surface.

The discrepancy between the flow depths is acceptable because in this study flow field numerical values were not compared directly between the two flumes; rather, the relative shape of the two flow fields was compared.

5.5 Oddities in the Results

5.5.1 Cross Stream Velocity, Piers only

Looking at Figure 30 and Figure 31, it appears that there is a greater coherent structure in between the piers for the small flume than the large flume. In fact, Figure 30 does not show the flow moving in between the piers as one would expect and as is shown in the small flume. This is best explained by the fact that due to time limitations, within the large flume, the measurement density was lower. This made it so that a measurement that would have captured this flow convergence in between the piers was not made. Had a velocity measurement be taken at this point, it is suspected that the cross stream velocities between the large and small flumes would compare better.

5.5.2 Reynolds Stress, Piers only.

There is a large difference in the Reynolds Stress distribution between the small and large flume. An example of this can be seen in Figure 36 and Figure 37. The large flume plots show the wake vortices very clearly while this is not the case for the small flume. This is likely due to the fact that the small flume measurements were taken at a lower plane which allowed it to be more influenced by the horseshoe vortex in the scour hole as well as the zones of erosion and deposition.

5.5.3 Scour Distribution, Piers Only.

By examining the scour distribution for the pier only case as shown in Figure 46 and Figure 47 , one difference that can be observed is that with the large flume the scour holes connect, while with the small flume this does not occur. This is likely an artifact of the non-ideal sediment scaling that was used. There was not enough shear stress in the small flume to move the sediment to the same degree.

As explained in Section 3.4, in order to satisfy Shields scaling, it would have been best to use a small sediment size for the smaller flume. However, when tests were performed with the next smallest sediment size which has d_{50}=0.7mm as opposed to the large flume which had a d_{50}=1.0mm, it was found that scouring occurred to the bottom. Therefore, it was decided that both tests would use sand with a d_{50} of 1.0mm even though perfect Shields scaling would be sacrificed. This was one of the results of this decision.

5.5.4 Vertical Velocity, Constriction Only.

When comparing the vertical velocities for the case of the constriction only as seen in Figure 56 and Figure 57, it was found that for the small flume, there was a downward vertical velocity in the expansion zone while this did not exist for the large flume.

The scour distribution shown in Figure 69 does not readily explain why this occurred so it is likely that this is due to the three-dimensional recirculation eddy. The measurements would indicate that the down flow section of this recirculation area occurred at the bottom of the large flume and towards the middle of the large flume.

5.6 Comparison to previous studies

Although there have not been any studies on the amount of scour due to a simultaneous pier and constriction, there have been other studies that can be used to validate the results of this experiment. In general, these studies examine scour and present turbulent statistics that are useful in support of this thesis. (Jamieson et al, 2013) studied the scour caused by stream barbs and how they can be related to the turbulent parameters similar to the ones in this thesis. (Dey et al, 2007) examined the development of a scour field due to a square pier providing detailed turbulent statistics

5.6.1 Turbulence and Vorticity in a Laboratory Channel Bend at Equilibrium Clear-Water Scour with and with Stream Barbs (Jamieson et al, 2013)

Jamieson in 2013 performed a study on the effect the turbulence and vorticity in a bent laboratory channel with and without barbs. Barbs are used to prevent erosion by directing the flow away from the river bank. One of the goals of this study was to examine the effect of barbs on the z-vorticity, Reynolds stress and the scour field. Six different experiments were run varying the flowrate and the number of barbs. It was found that for the cases with more barbs, there were higher values of TKE measured because the barbs created more mixing, overtopping and flow separation. Jamieson et al. hypothesized that the barbs created a more varied flow field which then resulted in high fluctuations in streamwise and cross stream velocities explaining the increased Reynolds Stress and TKE.

A somewhat surprising result that came out of Jamieson's study was that in the locations of scour, the highest Reynolds stresses were in the streamwise and cross stream direction. This was not expected because this component of the Reynolds stress acts on a vertical plane. One would expect that the principal vertical streamwise Reynolds stress would be greatest because it is a measure of the shear on the horizontal plane in the streamwise direction. The explanation provided by the authors was that since the scour hole develops a slope, a component of the streamwise / cross stream Reynolds stress is able to act on the scour hole and cause erosion.

Another result that came from (Jamieson et al, 2013) is that large z-vorticity values were associated with the scour holes and barbs. The authors explained that the high values of z-vorticity are due to the velocity gradients caused as the water accelerates around the barbs. These rotations show up as vorticity and produce velocity gradients near the bed which create shear stress leading to scouring.

Fundamentally, there are similarities between the study of flow around barbs on a bent flume and flow around a constriction and piers in a straight flume. The barbs, constriction and piers all increase turbulence and cause scour within the flow field. The first similarity discovered when comparing the results of the two studies is that high values of TKE were discovered around both the piers and the barbs. This is explained by the fact that the piers and constrictions disturb the flow by creating mixing and possible flow separation which increases the turbulence.

Another similarity is that both this thesis and the study by Jamieson et al. report that the highest component of Reynolds stress occurs in the scour holes and is in the streamwise – cross stream component. Just like the study by Jamieson et al., the scour holes caused by the constriction or piers have a significant slope so it is possible that although the streamwise – cross stream Reynolds stress acts upon the vertical plane, a component contributes to scouring.

By looking at the plots of Z vorticity and comparing them to the scour holes, one can find that there is a correlation between these two parameters as was found by Jamieson. The explanation that vorticity is represented by near bed velocity gradients leading to shear stress causing scouring seems to be applicable for the explanation of the correlation between Z vorticity and scouring within this study.

5.6.2 Characteristics of Horseshoe Vortex in Developing Scour Holes at Piers (Dey & Raikar, 2007)

A study was performed by Dey in 2007 to study characteristics of the horseshoe vortex in a scour hole caused by a circular and a square pier. Detailed measurements of the flow field at various stages leading up to equilibrium were taken. One trade-off of the Dey study was that since it focused so heavily on measurement of the scour hole flow field, the approach flow field was not measured so it is difficult to examine how the flow changes as it approaches the

piers. However, it is still beneficial to compare turbulence parameters such as vertical velocity, TKE, and Reynolds stresses between this thesis and Dey's work.

Even though only velocity measurements very close to the pier were taken, Dey measured negative vertical velocities for both the circular and square piers, just before the water impacts the piers. This diving flow was also measured in this thesis providing a form of validation.

Another parameter to compare was TKE. It was found in this thesis that TKE was highest in the scour holes as seen in the results section. This trend was also observed by Dey. Dey shows that for both the circular and square piers, the highest value of TKE occurs within the scour hole which is again consistent with the results of this thesis.

Dey presented contours of UV, UW and WU Reynolds stresses in his paper. By studying these, one comes up with the fact that the Reynolds stress component with the greatest magnitude was the UV component, which is consistent with (Jamieson et al, 2013) as well as this thesis. Once again, this result is surprising because the UV Reynolds stress acts upon the vertical plane and one would expect that the Reynolds stress component acting horizontally to be highest. However, just as in this thesis and (Jamieson et al, 2013) the scour hole in Dey's experiment is sloped so a component of UV may very well be acting on the scour hole and causing erosion.

In Dey's experiment, the equilibrium scour generated by one circular pier was 16cm while one square pier produced 20cm. This is expected because the square pier produces more flow separation, translating into turbulence and then scour. For this thesis, two circular piers on their own produced 1cm of scour while two square piers on their own produce 2.8cm of scour. It is expected that the square piers generate more scour than the circular piers but it is interesting to note that in this thesis, the two squares produce 2.8 times the amount of scour

as two circular piers while comparing one circular pier to one square pier as done by Dey, only shows that the square pier produces 1.25 as much scour. A possible explanation for the difference is that with two piers, the effect of the flow separation is magnified causing more disruption to the flow field which translates to more turbulence and therefore scour.

5.6.3 Comparison with Traditional Bridge Scour Equations:

The data collected in this thesis were compared with traditional scour equations to see how they would fare. The Richardson and Davis equation (Melville & Coleman, 2000) was used and predicted 0.64cm for one square pier in the small flume while the experimental result was 1.3cm. Contraction scour was predicted using an equation provided in (Melville & Coleman, 2000) to be 0.11cm in the small flume while the experimental result was 4cm. It appears that the traditional equations underestimate both local and constriction scour.

5.7 Scour Depth vs. Blockage Ratio

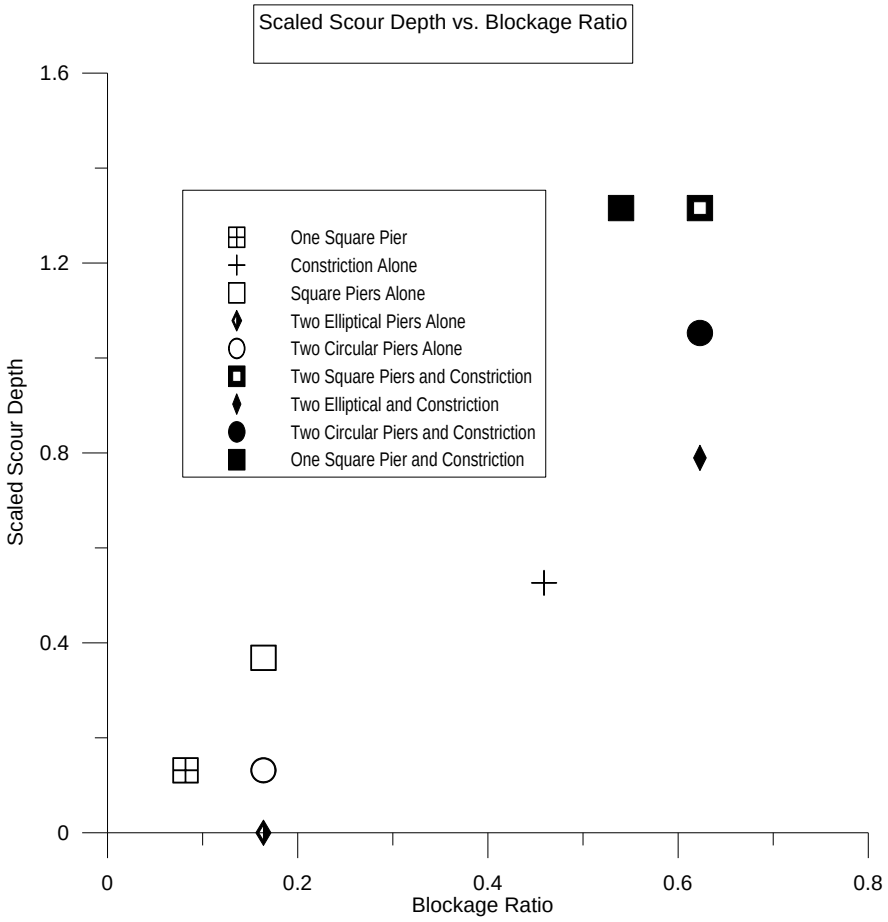

Figure 90: Scour depth versus Blockage Ratio as performed in the small flume

Figure 90 above displays a chart of the blockage ratio to the scour depth. The blockage ratio is the proportion of the flume that is blocked by either the piers or the constriction in comparison to original width. Using data from the flume experiments, it was found that as the blockage ratio increases, the scour depth increases for the same shape of piers. This can be explained by the increased acceleration by the blockage.

Another factor is the shape of the piers. Given the same blockage ratio, the more "aerodynamic" piers produce less scour. This is explained by the fact that less turbulence is caused by these piers producing less shear stress and therefore less scouring. Even with a smaller blockage ratio, the one square pier produces more scour than two elliptical piers and equivalent scour to two circular piers under the experimental conditions of this thesis.

6.0 Conclusion

Scouring is a leading cause of bridge failure. This study aimed to reduce this by gaining a better understanding of the mechanisms behind scouring. In particular, the study examined the case of combined constriction and pier scour. Currently the practice in industry is to determine the scour depth from the pier and constriction separately and use the linear sum to predict the amount of total scour for a case in which both types of scour occur (Arneson, 2012).

For the blockage ratios tested this study which ranged from 0.1 to 0.6 it was found that when in the case of simultaneous pier and constriction scour, the linear sum of the two components is less than the amount observed in a case where both are present.

7.0 Recommendations

It is recommended that factor of safety be applied to account for the experimental results described in the conclusion section above. From the four test cases observed in this study, it has been found that adding up the individual components underestimates the combined case by between 26% and 38 %. The factor of safety should account for this.

7 Directions for Future Study

The implications for this study are profound and applicable to industry. However, only four experiments which enabled the comparison between the various combinations of scour were performed. Thus far, experiments have been performed on double square, elliptical and circular piers and well as one square pier with two experiments of different scales being performed on two square piers. Due to time restrictions, the cases with the elliptical and circular piers were performed on a small scale so it would be interesting to see if the results change for a larger scale.

All the experiments used the same constriction ratio so one direction of future research would be to vary the constriction ratio and see how that will change the scour depth. This is important because in practice, bridges are being built are various severities of constrictions.

Numerical methods are generally less costly than experiments so one idea could be to use a computer model in order to calculate the amount of scour for various pier and constriction combinations. During this research project, the numerical Reynolds Averaged Navier Stokes (RANS) model SSIIM was used to evaluate pier and constriction scour, but it was found that this model could not produce the similar scour distribution to what was observed in experiments. In particular, SSIIM could not produce scour at the front of the pier associated with down flow. Perhaps a different model would produce better results. In particular, a model that can predict sediment transport associated with the horseshoe vortex generated by the down flow may prove more useful. A 3D Unsteady Reynolds Averaged Navier Stokes model was developed by (Ge & Sotiropoulos, 2005) which can capture the unsteady vortices generated. Another model was recently developed which can predict the initial stages of erosion around a pier (Escauriaza & Sotiropoulos, 2011). Due to the intense computational resources required, neither model is ready for commercial usage. Therefore the development of a suitable model remains a goal for future research.

Bibliography

A. Roulund, B. M. (2005). Numerical and experimental investigation. *J. Fluid Mech*, vol. 534, pp. 351–401.

Arneson, Z. L. (2012). *Evaluating Scour at Bridges.* Fort Collins, Colorado: Office of Bridge Technology, National Highway Institute.

Chabert, J. a. (1956). Etude des affonillements author des. *Laboratoire National d'Hydraulique,*, Chatou, France.

Coleman, M. &. (1997). *Bridge Scour.*

Conway, J. (2004). USGS.

Dey et al. (2007). *Journal Of Hydraulic Engineering*.

Dey, S., & Raikar, R. (2005). Scour in Long Contractions. *JOURNAL OF HYDRAULIC ENGINEERING*, 1036-1049.

Dey, S., & Raikar, R. (2007). *Journal of Hydraulic Engineering "Characteristics of Horseshoe Vortex in Developing Scour Holes at Piers*, 399-413.

Dot. (2013). *Bridge Scour Manual.* Queensland: Department of Transport and Main Roads for Queensland.

Duc, B. M., & Rodi, W. (2008). Numerical Simulation of Contraction Scour in an Open Laboratory Channel. *Journal of Hydraulic Engineering*, 367-377.

Escauriaza, C., & Sotiropoulos, F. (2011). Initial stages of erosion and bed form development in a turbulent flow around a cylindrical pier. *Journal of Geophysical Research*, 1-24.

Ettema, R. (1980). *"Scour at bridge piers.".* Auckland, New Zealand: Univ. of Auckland.

Ettema, R. M. (1998). "On Scour at skewed piers". *Journal of Hydraulic Engineering*, 756-760.

Federico, F. (2003). Scour Vulnerability of River Bridge Piers. *Journal of Geotechnical and Geoenvironmental Engineering*, 890-899.

García, M. H. (2008). *Sedimentation Engineering.* ASCE Productions.

Ge, L., & Sotiropoulos, F. (2005). 3D Unsteady RANS Modeling of Complex Hydraulic Engineering Flows. I: Numerical Model. *Journal of Hydraulic Engineering*, 800-808.

Jamieson et al, E. C. (2013). Turbulence and Vorticity in a Laboratory Channel Bend at Equilibrium Clear-Water Scour with and with Stream Barbs. *Journal of Hydraulic Engineering*, 259-268.

Kirkgozl, M. S., & Ardichoglu, M. (1997). Velocity Profiles of Developing and Developed Open Channel Flow. *Journal Of Hydraulic Engineering*, 1099-1105.

Kwaku Oben-Nyarko, M. a. (2011). Pier and Abutment Scour Interaction. *JOURNAL OF HYDRAULIC ENGINEERING*, 1598–1605.

Lee, O. S., & Sturm, T. W. (2009). Effect of Sediment Size Scaling on Physical Modeling of Bridge Pier Scour. *JOURNAL OF HYDRAULIC ENGINEERING*, 793-802.

Melville, B. W. (1999). "Time scale for local scour at bridge piers.". *J. Hydraul. Eng*, 59–65.

Melville, B., & Coleman, S. (2000). *Bridge Scour.* Highlands Ranch, Colorado: Water Resources Publications.

Nortek. (n.d.). *Nortek Support Website*.

Oliveto, G. a. (2002). Temporal evolution of clear-water pier and abutment scour. *J. Hydraul. Eng*, 811–820.

Prashun, A. (1992). *"Fundamentals of Hydraulic Engineering".* New York: Oxford University Press.

Queensland, G. o. (2013). *Bridge Scour Manual.* Queensland: Government of Queensland, Department of Transport and Main Roads.

Raikar, S. D. (2005). Scour in Long Contractions. *JOURNAL OF HYDRAULIC ENGINEERING*, 1036-1049.

Rennie, & Hay. (2010). Reynolds Stress Estimates in a Tidal Channel from Phase-Wrapped ADV Data. *Journal of Coastal Research*, 157-166.

Rennie, C. (2009). CVG 3116 Lecture Notes . *Hydraulics Class.* Ottawa: University of Ottawa.

Rennie, C. (2011). River Hydraulics Course. Ottawa: University of Ottawa.

Rennie, C. (2012). *"Sediment Transport: Course Notes".* Ottawa: University of Ottawa.

Rennie, C. a. (2010). Reynolds Stress Estimates in a Tidal Channel form Phase-Wrapped ADV Data. *Journal of Coastal Research*, 157-166.

Richardson, E., Simons, D., & Lagasse, P. (2001). *RIVER ENGINEERING FOR HIGHWAY ENCROACHMENTS.* http://www.engr.colostate.edu/~pierre/ce_old/classes/ce717/FHWA-NHI-01-004.pdf: National Highway Institute.

Richardson, J., & Richardson, E. (2008). *Bridge Scour Evaluation, Sedimentation Engineering.* Reston, Virginia: American Society of Civil Engineers.

Roads, D. o. (2013). *Bridge Scour Manual.* Queensland, State of .

Simarro, G., Fael, C. M., & Cardoso, a. A. (2011). Estimating Equilibrium Scour Depth at Cylindrical Piers in Experimental Studies. *JOURNAL OF HYDRAULIC ENGINEERING*, 1089-1093.

Water Survey of Canada. (2004). WSC-02 - ADCP Principles.

Appendix A: Photos of Experiments

Figure 91: Photo of Scour Pattern for the case of the constriction alone in the large flume

Figure 92: Photo of the Scour Pattern for the case of both the constriction and pier in the large flume

Figure 93: Small Flume - Constriction and two elliptical piers

Figure 94: Small Flume- Constriction Only

Figure 95: Small Flume- constriction and two square piers

Figure 96: Small Flume - Two Square Piers

Figure 97: Small Flume- Constriction and two circular piers

Appendix B: 2D Interpolation in tecplot

In order to interpolate in tecplot, there are 2 major steps. The first is to create the grid for interpolation and then use this grid to interpolate the data. For this thesis, the grid generation was produced in SSIIM

Grid Generation in SSIIM

1) Open SSIIM and a box will appear asking for the dimension of the flume and the number of lines in the streamwise and cross stream directions. The number of lines will determine the gridding for interpolation
2) This next step will guide the user to make a constriction. Skip this if no constriction is required for the flume.
    a. View → grid editor
    b. Define → no move points mode
    c. Click the edges of the desired constriction
    d. Define → give coordinates: type in new coordinates
    e. Generate→ Transfinite I
    f. Generate → Boundary
    g. Generate → implementation
3) File→ Write tecplot 2D file

Following these steps will create a grid for interpolation that can be read by tecplot. This is still not in the format that tecplot requires for interpolation that is covered in the next step.

Generation of Required Files

Grid

1) Open up tecplot and click load→ data file
2) Grid will load with the amount of cells previously defined in SSIIM
3) Write → data file
    a. Save as .plt
4) This creates a grid which can be loaded into the tecplot data loader (for the next step)

Data

1) Take data from Excel and copy it into notepad
    a. Headings must be in quotations, eg “x velocity”
2) Open up tecplot and click → open data file
3) Save this as type .plt

Now there should be two (2) .plt files. This is the file type that tecplot needs in order to be able to use the tecplot data loader for interpolation.

Interpolation:

1) Open up the grid.plt file

2) Click→ load data file → tecplot data loader→ Option: add to current data set
    a. Now both the grid and data files are in the same window of tecplot. Interpolation can begin
3) From the top menu click data→ interpolate → kriging
    a. Source zone → data
    b. Destination zone → grid
    c. You will need to label these but it should be apparent as tecplot will show variable ranges
    d. Select “no drift” under the drift menu
    e. Other settings are:
        i. Range: 0.3
        ii. Zero Value: 0
        iii. Point Selection: Octant
        iv. Amount of Points: 8
    f. Compute → interpolate
    g. Interpolation will take a few seconds to a minute depending on the amount of fields
    h. Check box called “contour” to the left of the screen and click on the desired variable

Appendix C: Velocity Profiles

The following appendix contains velocity profiles that were not presented in the thesis. The elevations are from the bottom of the scour bed so in some areas, the depth can exceed the nominal flow depth.

Velocity Profiles for the Large Flume with only the constriction [C3O]

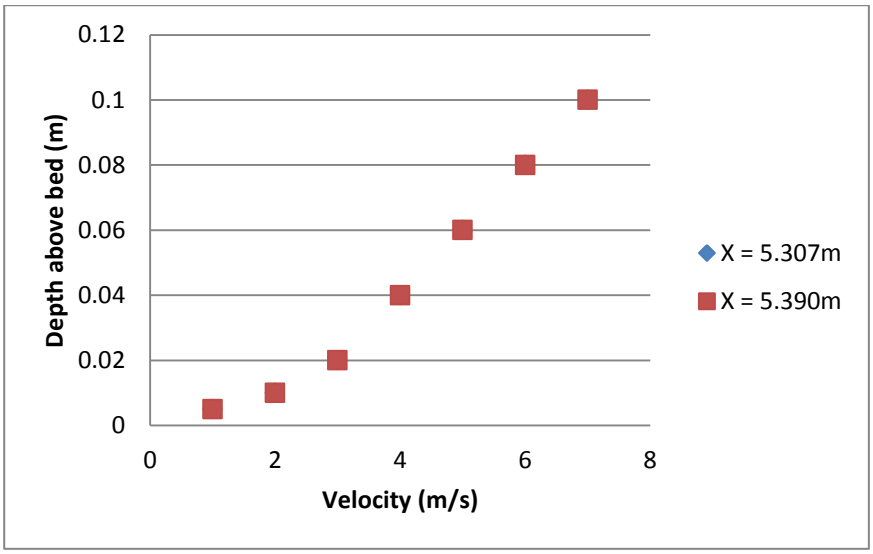

Figure 98: Centerline Velocity for C30 at two points

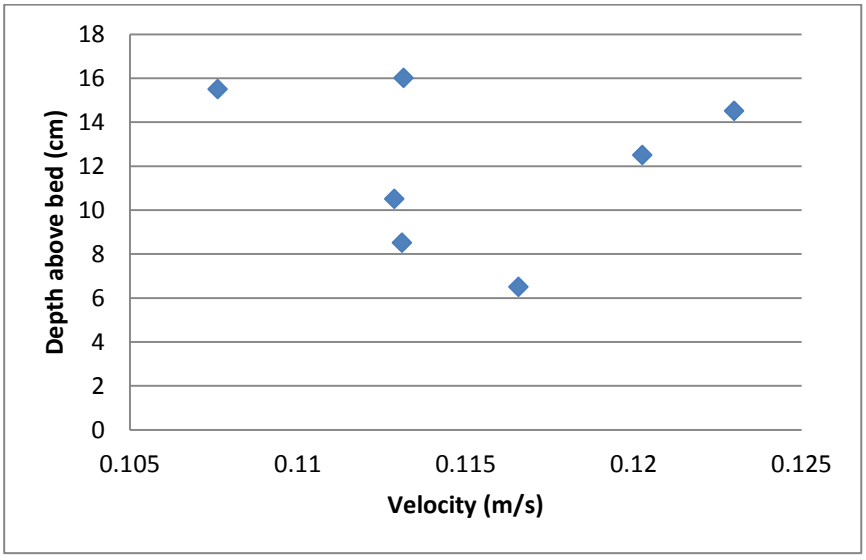

Figure 99: Velocity Profile for Large C30: x = 5.875m, y = 0.306m

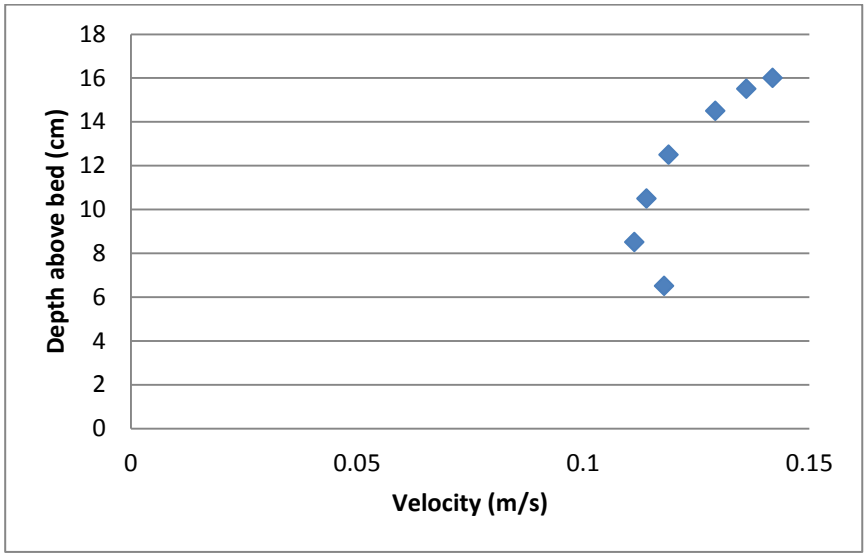

Figure 100: Velocity Profile for Large C30: X = 5.88m, Y = 0.66m

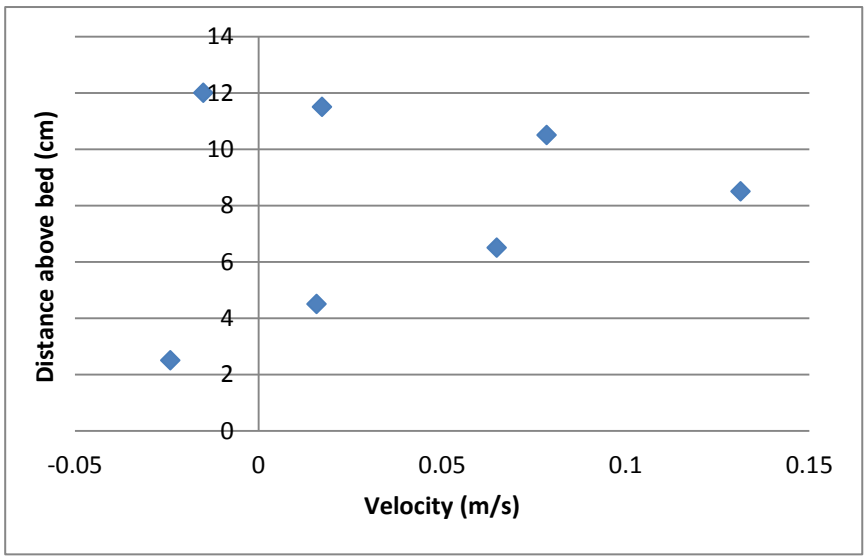

Figure 101: Velocity Profile for Large C30 X=5.9m, Y = 0.27m

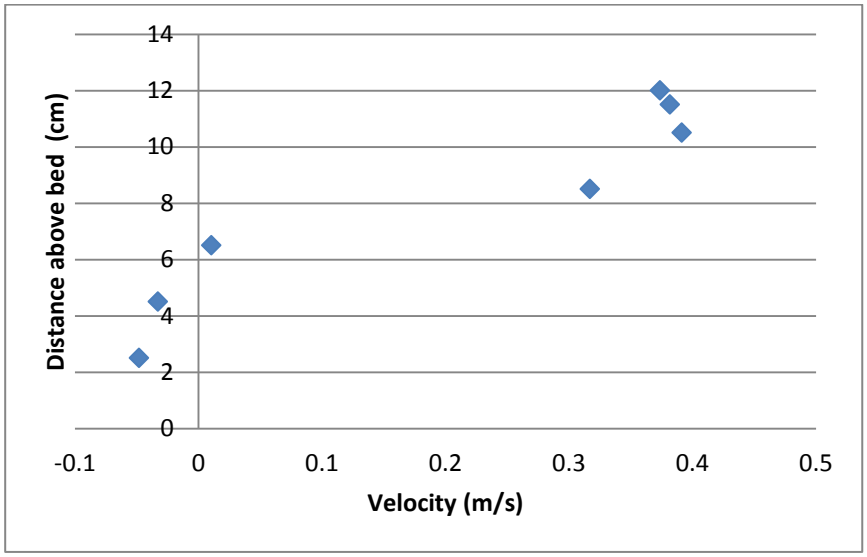

Figure 102: Velocity Profile for Large C30: X = 5.93, Y = 0.69m

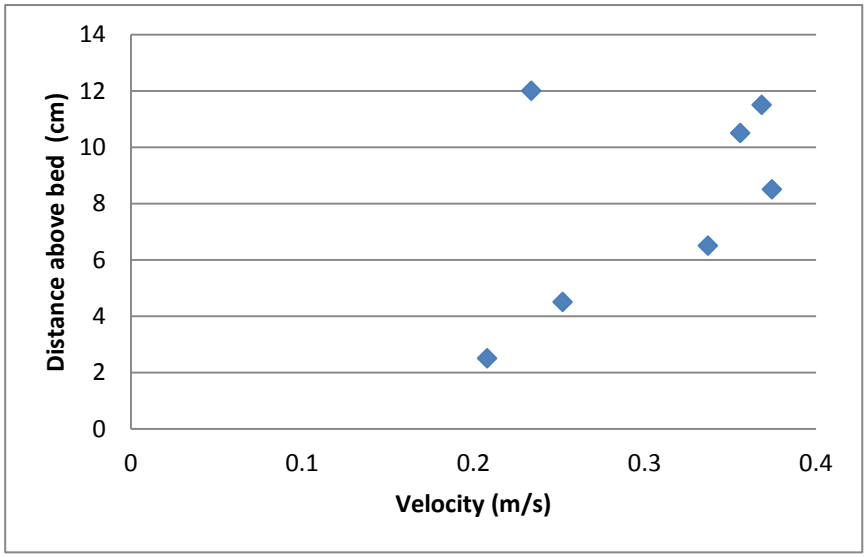

Figure 103: Velocity Profile for Large C30 X = 6.2m, Y = 0.73m

Velocity Profiles for the Small Flume with only the constriction [C3O]

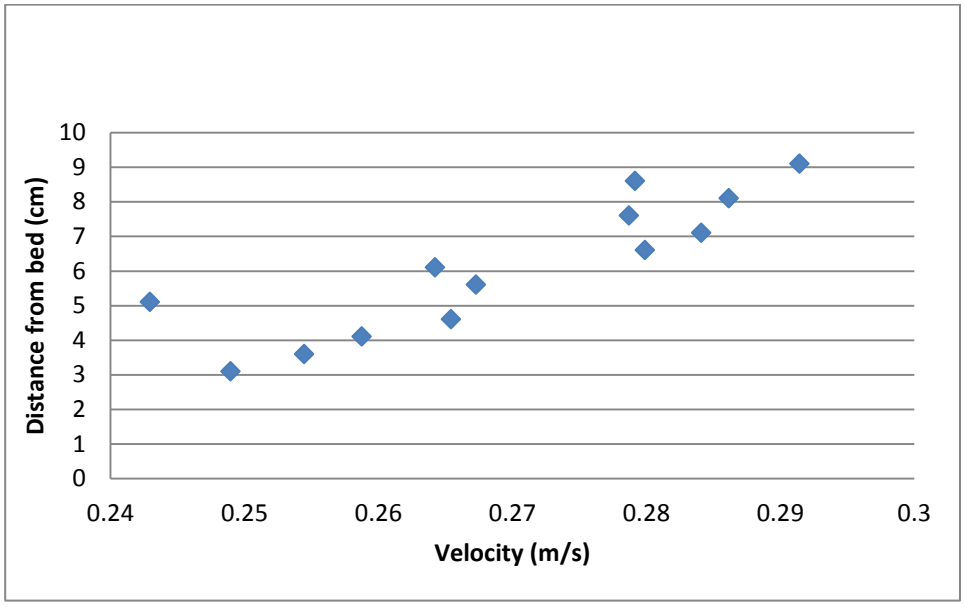

Figure 104: Velocity Profile for Small C30: X = 1.32m, Y = 0.4m

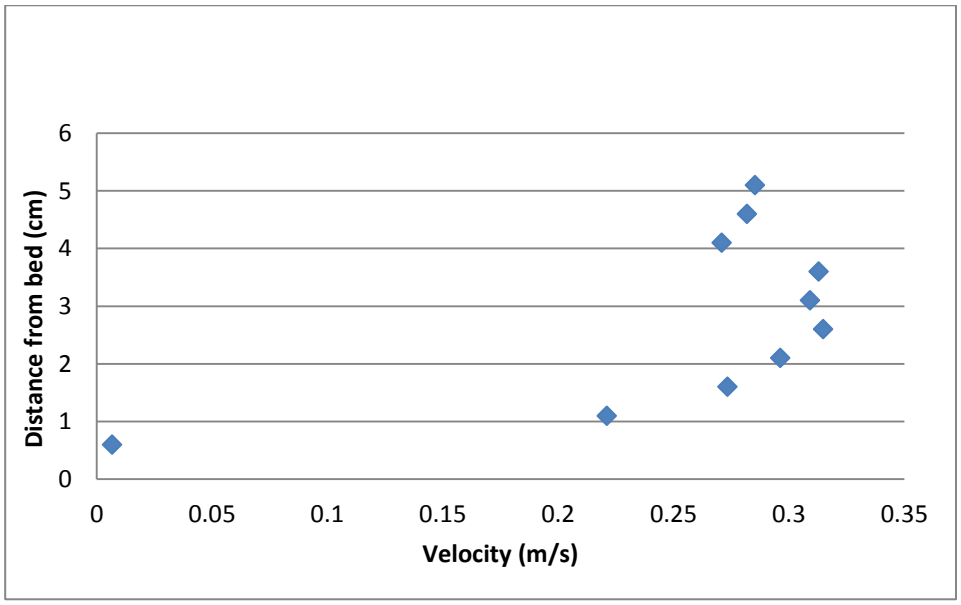

Figure 105: Velocity Profile for Small C30: X = 1.39m, Y = 0.43m

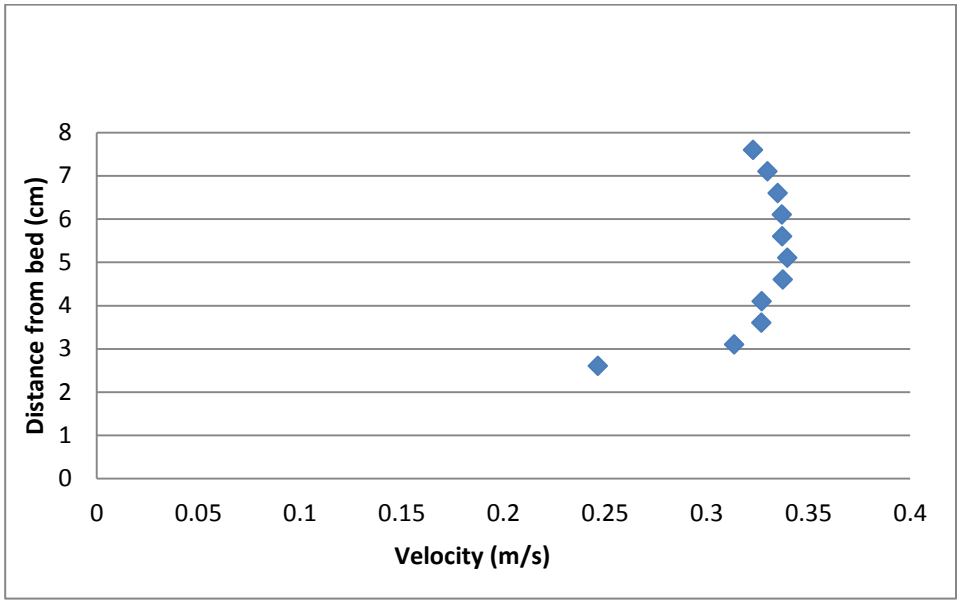

Figure 106: Velocity Profile for Small C30 X = 1.48m, Y = 0.16

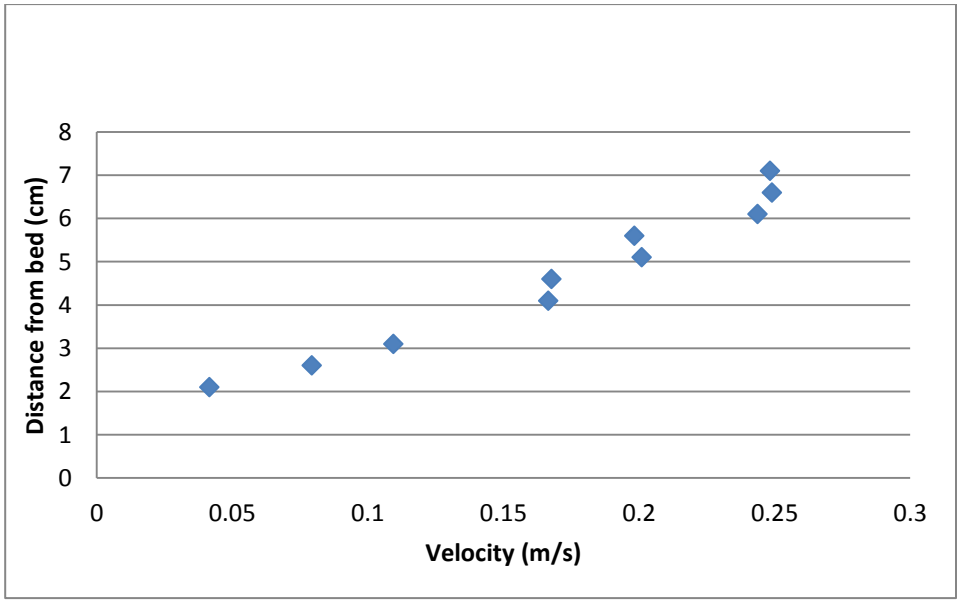

Figure 107: Velocity Profile for Small C30 X = 1.7m, Y = 0.44m

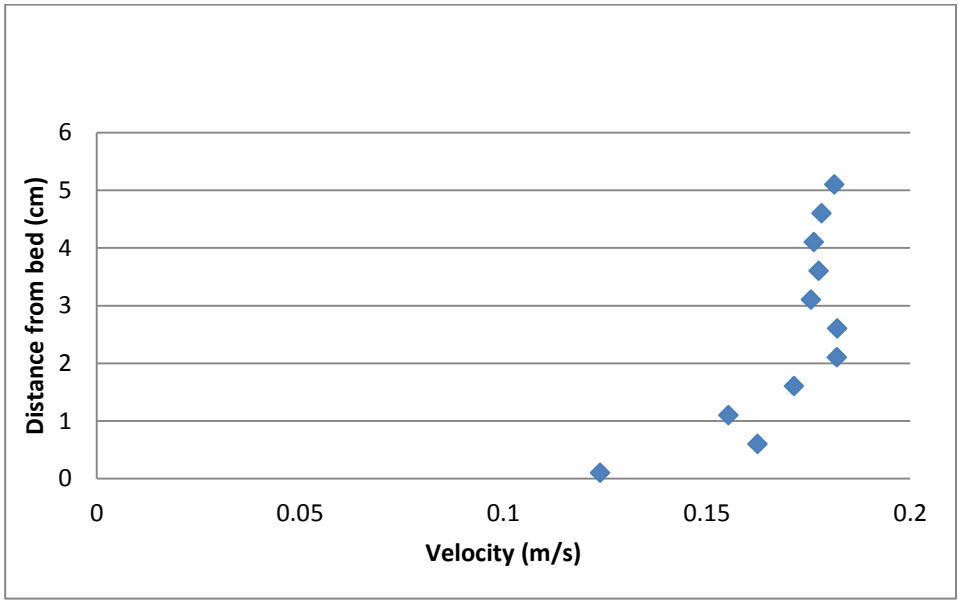

Figure 108: Velocity Profile for Small C30: X = 0.82m, Y = 0.30m

Velocity Profiles for the Large Flume with the constriction and two square piers [C32]

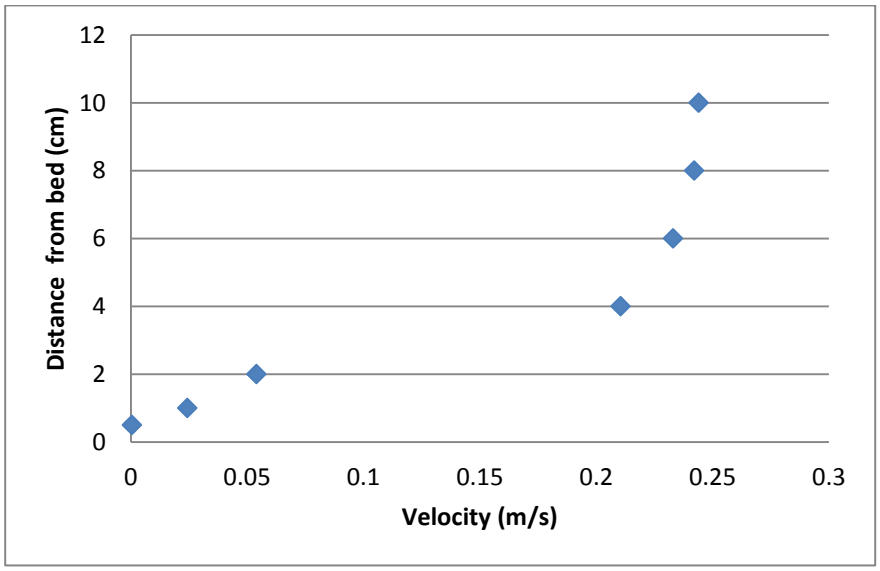

Figure 109: Velocity Profile for Large C32 X = 6.12m, Y = 0.5

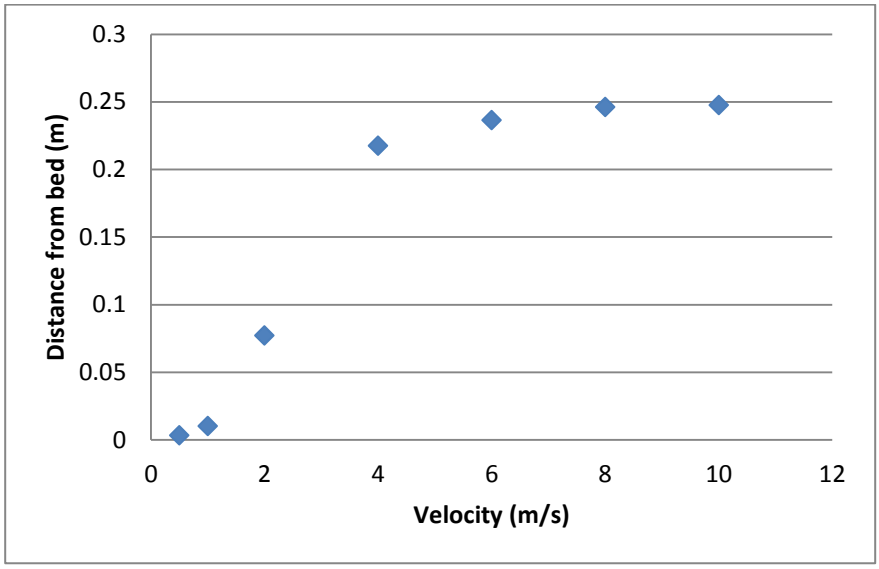

Figure 110: Velocity Profile for Large C32 X = 6.21m, Y = 0.5m

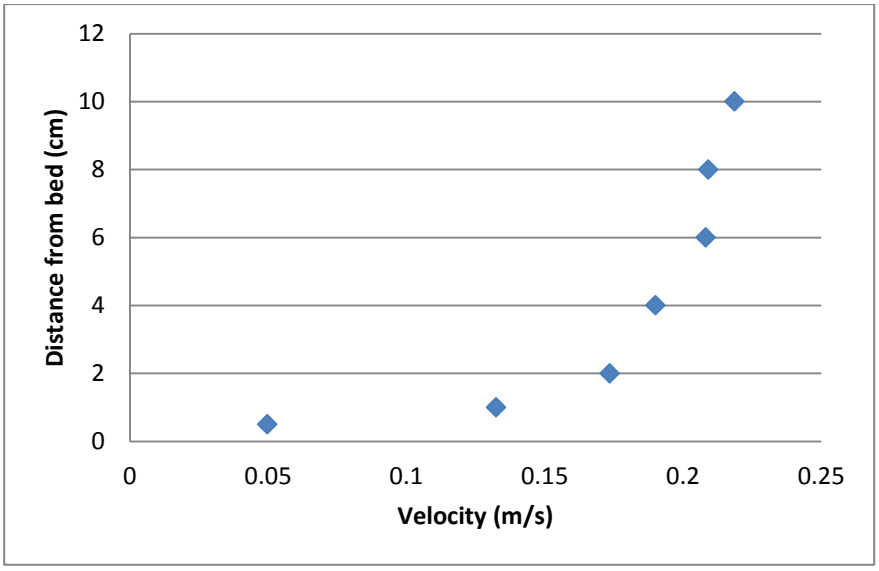

Figure 111: Velocity Profile for Large C32 X = 6.7m, Y = 0.3m

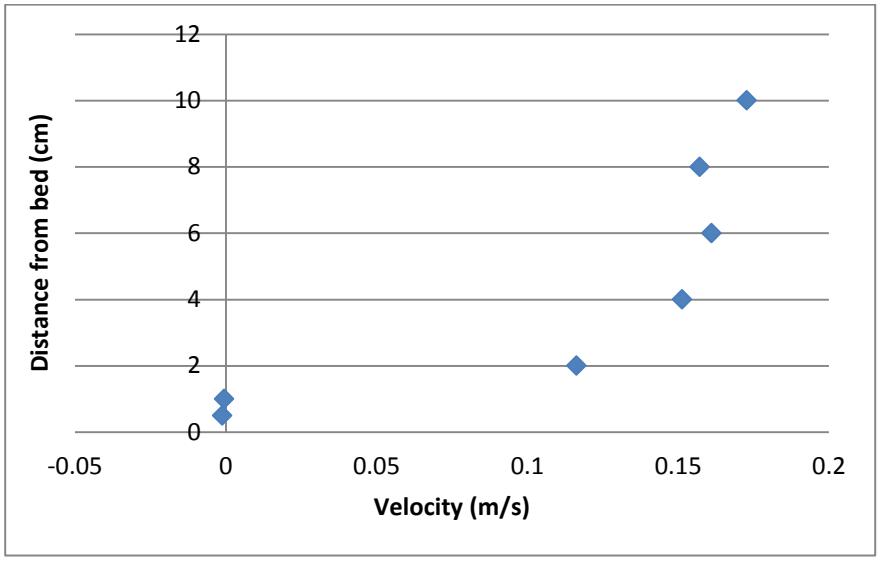

Figure 112: Velocity Profile for Large C32 X = 6.72m, Y = 0.73m

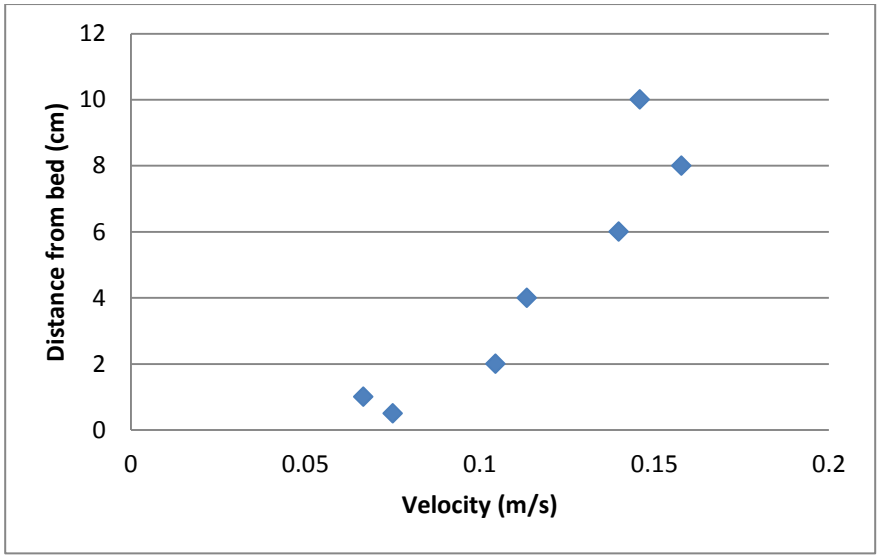

Figure 113: Velocity Profile for Large C32 X = 6.72m, Y = 0.27m

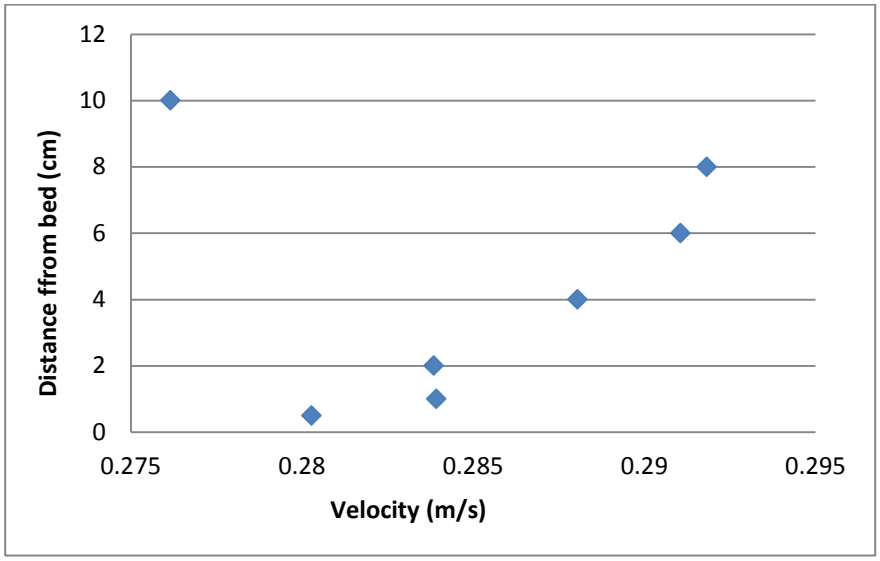

Figure 114: Velocity Profile for Large C32: X = 6.75m, Y = 0.7m

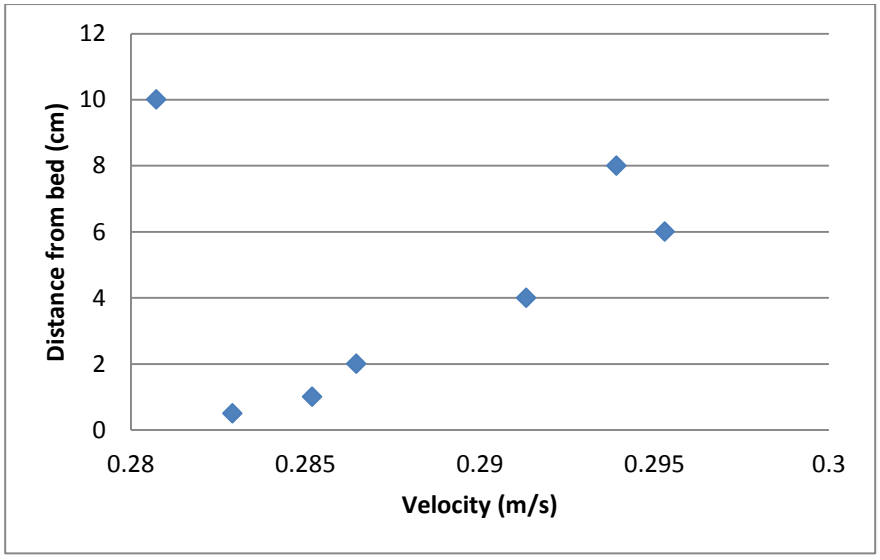

Figure 115: Velocity Profile for Large C32: X = 6.75m, Y = 0.62m

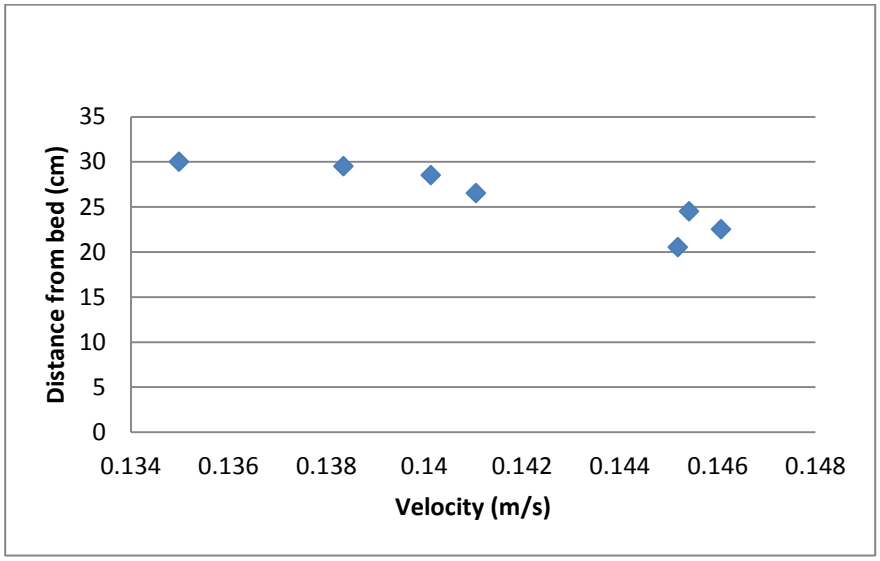

Figure 116: Velocity Profile for Large C32: X = 6.8m, Y = 0.39m

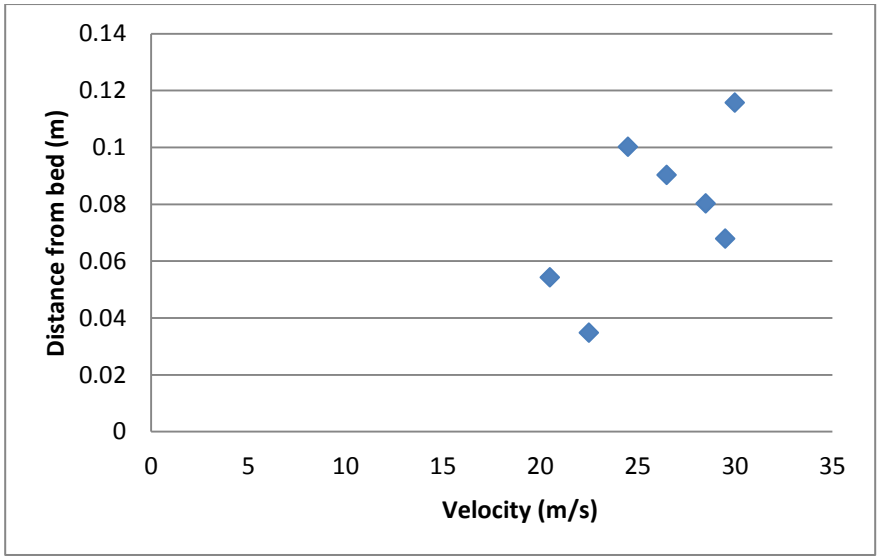

Figure 117: Velocity Profile for Large C32: X = 6.87m, Y= 0.46m

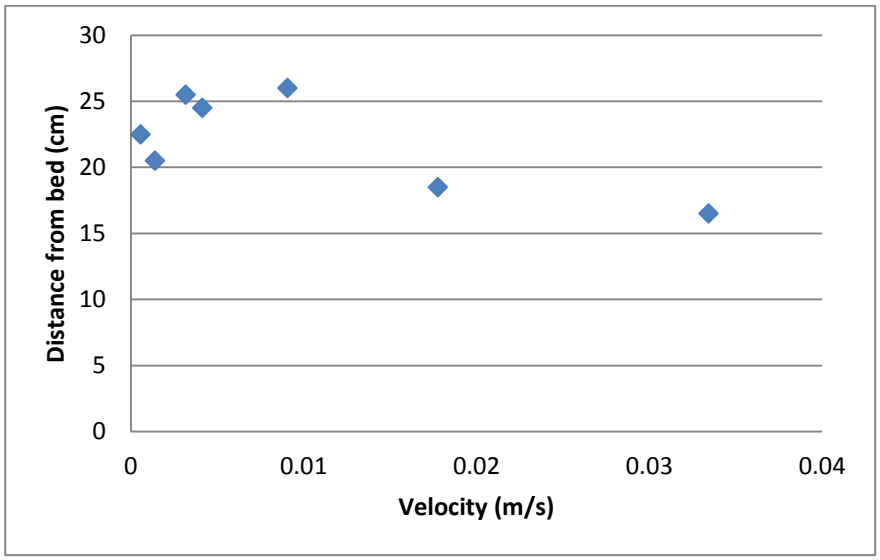

Figure 118: Velocity Profile for Large C32: X = 6.95m, Y = 0.62m

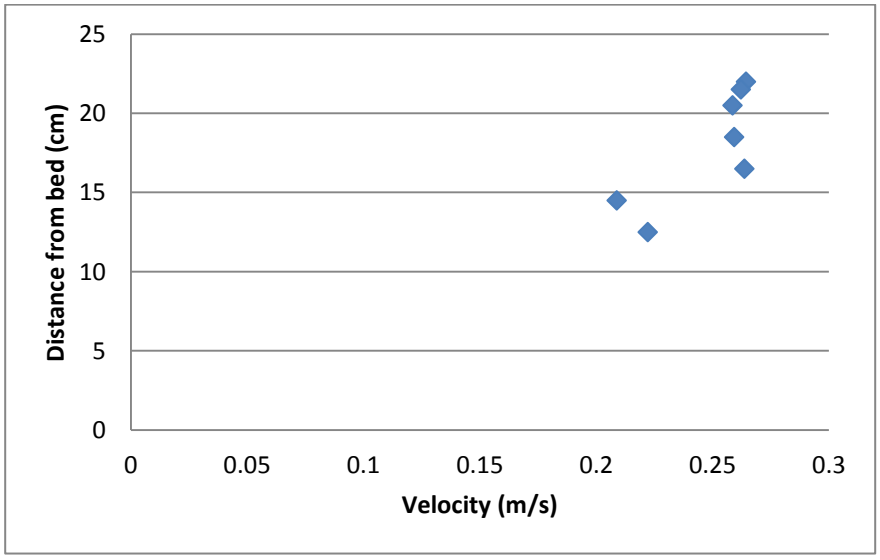

Figure 119: Velocity Profile for Large C32 X = 7.0m, Y = 0.27m

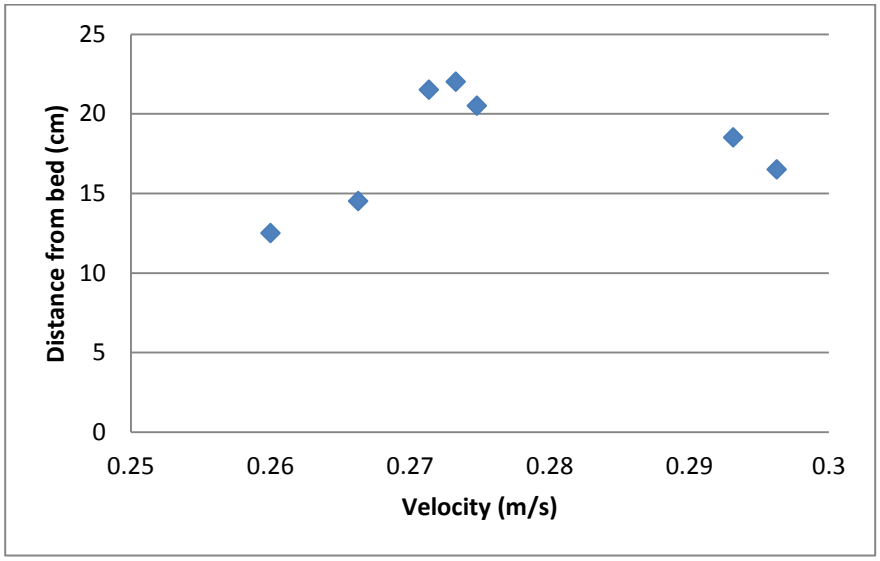

Figure 120: Velocity Profile for Large C32 X = 7.0m, Y = 0.73m

Velocity Profiles for the Small Flume with the constriction and two square piers [C32]

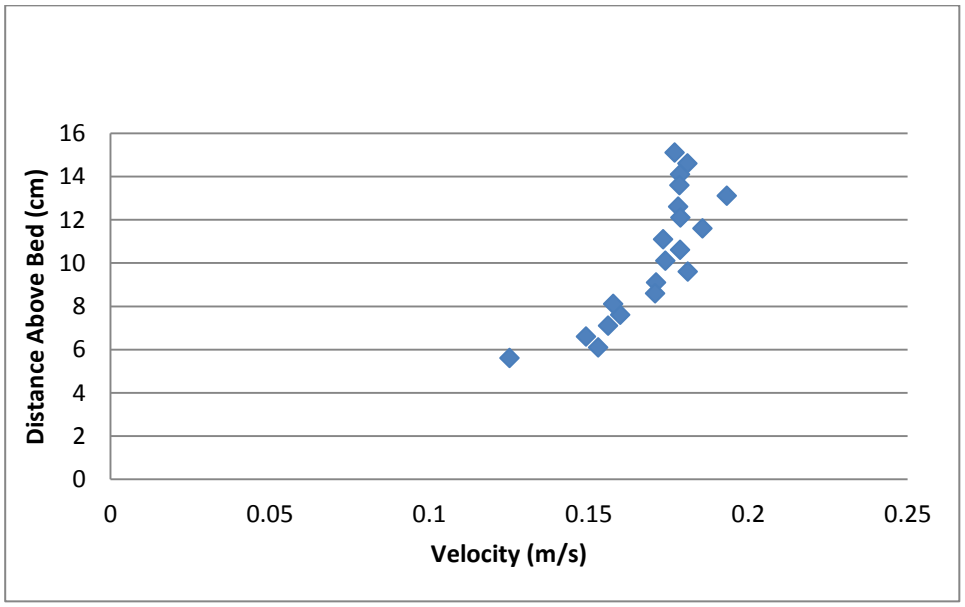

Figure 121: Velocity Profile for Small C32 X = 123cm Y = 37.8cm

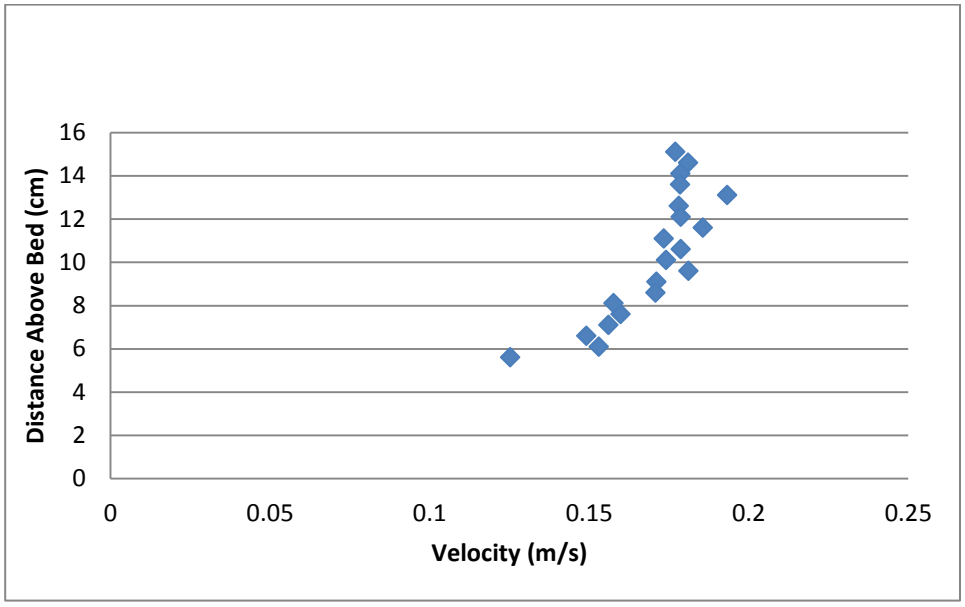

Figure 122: Velocity Profile for Small C32 X = 123cm, Y = 37.8cm

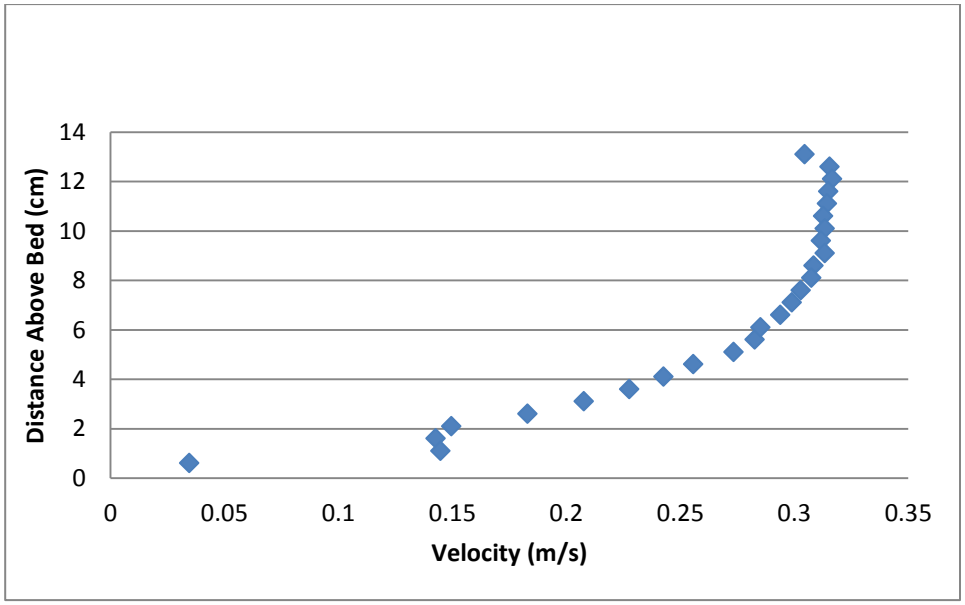

Figure 123: Velocity Profile for Small C32: X = 129cm, Y = 27.5cm

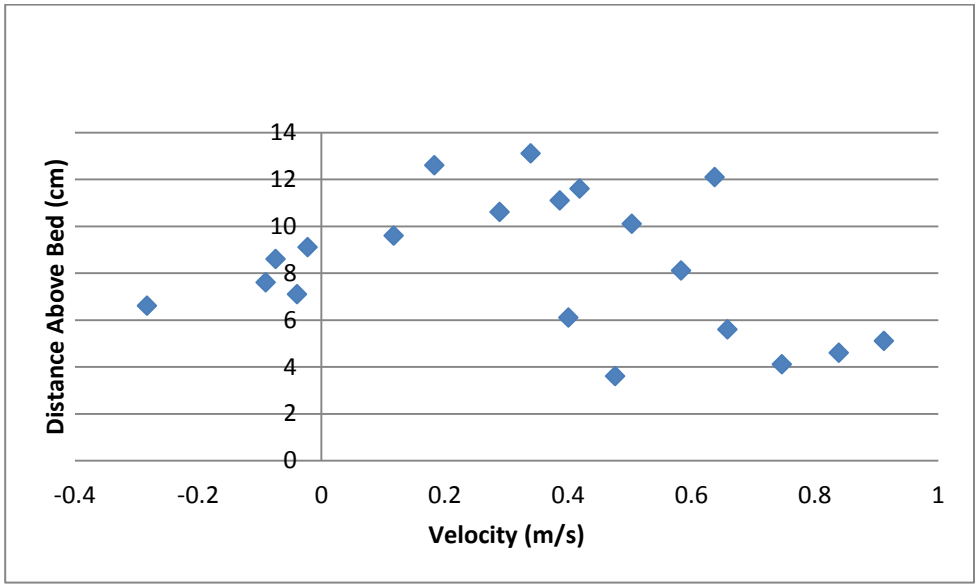

Figure 124: Velocity Profile for Small Flume C32: X = 135cm, Y = 23.2cm

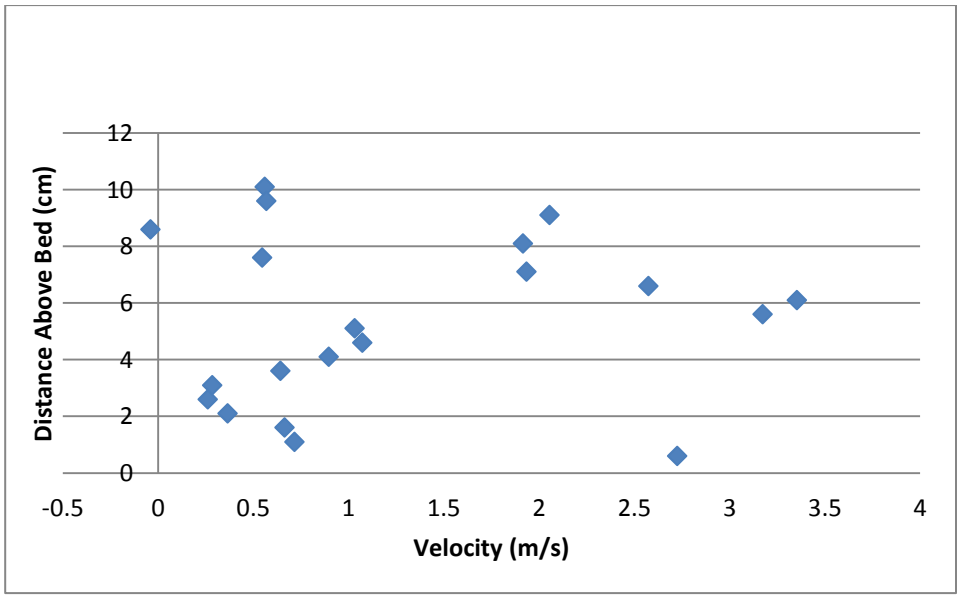

Figure 125: Velocity Profile for Small C32 X = 135cm, X = 38 cm